The electrical dynamics of dielectric barrier discharges

Please check the document version of this publication:

• A submitted manuscript is the version of the article upon submission and before peer-review. There can be important differences between the submitted version and the official published version of record. People interested in the research are advised to contact the author for the final version of the publication, or visit the DOI to the publisher's website.
• The final author version and the galley proof are versions of the publication after peer review.
• The final published version features the final layout of the paper including the volume, issue and page numbers.

Link to publication

The Electrical Dynamics of Dielectric Barrier Discharges

Floran Peeters

The Electrical Dynamics of Dielectric Barrier Discharges

PROEFSCHRIFT

ter verkrijging van de graad van doctor aan de Technische Universiteit Eindhoven, op gezag van de rector magnificus prof.dr.ir. F.P.T. Baaijens, voor een commissie aangewezen door het College voor Promoties, in het openbaar te verdedigen op donderdag 28 mei 2015 om 16:00 uur

door

Floran Johan Joseph Peeters

geboren te Rucphen

Dit proefschrift is goedgekeurd door de promotoren en de samenstelling van de promotiecommissie is als volgt:

voorzitter:	prof.dr.ir. G.M.W. Kroesen
1e promotor:	prof.dr.ir. M.C.M. van de Sanden
2e promotor:	prof.dr. N.J. Lopes Cardozo
leden:	prof.dr. Y.S. Akishev (Moscow Engineering Physics Institute)
	dr. R. Brandenburg (Leibniz Institute for Plasma Science & Technology)
	prof.dr.ir. A.C.P.M Backx
	prof.dr. F. Reniers (Université Libre de Bruxelles)
	prof.dr. U.M. Ebert

Contents

Chapter 1

Introduction

1.1. A short history of plasma processing

Artificially produced plasma finds applications in many fields of research, technology and industry, because of the ability of a plasma to provide a highly excited medium that has no chemical or physical counterpart in a natural, equilibrium environment. For example, in non-equilibrium plasma, the electron temperature can be around a 100 times higher than the gas temperature, providing enhanced chemical reactivity at a relatively low thermal load to its surroundings. Additionally, a wide range of temperature and density of plasma can be achieved through various geometries, excitation methods and process gases, providing many opportunities for materials processing and chemical conversion processes.

Plasma-based processing proliferated in the semiconductor industry, where it was first introduced in the 1960's. Initially, simple barrel-type vacuum plasma systems were developed to strip photoresists [1]. Before this, wet chemical solvents were used which were carcinogenic and costly to dispose of. This illustrates the potential of plasma technology for sustainable development; by providing chemical reactivity via electrical means instead of via potentially harmful reactive substances. Plasma processing is now commonly used in etching and deposition of materials in the production of integrated circuits and photovoltaics. These applications place specific demands on controlling the plasma via *e.g.* the amount of ion bombardment, the preferred reaction pathways between plasma and surface, or plasma and chemical precursor, and the level of impurities introduced by the process. These requirements limit the plasma to a low pressure regime, well below atmospheric pressure, necessitating the use of vacuum equipment. Vacuum equipment places constraints on scaling and throughput, as well as increasing investment and maintenance costs. Due to the high added value of these applications, however, the majority of applied research in past decades was in low pressure plasma [2].

Plasma processing at atmospheric pressure, or above, actually has a longer history than low pressure plasma processing. A German research group in 1796 reported on the conversion of hydrocarbons

3

into oil-like products when exposed to an electrical discharge [3]. After low pressure plasma sputtering was discovered by Sir William Grove in 1852, Werner von Siemens patented the first technological application of atmospheric pressure plasma in 1857. Siemens' ozonizer was the forerunner to one of the largest industrial applications of plasma: the synthesis of ozone (O_3) from molecular oxygen (O_2). Similar to the early applications of low pressure plasma in the semiconductor industry, ozone is a more sustainable, environmentally friendly replacement for *e.g.* chlorine as a sterilizing agent in water treatment. It is also used as a sterilizing agent for killing bacteria, spores and insects, in air, laundry and food, up to the complete sterilization of operating theatres between surgeries [4]. On-site and on-demand production of such a potent chemical, which quickly decays naturally and requires relatively simple, cost-effective technology is an excellent example of the advantages of atmospheric pressure plasma processing.

1.2. Plasma at atmospheric pressure

While ozone production via atmospheric pressure plasma has a long history of industrial usage, various other applications have been gaining ground over the last decades. In the following discussion no distinction is made between the various methods of atmospheric plasma generation, nor the efficacy of different process gases or other operating conditions. While the aim is to give a general overview of applications, all have been investigated or applied using Dielectric Barrier Discharges (DBDs), which are the topic of this thesis.

Air pollution control & catalysis
Similar to ozone production, the ability of atmospheric pressure plasma to induce chemical reactions can be utilized to decompose pollutants such as nitrous oxides (NO_x), sulphuric oxides (SO_2) and a wide range of other Hazardous Air Pollutants (HAP's) or Volatile Organic Compounds (VOC's) from *e.g.* factory and car exhausts [5]. The reactive yield can be significantly enhanced using a catalyst bed, *e.g.* alumina, zirconium silicate, or cobalt oxide beads, in series or at the location of the discharge, and is referred to as Plasma Enhanced

Catalysis (PEC) [3]. Atmospheric pressure plasma can also be used to dissociate CO_2, as a crucial first step in forming syngas, a mixture of H_2 and CO, which can then be further processed using the conventional Fischer-Tropsch process to produce hydrocarbons. This would allow the conversion of renewable energy, from *e.g.* photovoltaic sources, into carbon-neutral liquid fuel [6].

Plasma medicine

In plasma medicine atmospheric pressure plasma is used for therapeutic applications, including chronic wound healing, antifungal treatment, dental care and skin diseases. These beneficial properties arise from *e.g.* ultraviolet radiation and radical species, such as NO and H_2O_2, which can be produced directly by the plasma from humid air [7–9].

Light sources

CO_2 and N_2 atmospheric plasma lasers have been in use for decades [10]. Atmospheric plasma discharges, specifically in rare gases or rare gas/halogen mixtures, can also act as an intense source of ultraviolet (UV) or vacuum ultraviolet (VUV) radiation. Using phosphors, visible radiation can be generated from VUV radiation, leading to mercury-free fluorescent lamps, with clear advantages for the environment [11]. Atmospheric pressure plasma UV sources have numerous applications in the form of UV cleaning and etching of surfaces, in UV curing of printing inks and adhesives (photo polymerization) and in materials processing [12].

Surface modification and materials processing

Surface modification and materials processing by atmospheric plasma is among the most intensively studied technologies during the last decade [13]. For example, non-polluting water-based paints will adhere to polymer surfaces only after a suitable plasma pre-treatment [14]. Similarly, polymers, textiles and natural fibres can be rendered water- or oil-repellent, with obvious applications for clothing and packaging. To illustrate these effects for water, Figure 1.1 shows the results of two DBD-generated Atmospheric Pressure Plasma Jet (APPJ) treatments on barium glass, where surface energy can be increased or decreased, depending on plasma composition. Similarly,
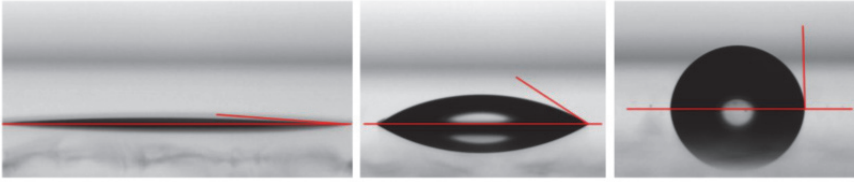
Figure 1.1: *Surface pre-treatment on barium glass (a) increased surface energy using 0.2 seconds of N_2 APPJ treatment, (b) untreated sample, (c) decreased surface energy using 0.1 seconds of N_2 + HMDS APPJ treatment [181]. The APPJ was generated via DBD.*

atmospheric pressure plasma can be used to clean metals, removing *e.g.* sulphide and chloride layers from silver surfaces [15]. Similar to surface modification, where only the top layer of the material is altered, thin films can be deposited. Thin film deposition at atmospheric pressure has been investigated for *e.g.* SiO_x, TiO_x, SnO_x, CeO_x, diamond-like carbon (DLC), carbon nanotubes and various polymers [16]. Operating at atmospheric pressure also allows for the production of hybrid coatings with relative ease, *i.e.* various liquid- or gas-phase precursors as well as nanoparticles can be injected simultaneously to obtain films with enhanced properties [17–20]. Highly uniform deposition of SiO_x films has been achieved by Fujifilm using their patented Atmospheric Pressure Glow Discharge (APGD) system [21–24]. Challenges still remain to develop deposition techniques as robust as low pressure deposition, mainly regarding deposition rates and process control, which may be resolved by an increased understanding of the mechanisms involved. There are also limitations to thin film deposition at atmospheric pressure, such as limited purity of the deposited films due to the lack of a highly controlled vacuum environment and the limited possibility of making use of ion bombardment, a hallmark of low pressure deposition, due to the shorter mean-free-path of particles at higher pressures [2,13,16,25–28].

1.3. Framework of this research

1.3.1 Dielectric Barrier Discharges

In this thesis, the focus is on atmospheric pressure plasma generated using Dielectric Barrier Discharges (DBDs). In a DBD, a high voltage on the order of several kilovolts is applied across two electrodes, where one or both electrodes are covered with an insulating material, referred to as the dielectric barrier. A schematic of a DBD is shown in Figure 1.2, along with a depiction of current and voltage characteristics over time. Upon breakdown of the gas in the gap, the dielectric prevents transition to a high current arc-like discharge, which would otherwise occur between two uncovered metal electrodes. Instead, the discharge consists of many transient microdischarges, referred to as filaments, spread across the electrode area. The filaments are self-limiting, because they charge the dielectric surface and locally negate the gap voltage until extinction occurs within 10^{-7} s. Not only are the filaments spread out over the surface, they also occur over a wide timeframe. If, for example, the DBD is driven by a sinusoidal external voltage at a frequency of 100 kHz, filaments will ignite over a period of 3 µs in each half-cycle, at many different stages of the external voltage. Though spatially uniform discharging in DBDs can be achieved under certain conditions [22–24,29–31], under most circumstances a filamentary discharge will develop [32]. Since filaments are characterized by high local electron densities of up to 10^{15} cm^{-3} and strong electric fields of up to 10^5 V/cm, it is these filaments that determine the plasma chemistry [33,34]. Our interest here is in the relation between the individual, localized filaments and the collective behavior of the discharge over the whole electrode area.

Studies of filamentary discharges tend to focus either on single filaments, experimentally [34–36], or via numerical modeling [33,34,37,38], while the link with the collective behavior of many filaments spread across the electrode area is rarely treated in literature. Single filament studies provide data on plasma chemistry, but translating this data to large area devices requires information on
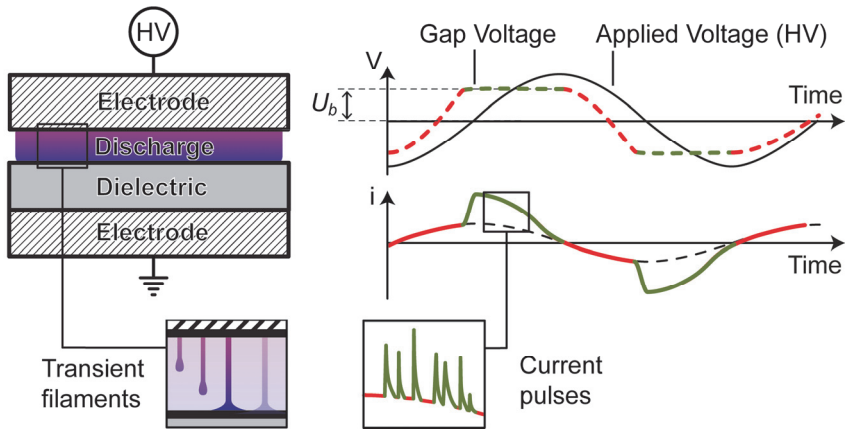
Figure 1.2: *Schematic of a DBD with one electrode covered by a dielectric. Current and voltage characteristics are given on the right-hand-side. While the plasma can be electrically modelled as having a continuous current and a constant gap voltage U_b during discharging, in reality the plasma is composed of filaments with durations of $< 10^{-7}$ seconds separated in space and time.*

the number of, and interaction between, filaments. It is, nevertheless, possible to use a simple electrical equivalent circuit for an ensemble of filaments, where the discharge can be modeled by a continuous current with a constant gap voltage, the so-called burning voltage U_b; see Figure 1.2.

1.3.2 Goals and outline of this thesis

It was already pointed out by T.C. Manley in 1943 that the plasma in a DBD can be described as having a constant burning voltage throughout a discharge half-cycle [39]. The existence of a constant burning voltage U_b throughout the discharge implies that individual filaments have, to a good approximation, the same time-averaged voltage drop during discharging. During filament propagation, most of this voltage drop will occur over the ~ 50 μm filament head where the net space charge of the plasma is concentrated, leading to electric field strengths of up to 400 kV/cm in air [27,28]. These strong transient electric fields give rise to mean electron energies > 15 eV [40] and are the driving force behind most of the reactivity in the
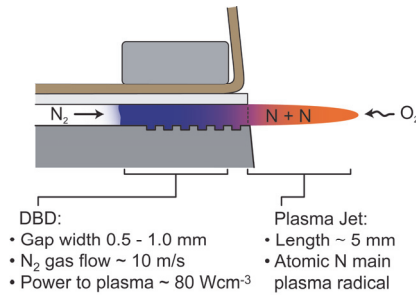
Figure 1.3: *Schematic of a single jet of the PlasmaLine®, with a description of its main characteristics [45]. Because the jet is exposed to the surrounding air, admixture of O_2 will occur.*

plasma. While the dynamics of filament propagation and the subsequent development of the filament at the dielectric surface can be satisfactorily modelled to account for experimentally observed emission intensity, spatial extent and duration of single filaments, the relation with plasma chemistry is usually not treated in detail [33,37,38,41,42]. The reasons for this are twofold, the first being the complexity of modelling even a single transient filament, which involves many different time-scales and reaction pathways [43], and the second being that too little is known about the relationship between single-filament models and real, multi-filament devices [41].

In this thesis, the link between the electrical characteristics of the discharge and the chemical reactivity is investigated experimentally. Subsequently, the relationship between the electrical characteristics of the space and time-averaged discharge and individual filaments is examined. The following research questions will be addressed:

What is the relation between the electrical characteristics of the discharge and the production of radicals?

In order to determine the relevance of U_b to the plasma chemistry, we aim to compare the electrical characteristics of the discharge to the density of plasma radicals produced. For this purpose, a commercially available Atmospheric Pressure Plasma Jet (APPJ) system is used; the VITO PlasmaLine® [44]. This system is designed for large area surface modification and deposition, consisting of two DBDs through

which N_2 process gas is passed to form two parallel linear plasma jets with a width of 20 cm and a thickness of approximately 1 mm. The PlasmaLine® was used extensively in the EU FP7 NMP project 'PlasmaNice' for grafting specific chemical groups to polymer foils [45]. A schematic of the PlasmaLine® is depicted in Figure 1.3. With this system we can study the electrical characteristics of the DBD in N_2 over a wide range of sinusoidal applied voltage amplitudes, while the plasma jet, or afterglow, can be studied to obtain radical densities produced by the DBD. For the former, we use charge-voltage (Q-V) measurements to determine burning voltage, while for the latter we use optical emission spectroscopy to determine the density of atomic N radicals in the DBD source.

In Chapter 2 we develop an electrical model for the large area DBD of the PlasmaLine®, which takes into account the possibility that the number density of filaments as a function of the applied voltage is insufficient to cover the entire electrode area. Using this model, we can determine the burning voltage U_b during the filamentary discharge, irrespective of filament number density. In Chapter 3, we determine the production efficiency of atomic N radicals in terms of the energy input from the discharge per atom produced. The results of these chapters show that both burning voltage and radical production efficiency are independent of the voltage applied to the DBD electrodes and that the only control achieved over the discharge results from the number density of filaments on the electrode area. In other words, burning voltage U_b is a characteristic of both single filaments and the discharge as a whole.

What is the connection between individual filaments and a multi-filament discharge?

Remarkably, the electrical characteristics of DBDs, such as the burning voltage U_b, can be described by a uniformly discharging capacitor, despite the plasma consisting of individual filaments that are spread across the surface and separated in time. Each filament discharges a different part of the dielectric, at different times and thus different external voltages, while the burning voltage remains effectively constant.

The constant burning voltage throughout the discharge half-cycle is commonly attributed to the surface charge deposited on the dielectric by individual filaments. These surface charges persist between discharge cycles and affect the next series of filamentary discharges when the applied voltage is reversed [41]. Self-organization of the surface charge is the preferred explanation of this phenomenon, but rigorous calculations showing that this can lead to constant burning voltages are lacking. Gibalov *et al.* model a DBD for multiple filaments with pre-existing surface charges, with good agreement to measurements, but the relationship between surface charge and current pulses and the reproducibility from cycle to cycle is not discussed [46]. Chirokov *et al.* model multi-filament interaction with a quasi-empirical Monte-Carlo simulation with good qualitative agreement with the experimentally obtained spatial distributions of the filaments, but electrical characteristics are not presented [47]. Xu and Kushner present a model to calculate the dynamics of up to 4 overlapping filaments at the surface [48]. The evolution of the charge state of the surface over many cycles is not modeled, however, and only the interaction between near-simultaneous filaments is studied. The evolution of the surface charge for a 38 mm^2 DBD in He over 24 discharge cycles is calculated by Stollenwerk *et al*, with excellent qualitative correspondence to experimental Lichtenberg images [49]. However, these results are applicable to self-organized patterns in glow-like discharges, where the 'filaments' form simultaneously in each discharge cycle, a phenomenon clearly distinct from the filamentary discharges which are the subject of this work [32].

Instead of relying on numerical models, we investigate filamentary discharges under sinusoidal excitation in greater detail using a miniature planar DBD in air. This DBD has an electrode area of approximately 7 mm^2, which is only sufficiently large to accommodate up to ~ 20 filaments per discharge cycle. This has the advantage that individual filaments can be easily distinguished in *e.g.* current measurements, which is impossible with the 80 cm^2 electrode area of the PlasmaLine$^®$. Furthermore, the miniature DBD is designed to easily replace the dielectric barrier and to alter gap width, allowing for different DBD configurations to be studied.

In Chapter 4, we combine the miniature DBD with an analog circuit designed to count and integrate individual filamentary current pulses. The aim is to investigate whether the current pulses through the filamentary discharge channels vary significantly with applied voltage amplitude or phase. At the same time, we examine how the current pulses are affected by changes in the DBD geometry and how this affects burning voltage. In Chapter 5 we combine this data with Q-V measurements and propose a model for multi-filament discharges. Our results suggest that despite the usual assumption of immobile surface charges in computational models of DBDs [46–50], a significant proportion of the surface charge can redistribute across the surface. This, in turn, has consequences for the interpretation of equivalent circuit models of DBDs. Finally, an Outlook is presented in which additional experiments are proposed to further verify the model for multi-filament discharges.

Chapter 2

The Influence of Partial Surface Discharging on the Electrical Characterization of DBDs

The determination of internal electrical discharge parameters, such as plasma current and burning voltage, in a DBD relies on an equivalent circuit based on series capacitances for discharge gap and dielectric material. An effective dielectric capacitance for the discharge can be obtained from Q-V diagrams, also called Lissajous figures, during discharging, which may not be a constant for a given DBD geometry. It has been shown experimentally that microdischarges, which can consist of narrow channels in either diffuse or filamentary form, may not fully cover the available discharge area. Here, we report on measurements of the effective dielectric capacitance as a function of applied voltage amplitude in a DBD plasma jet system operating in N_2 and derive equations to determine the conductively transferred charge, burning voltage and the proportion of the electrode surface over which discharging occurs.

2.1. Introduction

Dielectric barrier discharges (DBDs) are used on a large industrial scale and have been studied for more than a century [51,52]. More recently, interest has expanded to include plasma jets based on DBDs [53–57]. Irrespective of the design of a DBD system, Q-V diagrams can be used to deduce the physical properties of the discharges, namely the conductively transferred charge during the discharge, ΔQ_{dis}, per half-cycle and the voltage across the gas gap during the discharge, U_b, referred to as the burning voltage. The product of ΔQ_{dis} and U_b equals the energy dissipated in the discharge per half-cycle. The burning voltage U_b is essentially the DC voltage across microdischarges in a DBD and is therefore directly related to the reduced electric field, which in turn determines the electron energy distribution function (EEDF) [58,59]. The transferred charge is *e.g.* a measure of the number of filaments formed per half-cycle, which, together with U_b, determines the chemical reactivity, excitation, dissociation and ionization rates within the discharge volume [60–62]. These two properties are therefore sufficient to compare DBDs between different reactor geometries for a given gas composition and pressure.

To interpret Q-V data, the simplest equivalent circuit of a DBD system which is commonly used assumes a dielectric capacitance (C_{diel}) and gap capacitance (C_{gap}) in series, with the discharge represented by a parallel component to the gap capacitance [39,63–71], see Figure 1(a). The equations used by different authors using this approach are discussed by Pipa *et al*, mainly regarding the use of a pre-factor when calculating current in the discharge gap from the current measured in the external circuit [72]. Pipa *et al.* have also reported on the evaluation of the dielectric and total system capacitance for pulsed driven DBDs and their effect on the determination of discharge properties from Q-V data [73,74]. Thorough derivations of equations, relating measured current and measured voltage to the current and voltage within the discharge gap
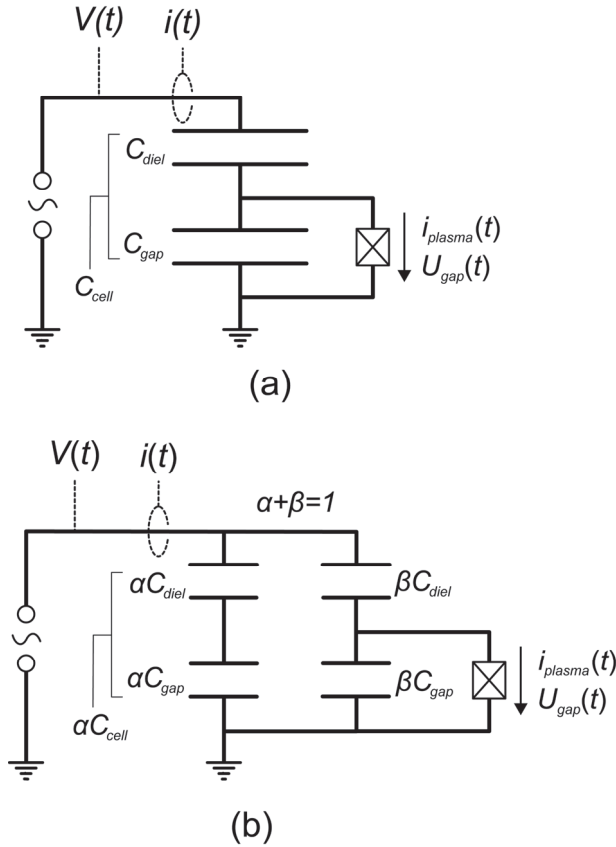
Figure 2.1: *(a) Standard simplest equivalent circuit commonly used to obtain electrical properties of DBDs. The discharge is represented as a component parallel to the gap and is considered an electronic 'black box'. The capacitances C_{diel} and C_{gap} in series are equivalent to the cell capacitance C_{cell}. (b) Alternative simplest equivalent circuit as presented in this chapter. The dielectric capacitance C_{diel} and gap capacitance C_{gap} are split into two sections, the non-discharging areal fraction α and the discharging areal fraction β, where only the β fraction has a parallel component representing the discharge. The capacitances αC_{diel} and αC_{gap} in series are equivalent to αC_{cell} and are strictly referred to as αC_{cell} in the main text.*

for arbitrary applied voltage waveforms are given by Liu and Neiger [64].

With sinusoidal driving voltage, the *Q-V* diagrams will approximate a parallelogram, as schematically depicted in Figure 2.2. This has the
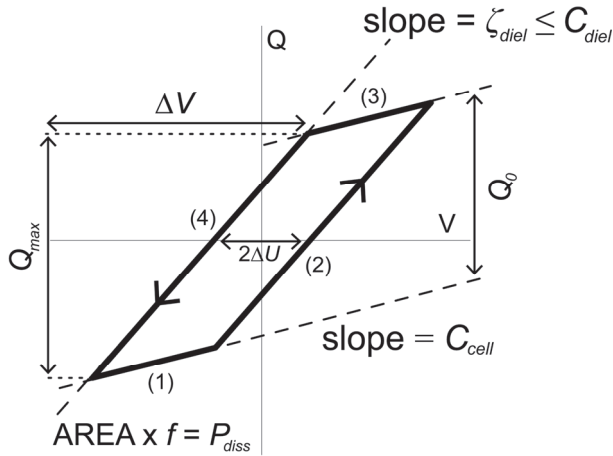
Figure 2.2: *Schematic of an idealized DBD Q-V plot with the quantities that can be extracted from it. The topic of this work is the physical interpretation of the quantities ΔU, Q_{max} and Q_0 for conditions where the slopes of (2) and (4), referred to as effective dielectric capacitance ζ_{diel}, are lower than the actual dielectric capacitance of the discharge cell, C_{diel}.*

advantage that relevant parameters can be extracted easily from the dimensions of the parallelogram, without the need for extensive calculations. This approach was pioneered by Manley in 1943, who first identified the slopes of the (2) and (4) segments in Figure 2.2 as the dielectric capacitance C_{diel} and the value of *ΔU* as the burning voltage U_b [39]. Here, we find that the slopes of (2) and (4), related to the charge transfer during the discharge, depend strongly on the external applied voltage amplitude. They can therefore not be identified as the dielectric capacitance C_{diel} in the equivalent circuit for the DBD, since this capacitance is determined by the fixed geometry of the DBD system. The same behavior is observed by Reichen *et al.* at low applied voltages, with the (2) and (4) slopes saturating to the dielectric capacitance C_{diel} only at applied voltages several kilovolts above the breakdown voltage [71]. This effect is attributed to the limited extent of microdischarges over the dielectric surface and a semi-empirical model for the development of the *Q-V* slopes with increasing applied voltage is presented. However, the effect of these variable *Q-V* slopes on the electrical properties within the discharge gap is not discussed [71]. To distinguish between the geometrically determined dielectric capacitance C_{diel} and the slopes of

17

(2) and (4) in Q-V parallelograms, we will refer to the latter as the effective dielectric capacitance, ζ_{diel}, as indicated in Figure 2.2.

Using an alternative equivalent circuit, depicted in Figure 2.1(b), where the electrode area is split into a non-discharging and a discharging areal fraction, α and β, we conclude that the slope of the parallelogram during a discharge, ζ_{diel}, is in fact a linear combination of the total capacitance of the system C_{cell} and the dielectric capacitance C_{diel}. This leads to different relations between the physically relevant discharge parameters and the dimensions of the parallelogram, for which several new equations are derived. These new equations should be applied to analysis of Q-V plots for cases when only a part of the dielectric surface is discharged during a half-cycle. The effect of partial surface discharging in DBDs is analogous to having stray capacitance in the circuit [70]. While the equations derived here are specific to partial surface discharging, stray capacitance can also be represented by a non-discharging capacitance comparable to αC_{cell} in the alternative equivalent circuit of Figure 2.1(b). Though the emphasis is on classical parallelogram figures, similar considerations may be applicable to Q-V diagrams obtained from *e.g.* pulsed-driven DBDs.

2.2. Experimental setup

2.2.1 DBD system

A commercially available DBD plasma jet system is investigated in this work, the VITO PlasmaLine® [44]. The source utilizes a double slit atmospheric pressure dielectric barrier discharge with a 2 mm thick quartz and mica stack on the powered electrode. The grounded, stainless steel electrode has a ribbed design, making the discharge gap vary between 0.5 and 1 mm. The total width of the system is 20 cm, while the electrodes extend 2 cm into the source. The HV electrodes are hollow and water cooled, with a 2 slm flow at 20 °C. A typical flow of 200 slm nitrogen gas is passed through the DBDs, resulting in
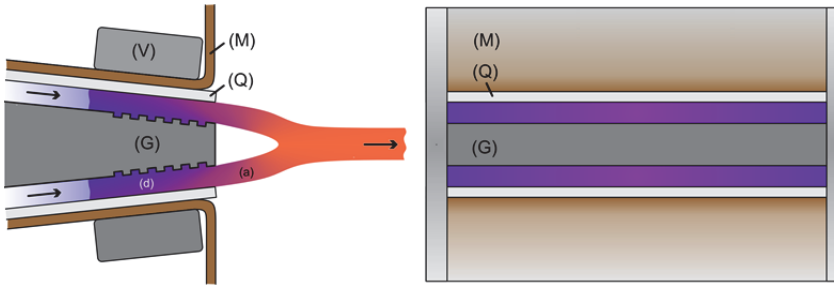
Figure 2.3: *Schematic cross section (left) and front view (right) of the PlasmaLine® source. Indicated are high voltage electrodes (V), mica dielectric barriers (M), quartz dielectric barriers (Q), grounded central electrode (G), discharge region (d), afterglow region (a).*

two parallel 20 cm wide linear plasma jets, with an average gas flow velocity of around 11 m/s. In this way uniform surface treatment can be achieved despite the filamentary nature of the discharge. A nearly sinusoidal voltage with a frequency of 55 kHz and amplitude of up to 11.6 kV is applied to the electrodes using an AFS generator (G10S-V) and transformer (GT40). The discharge itself is sealed off from the atmosphere by virtue of the large gas flow, while the plasma jets emerging from the DBDs are exposed to the surrounding air. A schematic of the plasma source is shown in Figure 2.3. The setup is placed inside a ventilation cabinet with an exhaust flow of 5 m^3min^{-1}.

The voltage applied to the system is measured using a Tektronix P6015A High Voltage Probe and the current is monitored using a Pearson Model 4100 Current Monitor. Both are attached to the high voltage line between transformer and HV electrodes, as schematically depicted in Figure 2.1. Measuring current on the HV line removes the possibility of leak currents to ground not being registered, but requires careful sealing of the gap between current measurement coil and HV line with paraffin to prevent unwanted (but significant) discharges. Note that this method is employed only for the PlasmaLine® and that for other DBDs in this thesis, the more conventional method of placing a large measurement capacitor in series with DBD and ground is used. Both current and voltage data were stored using an Agilent InfiniiVision 5000 digital oscilloscope. Calibration measurements were performed to ensure that both voltage probe and current monitor have the same time delay within the sampling rate of the scope (~ 0.4 ns).

The temperature of the central electrode was monitored using a Luxtron I652 Fiber Optic Thermometer, while the temperature of the cooling water was registered digitally through thermocouples in the cooling system.

2.3. Theory

2.3.1 Relations obtained for the alternative equivalent circuit

To provide a correct physical interpretation of Q-V plots with ζ_{diel} a function of applied voltage amplitude, we begin with the equations for plasma current $i_{plasma}(t)$, plasma charge $Q_{plasma}(t)$ and gap voltage $U_{gap}(t)$ derived using the alternative equivalent circuit depicted in Figure 2.1(b). Note that $Q_{plasma}(t)$ is the charge on the capacitor βC_{gap} which can be transferred conductively during a discharge and $i_{plasma}(t)$ is its time derivative. It should also be stressed that $U_{gap}(t)$ is the gap voltage only of the discharging part of the circuit. The derivations of these equations are given in the appendix and are expressed in terms of $V(t)$ and $Q(t)$:

$$i_{plasma}(t) = \frac{1}{1 - C_{cell}/C_{diel}} \left[\frac{dQ(t)}{dt} - C_{cell} \frac{dV(t)}{dt} \right] \qquad (2.1)$$

$$Q(t) = \left(1 - \frac{C_{cell}}{C_{diel}} \right) Q_{plasma}(t) + C_{cell} V(t) \qquad (2.2)$$

$$U_{gap}(t) = \left(1 + \frac{\alpha}{\beta} \frac{C_{cell}}{C_{diel}} \right) V(t) - \frac{1}{\beta C_{diel}} Q(t). \qquad (2.3)$$

These equations are valid for sinusoidal applied voltage where α, β, C_{cell} and C_{diel} remain constant throughout a full period. Equations (2.1) and (2.2) are independent of α and β, from which it can be concluded that the plasma current $i_{plasma}(t)$ obtained using the alternative simplest equivalent circuit is identical to the plasma current from the standard simplest equivalent circuit, depicted in Figures 2.1(b) and 2.1(a), respectively. For $\beta = 1$ and $\alpha = 0$, Equation (2.3) reduces to:

$$U_{gap}(t) = V(t) - \frac{1}{C_{diel}} Q(t),$$ (2.4)

which is the equation for gap voltage for the standard equivalent circuit [72]. For $\beta = 0$ and $\alpha = 1$, Equation (2.3) is indeterminate, because in this case the alternative equivalent circuit of Figure 2.1(b) is invalid, since the plasma 'black box' over which $U_{gap}(t)$ is determined drops out and only the two left-most capacitors remain.

To understand the difference between a Q-V diagram obtained from fully discharging electrodes, *i.e.* $\beta = 1$, and a Q-V diagram obtained from partially discharging electrodes where $\beta < 1$, we turn to Equation (2.2) and expand its terms to include α and β:

$$
\begin{aligned}
Q(t) &= \left(1 - \frac{\beta C_{cell}}{\beta C_{diel}}\right) Q_{plasma}(t) + (\alpha + \beta) C_{cell} V(t) \\
&= \left[\left(1 - \frac{\beta C_{cell}}{\beta C_{diel}}\right) Q_{plasma}(t) + \beta C_{cell} V(t)\right]_{discharging} \\
&+ \left[\alpha C_{cell} V(t)\right]_{non\text{-}discharging},
\end{aligned}
$$ (2.5)

where we use the fact that $Q_{plasma}(t)$ occurs only in the discharging part of the equivalent circuit, which we make explicit by including β in its prefactor. Equation (2.5) now shows that the effect of a non-discharging fractional area, in the form of αC_{diel} and αC_{gap} in series in the equivalent circuit, is nothing more than an addition of $\alpha C_{cell} V(t)$ to the Q-V plot. This is illustrated schematically in Figure 2.4, where an as-measured Q-V plot has this additional term subtracted to obtain the Q-V plot of the discharging part of the alternative equivalent circuit. Note that both the intersections of the corrected Q-V plot at $Q(t) = 0$, related to gap voltage, and the maximum values of $Q(t)$, related to transferred charge, are changed.

Since the discharging part of the alternative equivalent circuit, represented by βC_{diel}, βC_{gap} and the plasma component, is essentially identical to the standard equivalent circuit, the slopes in the corrected
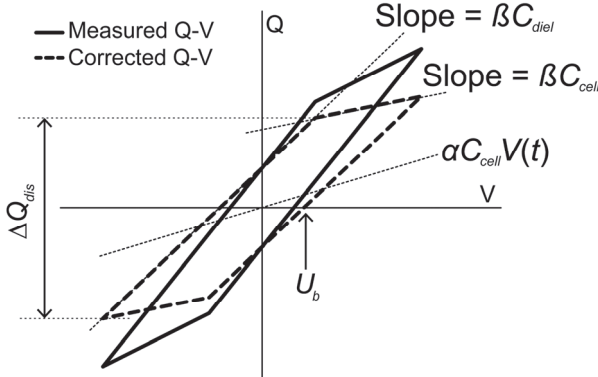
Figure 2.4: *Schematic of an as-measured Q-V diagram and a corrected Q-V diagram after subtraction of the slope αC_{cell}. In this example $\alpha \approx 0.7$ and only 30% of the available electrode area discharges twice per period. The corrected Q-V diagram would be obtained if only the discharging areal fraction of the DBD could be measured.*

Q-V diagram can be identified as βC_{diel} (during discharging) and βC_{cell} (between discharging). If the slope during discharging in an as-measured Q-V plot is ζ_{diel} we then have:

$$\zeta_{diel} = \alpha C_{cell} + \beta C_{diel} \,, \tag{2.6}$$

which, combined with $\alpha + \beta = 1$, gives:

$$\alpha = \frac{C_{diel} - \zeta_{diel}}{C_{diel} - C_{cell}}, \tag{2.7}$$

$$\beta = \frac{\zeta_{diel} - C_{cell}}{C_{diel} - C_{cell}}. \tag{2.8}$$

Using Equations (2.7) and (2.8), we can now relate the characteristics Q_{max} and ΔU, as obtained from as-measured Q-V plots, indicated in Figure 2.2, to the physical properties of the discharge, ΔQ_{dis} and U_b.

The conductively transferred charge ΔQ_{dis} is the change in charge during a discharge, $Q(t_{plasma\ off}) - Q(t_{plasma\ on})$ in the *corrected* Q-V plot, similar to Q_{max} in the as-measured Q-V data. In standard theory, where $\beta = 1$, Q_{max} always equals ΔQ_{dis}, but for partial discharging

Q_{max} will exceed ΔQ_{dis} due to the additional term $\alpha C_{cell}V(t)$. From geometric considerations we can state that

$$\Delta Q_{dis} = Q_{\max} - \alpha C_{cell}\Delta V , \qquad (2.9)$$

where ΔV is the change in external voltage during a discharge, as indicated in Figure 2.2. From the same figure it also becomes clear that

$$Q_{\max} = \zeta_{diel}\Delta V , \qquad (2.10)$$

which can be substituted into (2.9) along with (2.7) to obtain, after rearranging

$$\Delta Q_{dis} = \frac{1 - C_{cell}/\zeta_{diel}}{1 - C_{cell}/C_{diel}} Q_{\max} . \qquad (2.11)$$

This equation provides a direct relation between the observed transferred charge in the as-measured Q-V plot and the actual conductively transferred charge during a discharge period.

The burning voltage U_b can be easily obtained from Equation (2.3) for $U_{gap}(t)$ in the alternative equivalent circuit. Since $V(t)$ and $Q(t)$ are always in phase, evidenced by the straight lines in the Q-V parallelograms, $U_{gap}(t)$ is constant and equal to U_b during a discharge. By noting that in the as-measured Q-V plot, $Q(t) = 0$ when $V(t) = \pm \Delta U$, we find for U_b:

$$U_b = \pm\left(1 + \frac{\alpha}{\beta}\frac{C_{cell}}{C_{diel}}\right)\Delta U , \qquad (2.12)$$

Which after substitution of Equations (2.7) and (2.8) yields:

$$U_b = \frac{1 - C_{cell}/C_{diel}}{1 - C_{cell}/\zeta_{diel}}\Delta U . \qquad (2.13)$$

Here, we again find a simple relation between a parameter derived directly from a Lissajous figure and its true physical value when $\zeta_{diel} \leq C_{diel}$.

Since the enclosed surface area of a Q-V plot is equal to the work W done by the plasma and the enclosed area is conserved after subtraction of the additional term $Q(t) = \alpha C_{cell} V(t)$, we find that

$$W = 2\Delta U Q_{max} = 2U_b \Delta Q_{dis} , \tag{2.14}$$

where the latter equality follows from Equations (2.11) and (2.13). The dissipated power P_{diss} is also easily calculated by multiplying W by the discharge frequency f.

There is one useful parameter which needs to be discussed and which is often used in the literature [63,64,72,75], the difference in charge between the (1) and (3) segments in Figure 2.2, Q_0. It can be related to Q_{max} via a geometric relation [73]:

$$Q_0 = \left(1 - C_{cell} / \zeta_{diel} \right) Q_{max} , \tag{2.15}$$

which, combined with Equation (2.11), leads to the relation

$$\Delta Q_{dis} = \frac{Q_0}{1 - C_{cell} / C_{diel}} . \tag{2.16}$$

This equation can be used to obtain ΔQ_{dis} through the parameter Q_0, which can be more accurately obtained from the Q-V plots than Q_{max}, provided the true dielectric capacitance C_{diel}, determined by DBD geometry, is known. Since $\zeta_{diel} \leq C_{diel}$ we can also state the following:

$$Q_0 < \Delta Q_{dis} \leq Q_{max} . \tag{2.17}$$

Only when $\zeta_{diel} = C_{diel}$, conductively transferred charge ΔQ_{dis} is equal to Q_{max} and the voltage U_b is equal to ΔU observed in the Lissajous figures, otherwise the former is overestimated and the latter underestimated. Equations (2.11), (2.13) and (2.16) described above

allow the calculation of the physical parameters ΔQ_{dis} and U_b from the parameters derived from as-measured Q-V diagrams Q_{max}, Q_0 and ΔU, if only a fraction of the total electrode surface area participates in discharging during a half-period of the applied voltage.

2.4. Results & discussion

2.4.1 Capacitances from the *Q-V* parallelograms

Current and voltage data were acquired for applied voltage amplitudes of 4.2, 8.4, 10.1, 11.1 and 11.6 kV. For each measurement cycle data was obtained only after the system has reached a steady-state, which was checked by monitoring the temperature of both the central electrode and the cooling water. Current and voltage data were digitally averaged for 512 full periods and stored using the oscilloscope. The instantaneous charge $Q(t)$ in the discharge cell is determined from the measured current $i(t)$ using:

$$Q(t) = q + \int_0^t i(t')dt'. \tag{2.18}$$

The integration constant q is determined by imposing the constraint that the average charge over time equals zero. By plotting $Q(t)$ against the measured applied voltage $V(t)$, Lissajous figures are obtained. For applied voltage amplitudes of 4.2, 8.4, 10.1, 11.1 and 11.6 kV these are depicted in Figure 2.5(a). Using this data we will derive the capacitances C_{cell}, ζ_{diel} and, along with a separate measurement of C_{diel} obtained with the system at room temperature, the gap capacitance C_{gap}. It is implicitly assumed that all capacitances depend only on the applied voltage amplitude, but are otherwise constant as a function of time, *i.e.* we treat the Q-V data as ideal parallelograms. Note that both discharge gaps of the PlasmaLine® are treated as a single DBD.
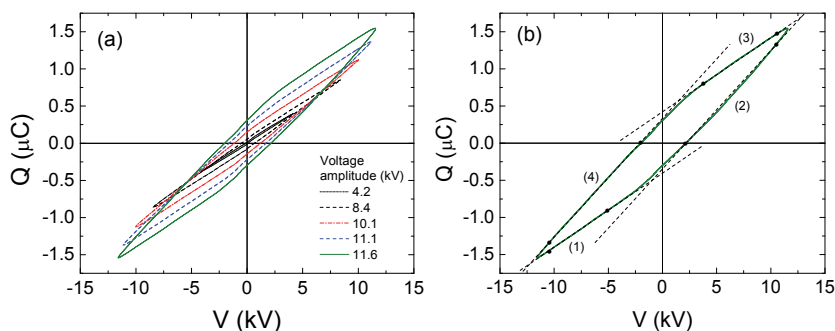
Figure 2.5: *(a) Q-V plots measured with increasing applied voltage amplitude and (b) the 11.6 kV data with fitted slopes. Only (1) and (4) are used to determine slopes, with fitting ranges indicated by black dots, while (2) and (3) have the slopes of (4) and (1), respectively. Each Q-V plot is an average of 512 full periods.*

Cell capacitance C_{cell} is equivalent to the slopes of (1) and (3) in the Lissajous figures, when there is no discharge in the cell. This capacitance corresponds to the combined series capacitance of the dielectric C_{diel} and the discharge gap C_{gap} in Figure 2.1 and depends mainly on the geometry of the system and the dielectrics used. The interpretation of C_{cell} from *Q-V* parallelograms presented here is no different from that of standard theory; in the absence of discharging the parallel components of αC_{diel} and αC_{gap} in series and βC_{diel} and βC_{gap} in series still equal C_{cell}. Linear fits of the slopes of (1) are used to obtain C_{cell} values, as indicated in Figure 2.5(b) and plotted in Figure 2.6(a). Cell capacitance C_{cell} increases by approximately 6% from lowest to highest applied voltage amplitude. An additional cell capacitance with minimal to no discharging was measured 10 minutes after operating the system at the highest applied voltage, showing that the increased cell capacitance is maintained in the absence of plasma. Only after several hours does the system return to the lowest observed value of 92 ± 2 pF. Furthermore, starting with an 'unconditioned' system at an increased gas flow of 300 slm, C_{cell} was found to increase by only 3% from lowest to highest applied voltage. At a gas flow of 200 slm, the steady-state temperature of the central electrode does increase from 20 °C (lowest applied voltage amplitude, no noticeable heating) to 70 °C (highest applied voltage amplitude), though the increase in C_{cell} is maintained longer than the temperature of the system. No conclusions regarding the origin of this effect can
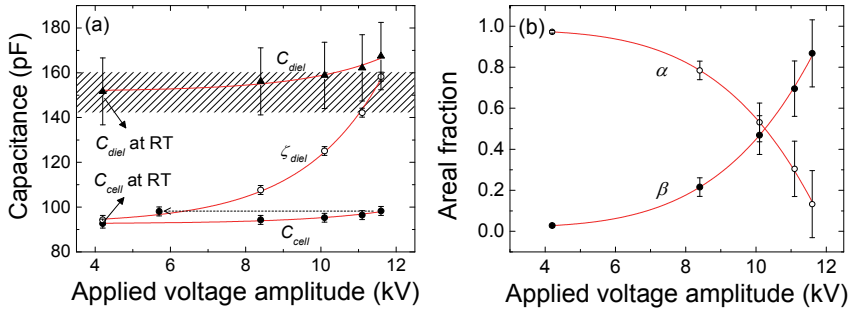
Figure 2.6: *(a) The cell, effective dielectric, and dielectric capacitances as a function of applied voltage amplitude extracted from the Q-V diagrams in Figure 2.5. The hatched area indicates the value of C_{diel} in the kHz range determined from separate measurements at room temperature (RT). The dashed arrow points to the cell capacitance at low applied voltage measured 10 minutes after operating the system in thermal equilibrium at the highest applied voltage. (b) The areal fractions α and β calculated from this data.*

be drawn based on the available data and we will proceed with the 'unconditioned' steady-state data as measured from lowest to highest applied voltage, *i.e.* with C_{cell} increasing.

Linear fits of the slopes of (4) are used to obtain ζ_{diel} values, as indicated in Figure 2.5(b) and plotted in Figure 2.6(a). Because only the HV electrode is covered by dielectric material, the discharge is not completely symmetric. The slope of (2) increases during the discharge and has a slight bulge compared to slope (4), as seen in Figure 2.5(b). Differences between half-cycles in asymmetric DBD configurations have been observed previously by Osawa *et al.* and Stollenwerk *et al*; the former observing alternating Townsend and filamentary discharges by using alumina and soda-glass on opposing electrodes, the latter observing offsets in the charge accumulation between half-cycles on a BSO crystal acting as the barrier on one electrode and ITO on the other [76–78]. Similar effects may be at play here and only the more constant slope of (4) is used to determine the effective dielectric capacitance. The differences between the two half-cycles will not be treated in detail in this work, since our interest lies with determining only the general properties of the discharge, such as the average conductively transferred charge during a discharge cycle, with the *Q-V* data presented here serving only to illustrate the effect

of increasing effective dielectric capacitance ζ_{diel}. Also depicted in Figure 2.6(a) is a separate measurement of the dielectric capacitance C_{diel} at room temperature, in the absence of plasma. This capacitance was measured by short-circuiting C_{gap} by carefully inserting a 0.5 mm thick aluminum sheet into a discharge gap up to a depth of 2 cm, so that it corresponds to the area of the high voltage electrode depicted in Figure 2.3 as (V). Since the capacitance was measured for only one discharge gap, it was multiplied by two to obtain the total dielectric capacitance of the system.

The effective dielectric capacitance ζ_{diel} increases sharply as a function of voltage amplitude, having a value close to the cell capacitance C_{cell} for low applied voltage and increasing to the value expected for the total dielectric capacitance C_{diel} for the highest applied voltage. It should be noted that the increase of ζ_{diel} as a function of applied voltage is clearly different from that observed by Reichen *et al* , who observe ζ_{diel} saturating to a constant value at sufficiently high applied voltages [71]. This can be attributed to the ribbed design of the PlasmaLine® central electrode, involving two different gap widths and a large number of edges. At the lowest voltage amplitude, only minimal discharging occurs in the gap, likely at the edges along the central electrode, leading to a small difference between (1)/(3) and (2)/(4) slopes. As the voltage amplitude is increased, more plasma is ignited across the discharge gap, conductively transferring charge from dielectric to grounded electrode and vice-versa and leading to increased (2)/(4) slopes.

We assume C_{gap} is a constant for all applied voltage amplitudes and independent of ζ_{diel}, temperature, or degree of ionization in the gap. The value of C_{gap} is therefore calculated using the measured values of C_{cell} and C_{diel} at room temperature, giving $C_{gap} = 238 \pm 20$ pF. The 6% increase observed for C_{cell} with increasing applied voltage is then assumed to be due entirely to an increase in C_{diel}. With C_{gap} known, C_{diel} can be easily calculated from C_{cell} using:

$$C_{diel} = \frac{C_{cell}C_{gap}}{C_{gap} - C_{cell}}, \qquad (2.19)$$

the results of which are included in Figure 2.6(a). Using Equations
(2.7) and (2.8), the values of the areal fractions α and β are calculated
for each applied voltage amplitude from the data in Figure 2.6(a) and
plotted in Figure 2.6(b). The parameter β can be identified as the
fraction of the dielectric surface area conductively discharged during
a half-cycle, whereas α is the fraction of the surface area behaving
capacitively. For the lowest applied voltage in this work we find β is
between (3 ± 5)%, while for the highest applied voltage it is (86 ±
14)%.

The areas enclosed by the Q-V plots point to dissipated powers P_{diss}
ranging from 9 W to 500 W for the lowest and highest applied voltage
amplitude, respectively. The areas enclosed by the linear fits, such as
depicted in Figure 2.5(b), are up to 8% greater, mainly due to the
sharper edges at the extremes of the applied voltage. This discrepancy
can be considered a measure of the deviation of the data from ideal
parallelograms, and it should be emphasized that we treat the data as
the latter throughout this work.

2.4.2 Physical properties derived using alternative circuit

Using the offsets of the linear fits of the (1) and (3) segments of the
Q-V diagrams, such as depicted in Figure 2.5(b), the values of Q_0 are
obtained. These are then converted to Q_{max} and ΔQ_{dis} using Equations
(2.15) and (2.16), respectively. This method is more accurate than
directly determining Q_{max} from the Q-V diagrams and converting to
ΔQ_{dis} using Equation (2.11). Results are depicted in Figure 2.7(a). The
data clearly shows that ΔQ_{dis} differs significantly from Q_{max} and the
two become similar only for large applied voltage amplitudes. The
applied voltage amplitude at which $\Delta Q_{dis} = Q_{max}$, i.e. β =1, falls
outside the range of measured data. Note that $\Delta Q_{dis} \approx 0$ at low applied
voltage, when $\zeta_{diel} \approx C_{cell}$, which shows there is little discharging
occurring in the gap. This does not hold for Q_{max}, which has a value >
0, further emphasizing that transferred charge obtained directly from a
Q-V diagram is not a direct measure of conductively transferred
charge. At the lowest applied voltage the difference between ζ_{diel} and
C_{diel} is at its largest and it follows from Equation (2.11) that Q_{max} is
approximately 20 times greater than ΔQ_{dis}. In other words, when the
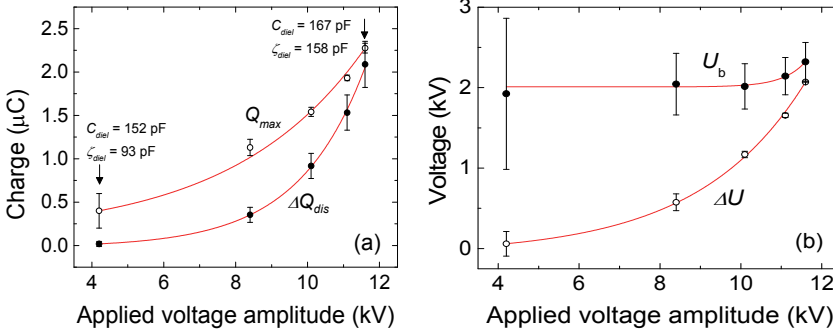
Figure 2.7: (*a*) *The total transferred charge Q_{max}, in as-measured Q-V plots and the charge transferred conductively ΔQ_{dis}, calculated using Equation (2.15) and (16), and (b) ΔU from the Q-V plots and the actual burning voltage U_b, calculated using Equation (13). The lines are guides to the eye.*

applied voltage is increased and minor discharging begins to occur somewhere in the gap, only a very small proportion of Q_{max} observed in a *Q-V* diagram is truly due to conductively transferred charge. This is one of the important results of this chapter, namely *that Q_{max} is greater than the conductively transferred charge if the effective dielectric capacitance ζ_{diel} is lower than the total dielectric capacitance C_{diel} of the system.*

In Figure 2.7(b), the burning voltage U_b is calculated using Equation (2.13) and is compared to ΔU. The latter is obtained from the *Q-V* plots from the intersections of the linear fits of the (2) and (4) segments at $Q = 0$. The burning voltage U_b is the constant voltage across the gap where microdischarges are present. In other words, it is the gap voltage in those places where the gas gap, or the surface of the dielectric, is conductive. As seen in Figure 2.7(b), it is always greater than the voltage ΔU seen in the *Q-V* plots and the two become similar only at high applied voltage amplitudes. *A very important result of our analysis is that the burning voltage is revealed to be nearly constant as a function of applied voltage amplitude, which suggests that individual microdischarges do not change with increasing voltage.* Since ΔQ_{dis} does increase significantly with applied voltage amplitude, it can be argued that only the number of microdischarges increases and, hence, the electrode area they cover.
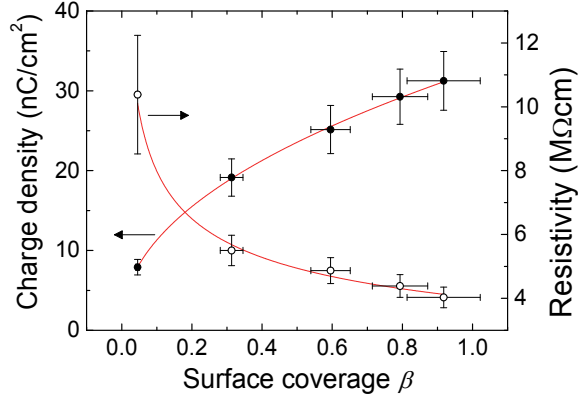
Figure 2.8: *The net charge density $\sigma_{tranfer}$ across the gap during a discharge and the plasma resistivity ρ_{plasma} averaged over the discharge area, both corrected for the variable surface coverage of the discharge, β. The vertical error bars do not include the uncertainty in total area or gap width.*

Many derived properties will depend on the discharged areal fraction β, among them the net charge density transferred across the gap during discharging

$$\sigma_{transfer} = \frac{\Delta Q_{dis}}{\beta A}, \tag{2.20}$$

and the resistivity of the plasma averaged over the discharge area

$$\rho_{plasma}(t) = \frac{U_b}{i_{plasma}(t)} \frac{\beta A}{l}, \tag{2.21}$$

where A is the total electrode area and l the gap width, which for the PlasmaLine$^®$ are estimated at 80 cm^2 and ~ 0.075 cm, respectively. Note that the resistivity will depend weakly on time via $i_{plasma}(t)$. We will determine ρ_{plasma} at the time when $Q(t) = 0$, which makes it a good measure of the minimum resistivity. Results of both equations are plotted in Figure 2.8. It can be concluded that ΔQ_{dis} increases faster than β with increasing applied voltage amplitude and that, as a result, the net charge transfer per unit area of plasma increases as well. Similarly, the resistivity of the plasma continues to drop with

31

increasing β. Provided that individual microdischarges remain nearly equivalent with increasing applied voltage amplitude, the data in Figure 2.8 indicates that not only the absolute number, but also the density or ignition frequency of microdischarges over the area corresponding to β is increasing. The relation between individual microdischarges and their areal density to the electrical properties of the entire discharge deserves further study. The main point here is that bulk electrical properties such as burning voltage U_b, plasma resistivity ρ_{plasma}, transferred charge ΔQ_{dis} and its density $\sigma_{transfer}$, along with their dependence on applied voltage amplitude, could not have been determined correctly from measured data if we would have used the assumption that $\zeta_{diel} = C_{diel}$.

2.5. Conclusions

When only a fraction of the available discharge area is conductively discharged during a half-cycle, the slope ζ_{diel} observed in Q-V plots will depend on applied voltage and will be lower than C_{diel}. It is possible to determine whether this is the case for a given discharge, by checking if ζ_{diel} saturates to a constant value with increasing applied voltage [71]. In this work, saturation did not occur at the highest applied voltage and hence separate capacitance measurements are used, even though this introduces larger errors. The system used in this work has an uncommon design with a ribbed central electrode and relatively low dielectric capacitance through the use of thick dielectrics, introduced to protect against large heat loads. Also, the grounded electrode has a larger area than the HV electrode, which may lead to larger discharge areas with increasing applied voltage. Combined with the wide range of input power between 9 and 500 W, a large variation in ζ_{diel} with applied voltage amplitude becomes apparent.

We present an alternative equivalent circuit for analysis of Q-V parallelograms when only a fraction of the electrode area is discharged. The steeper slopes in the Q-V plots then become a linear combination of the total capacitance of the system C_{cell} and the dielectric capacitance C_{diel}. This leads to different relations between

the true physical values for burning voltage U_b and conductively transferred charge ΔQ_{dis} and the dimensions of the parallelogram, for which new equations are derived. Furthermore, the proportion of the electrode surface over which discharging occurs can be easily calculated from the observed slope in the parallelograms ζ_{diel} and the true total dielectric capacitance C_{diel}. Care must be taken when identifying the steeper slopes in Q-V diagrams with the total dielectric capacitance, or non-physical values for conductively transferred charge and breakdown voltage will be found.

Appendix to Chapter 2

A2.1 Plasma current for the alternative equivalent circuit

From Kirchoff's laws we find the following relations for the equivalent circuit in Figure 2.2(b):

$$q_{cell}(t) = \alpha C_{cell} V(t), \tag{A2.1}$$

$$q_{diel}(t) = \beta C_{diel} U_{diel}(t), \tag{A2.2}$$

$$q_{gap}(t) = \beta C_{gap} U_{gap}(t), \tag{A2.3}$$

$$\frac{dq_{diel}(t)}{dt} = \frac{dQ(t)}{dt} - \frac{dq_{cell}(t)}{dt}, \tag{A2.4}$$

$$i_{plasma}(t) = \frac{dq_{diel}(t)}{dt} - \frac{dq_{gap}(t)}{dt}, \tag{A2.5}$$

$$U_{gap}(t) = V(t) - U_{diel}(t), \tag{A2.6}$$

where $q_{cell}(t)$ is the charge in the non-discharging fractional area α of the DBD and $q_{diel}(t)$ and $q_{gap}(t)$ the charge on the discharging fractional area β of the dielectric and gap capacitance, respectively, with $U_{diel}(t)$ and $U_{gap}(t)$ their associated voltages. Note that $U_{diel}(t)$ and $U_{gap}(t)$ are specifically defined here as the voltage drops over the discharging fraction β of the circuit and that the dielectric and gap voltage drops over the non-discharging fraction α are not included separately in the derivation. Substituting (A2.2) into (A2.6) we have for the gas gap voltage:

$$U_{gap}(t) = V(t) - \frac{q_{diel}(t)}{\beta C_{diel}} \tag{A2.7}$$

And substituting (A2.7) into (A2.3)

$$q_{gap}(t) = \beta C_{gap} \left(V(t) - \frac{q_{diel}(t)}{\beta C_{diel}} \right), \tag{A2.8}$$

Followed by substitution of (A2.8) into (A2.5) and rearranging, we have for the plasma current:

$$i_{plasma}(t) = \left(1 + \frac{C_{gap}}{C_{diel}}\right)\frac{dq_{diel}(t)}{dt} - \beta C_{gap}\frac{dV(t)}{dt} \qquad (A2.9)$$

Further substituting (A2.1) into (A2.4) and the result into (A2.9), we obtain:

$$i_{plasma}(t) = \left(1 + \frac{C_{gap}}{C_{diel}}\right)\left(\frac{dQ(t)}{dt} - \alpha C_{cell}\frac{dV(t)}{dt}\right) - \beta C_{gap}\frac{dV(t)}{dt}, \qquad (A2.10)$$

which can be further simplified using the identities $C_{cell}^{-1} = C_{diel}^{-1} + C_{gap}^{-1}$ and $\alpha + \beta = 1$ to obtain:

$$i_{plasma}(t) = \left(\frac{1}{1 - C_{cell}/C_{diel}}\right)\left(\frac{dQ(t)}{dt} - C_{cell}\frac{dV(t)}{dt}\right), \qquad (A2.11)$$

which is the same as Equation (2.1), showing that the plasma current for the alternative equivalent circuit in Figure 2.1(b) is independent of α and β and equal to that found for the standard equivalent circuit depicted in Figure 2.1(a) [72].

Integrating (A2.11) over time we have:

$$Q_{plasma}(t) = \left(\frac{1}{1 - C_{cell}/C_{diel}}\right)(Q(t) - C_{cell}V(t) + q_0), \qquad (A2.12)$$

where q_0 is an integration constant. Since $Q_{plasma}(t)$, $V(t)$ and $Q(t)$ must all average out to zero over time, the integration constant q_0 can be set to zero and solving for $Q(t)$ we have:

$$Q(t) = \left(1 - \frac{C_{cell}}{C_{diel}}\right)Q_{plasma}(t) + C_{cell}V(t), \qquad (A2.13)$$

which is equivalent to Equation (2.2).

A2.2 Gap voltage for the alternative equivalent circuit

We begin by integration of (A2.4) over time and substituting into (A2.7):

$$
\begin{aligned}
U_{gap}(t) &= V(t) - \frac{1}{\beta C_{diel}} \int \left(\frac{dQ(t)}{dt} - \frac{dq_{cell}(t)}{dt} \right) dt \\
&= V(t) - \frac{1}{\beta C_{diel}} \left(Q(t) - q_{cell}(t) + q_1 \right) \qquad \text{(A2.14)} \\
&= V(t) - \frac{1}{\beta C_{diel}} \left(Q(t) - q_{cell}(t) \right) + U_1,
\end{aligned}
$$

where q_1 and U_1 are integration constants. By further substituting (A2.1) and collecting terms we have:

$$
U_{gap}(t) = \left(1 + \frac{\alpha}{\beta} \frac{C_{cell}}{C_{diel}} \right) V(t) - \frac{1}{\beta C_{diel}} Q(t) + U_1. \qquad \text{(A2.15)}
$$

By further noting that for symmetric discharges, leading to symmetric Q-V plots, $U_{gap}(t)$, $V(t)$ and $Q(t)$ must all average out to zero over time, the integration constant U_1 can be set to zero:

$$
U_{gap}(t) = \left(1 + \frac{\alpha}{\beta} \frac{C_{cell}}{C_{diel}} \right) V(t) - \frac{1}{\beta C_{diel}} Q(t), \qquad \text{(A2.16)}
$$

which is equivalent to Equation (2.3).

Chapter 3

Radical Production in a DBD with Variable Surface Coverage

In a nitrogen-fed plasma jet, atomic nitrogen is the longest lived radical species and, through recombination, gives rise to highly reactive excited nitrogen species. In this chapter, the atomic nitrogen concentration is determined using direct 2D imaging of the visible First Positive System emission from the jet. From the same emission, the molecular oxygen and water concentration admixed in the jet from the surrounding air is estimated. For the pure nitrogen jet used here, the specific energy input per nitrogen atom is found to be 320 ± 20 eV/atom, comparable to the specific energy for other atomic nitrogen sources in the literature. It is shown that the production efficiency of atomic nitrogen does not depend on the amplitude of the applied voltage of the DBD and any increase in radical production is due to an increase of the electrode area covered by the discharge, i.e. an increase in the number of microdischarges.

3.1. Introduction

The potential of Atmospheric Pressure Plasma Jets (APPJ) for industrial application, such as deposition of thin films, surface modification or surface pre-treatment, is determined by the type and concentration of active species in the jet. In the case of the PlasmaLine® system, a high nitrogen flow between 5 - 15 m/s passes through a DBD to activate the gas. See Figure 3.1 for a schematic overview of the system and Figure 3.2 for a photograph of the PlasmaLine® jets. Nitrogen is highly suitable as a carrier gas for large scale processing, since it is much cheaper than noble gases such as argon or helium, has a high propensity for forming metastable excited states via energy-pooling reactions and can be dissociated into nitrogen atoms, providing a highly reactive afterglow. Atomic nitrogen is expected to be the plasma radical with the longest lifetime and the highest concentration in the post-discharge and hence the main reactive particle in the plasma jet [54,79–81]. Our interest lies with determining the production efficiency of atomic nitrogen as a function of the applied voltage amplitude in the DBD source and evaluate its relationship with the surface coverage β of the discharge, introduced in Chapter 2.

In this chapter, the atomic nitrogen concentration at the source exit is quantified by measuring the optical emission in the jet of the N_2 First Positive System (FPS), $N_2(B\ ^3\Pi_g \rightarrow A\ ^3\Sigma_u^+)$, which has an intensity proportional to the rate of recombination of N atoms because direct electron excitation of N_2 is absent. The rate of decay of the FPS emission can then be used to determine N atom concentrations, provided the gas flow velocity in the jet is known [82]. Quantifying atomic N in this way is not new; in previous work by other authors, the flowing afterglow, or jet, from a small-scale atmospheric pressure source is directed into a quartz tube, which allows for a large spatial extent of the jet by adjusting flow velocity, while simultaneously preventing admixture of the surrounding air [54,83]. Using these tubes, the decay of the FPS emission can be reliably measured using Optical Emission Spectroscopy (OES) at various distances from the
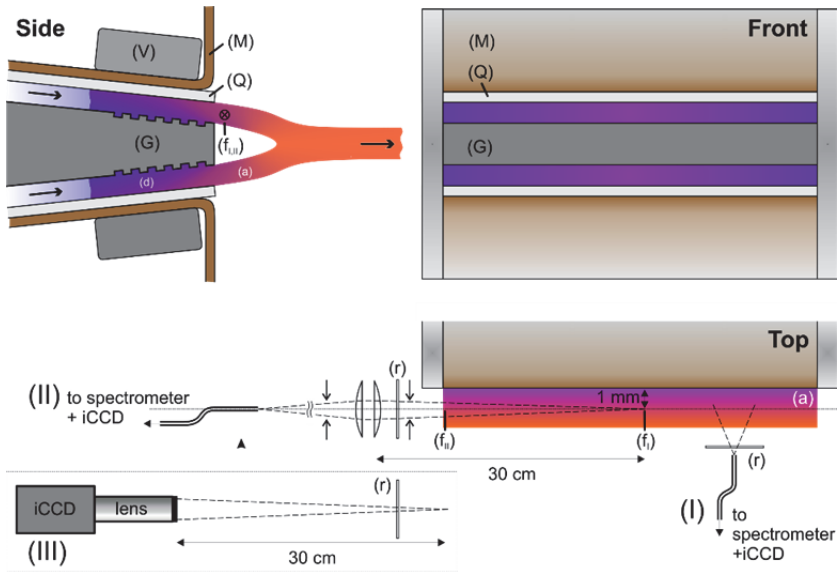
Figure 3.1: *Schematic (cross-sectional) side, front and top view of the PlasmaLine source. Indicated are high voltage electrodes (V), mica dielectric barriers (M), quartz dielectric barriers (Q), grounded central electrode (G), discharge region (d), afterglow/jet region (a), optical filters (r) and focal points of optical setups (II) and (III) ($f_{I,II}$). Optical setup (I) is used to obtain the spectrum of the discharge, (II) to obtain the spectrum of the jet and (III) to image the FPS emission as a function of position.*

plasma source. For the commercial PlasmaLine[®] system, however, adding a flow tube to the 20 cm wide plasma jets is impractical and direct 2D CCD imaging of the spatial decay of the FPS emission in the jet is used instead. In the absence of a flow tube, both gas flow velocity and the admixture of molecular oxygen and water from the surrounding air have to be assessed to obtain accurate measures of the atomic N concentration in the source.

This chapter is structured as follows: first, the optical emission from the jet is compared to the emission from the discharge over a wide wavelength range using low resolution (0.3 nm) spectroscopy. From this analysis it is concluded that the FPS emission in the jet depends solely on the recombination of N atoms and can be used to quantify its concentration. This emission is then measured as a function of position using an iCCD camera, with flow velocity measurements
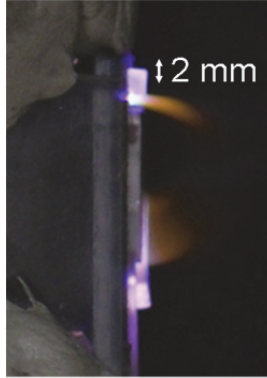
Figure 3.2: *Photograph of the PlasmaLine® jets viewed from the side, with an indication of scale.*

using a hot-wire anemometer providing the relationship between position and time-of-flight of species in the jet [84]. Combining this data, the atomic N concentration at the source exit is determined as a function of applied voltage amplitude. Also, an estimate of the admixture of molecular oxygen and water is made using a 1D convection-reaction model, so that their influence on the atomic N measurements can be assessed. Finally, the atomic N production is compared to values from literature and related to the results of the electrical model of the DBD presented in Chapter 2.

3.2. Experimental setup

The PlasmaLine® source was already described in Chapter 2. Very high dissipated power densities between 60 and 100 W/cm^3 are reached in the discharge, as determined from Q-V diagrams, with the maximum discharge volume of 6 cm^2 corrected by the fractional surface coverage β; see Chapter 2 for details. The nitrogen discharge itself is sealed off from the atmosphere by virtue of the large gas flow, while the plasma jets emerging from the DBDs are exposed to the surrounding air. The N_2 process gas is 99.999% pure, with contributions of < 3 ppm O_2 and < 2 ppm H_2O [85]. A schematic of the plasma source is shown in Figure 3.1. The setup is placed inside a ventilation cabinet with an exhaust flow of 5 m^3s^{-1}. The relative

humidity RH of the ambient air in the lab is ~ 50% at a temperature of 20°C.

Spectra of the discharge between 200 and 850 nm are obtained using an ANDOR Shamrock SR-303i spectrograph with a 150 lines/mm grating and 500 nm blaze combined with an ANDOR iStar DH734-18-03 intensified CCD camera through a fiber optic cable with an 18° collection angle a distance of 10 cm from a discharge slit. This is depicted schematically in Figure 3.1, optical setup (I). Exposure times for these measurements are 50 ms for 300 - 500 nm and 10 s from 500 - 850 nm with maximum intensifier gain. Since the brightness of the discharge is very high, no collection optics are needed to obtain qualitative spectra. To obtain spectra of the jet, or flowing afterglow, a higher sensitivity is needed. In dark conditions, the afterglow is barely visible to the naked eye as a 5 mm long plasma jet. To characterize the emission, two plano-convex lenses with a focal length of 30 cm and an aperture size of 2 mm are used to image the side of a single jet onto an optical fiber, see Figure 3.1, optical setup (II). Exposure times of 0.4 s and 300 accumulations at the maximum intensifier gain are required to obtain the spectra. The focal point of this setup is located approximately halfway along the length of the jet and 1 mm from the source exit. The optical path is covered to block any ambient stray light or direct and reflected light from the discharge. Because the imaged area is 1 mm wide, the spectra represent the averaged emission over what is likely a wide range of species densities, therefore no absolute calibration of the spectra is attempted. For all spectra the wavelength range of 200 - 850 nm is achieved in four separate measurements (180 - 400 nm, 400 - 500 nm, 500 - 700 nm and 700 – 850 nm) and appropriate filters are used for each measurement to prevent higher order diffraction peaks. The quantum efficiency of the iCCD is effectively zero from 900 nm and above, so no spectra are obtained in this wavelength region. The position of the fiber in optical setup (I) was chosen such that the optical collection volume for this measurement was approximately equal to that of optical setup (II); ~ 0.1 cm^3 in both cases. Direct 2D imaging of the jet is carried out using the same ANDOR iStar iCCD camera in combination with a Tamron 70-300 mm Macro lens. The camera is aligned parallel to the source exit using an alignment laser

in combination with position markers; see Figure 3.1, optical setup (III). An optical filter is used to block any emission below a wavelength of 450 nm. The exposure time is set at 0.5 s, with 500 accumulations at the maximum intensifier gain of 255. The resulting image has a resolution of 400 pixels/cm, with the jet being imaged onto the 13.3 x 13.3 mm CCD at approximately 1:2.

For analysis of the 2D jet images, a custom-built Hot-Wire (HW) anemometer flow sensor is used to determine both the effective width of the plasma jet and the gas flow velocity between 0 and 6 mm from the source exit. The device is calibrated using a well-defined flow. The flow sensor is discussed in more detail in [86]. The flow data is used to calculate the time-of-flight of particles as a function of distance to the source exit.

3.3. Results

3.3.1 Qualitative analysis of spectra

Typical optical emission spectra for the discharge and jet are depicted in Figure 3.3. At all applied voltage amplitudes (8.4 to 11.6 kV) the spectra are qualitatively equivalent. The spectra show contributions from the NO γ system, $NO(A\ ^2\Sigma^+ \rightarrow X\ ^2\Pi)$, NO β system, $NO(B\ ^2\Pi \rightarrow X\ ^2\Pi)$, First Negative System (FNS), $N_2^+(B\ ^2\Sigma_u^+ \rightarrow X\ ^2\Sigma_g^+)$, Second Positive System (SPS), $N_2(C\ ^3\Pi_u \rightarrow B\ ^3\Pi_g)$, First Positive System (FPS), $N_2(B\ ^3\Pi_g \rightarrow A\ ^3\Sigma_u^+)$ and the Herman Infra-red system (HIR), $N_2(C^{"}\ ^5\Pi_u \rightarrow A'\ ^5\Sigma_g^+)$ [87,88]. No emission from water-related species, such as the $OH(A\ ^2\Sigma^+ \rightarrow X\ ^2\Pi$) transition expected at 306 nm, is evident from these spectra [88]. All excited states will hereafter be referred to as NO(A), NO(B), N_2(A), N_2(B), N_2(C) and $N_2(C^{"})$.

The bulk of the SPS and FPS emission observed in the discharge spectrum is the direct result of electron excitation processes, while HIR is exclusively the result of $N_2(C^{"})$ production via energy-pooling reactions of N_2(A) metastables in the post-discharge phase [89–93]:

$$N_2(A) + N_2(A) \rightarrow N_2(C", C, B) + N_2 . \tag{R1}$$
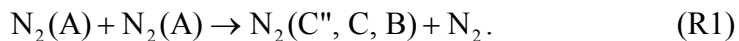
The spectrum of the jet is also depicted in Figure 3.3 and is very similar to the spectrum reported by Ricard *et al.* obtained from an N_2 afterglow at roughly the same distance from the source in terms of time-of-flight of the active species (< 1 ms from source exit) [83]. The FPS emission lines between 500 and 650 nm indicate the presence of highly vibrationally excited $N_2(B, v' \geq 10)$. This is a clear signature of ground-state atomic nitrogen recombination in the late, or Lewis-Rayleigh afterglow via the reaction [82]:

$$N + N + M \rightarrow N_2(X, A, B) + M \qquad (R2)$$

$$N_2(B) \rightarrow N_2(A) + h\upsilon(FPS) \qquad (R3)$$
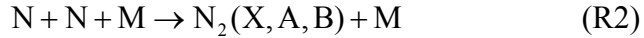
where M is a third particle, either N_2 or O_2. Reaction R2 will lead to overpopulation of the $N_2(B, v' = 11)$ state, as is clearly observed in Figure 3.3(b) [94]. In a Lewis-Rayleigh afterglow the excited N_2 species are created without any significant contribution of the metastable $N_2(A)$ energy pooling reaction R1, so that, contrary to the discharge spectrum, reaction R2 is the sole source of FPS emission [95]. Even within 1 mm of the source exit, the contribution of the energy pooling reaction R1 is negligible, which will be tested further below.

3.3.2 Quantitative analysis

Since we can conclude from the spectrum of the jet in Figure 3.3 that the plasma is in the late afterglow phase within 1 mm of the source exit, the emission intensity above wavelengths of 500 nm, I_{FPS}, can be used to quantify the atomic nitrogen concentration, via the concentration of $N_2(B)$:

$$I_{FPS}(t) = k_{R3}[N_2(B)](t) , \qquad (3.1)$$

with k_{R3} the Einstein coefficient for spontaneous emission of reaction R3. The creation of $N_2(B)$ is the result of recombination of atomic N, via reaction R2. The concentration of atomic N will decay according to the differential equation:
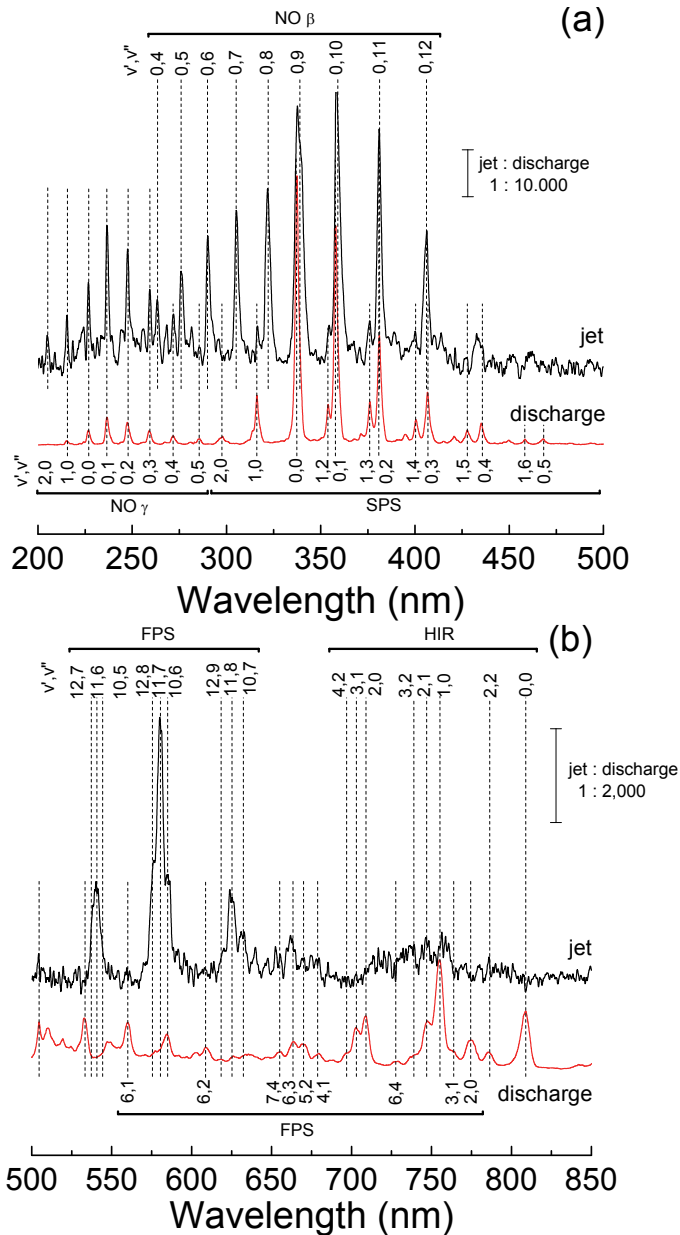
Figure 3.3: *Optical emission spectra of the DBD discharge and jet at an applied voltage amplitude of 11.6 kV, (a) between 200 - 500 nm and (b) between 400 - 850 nm. The relative vertical scales between the different plasma regions is indicated in each figure.*

$$\frac{\partial [\mathrm{N}](t)}{\partial t} = -2k_{R2}[\mathrm{M}]\big([\mathrm{N}](t)\big)^2 . \tag{3.2}$$

Note that we assume here that O_2 and H_2O and, hence, NO concentrations are sufficiently low that additional loss channels for atomic N need not be considered. This assumption will be tested at a later point, using a 1D convection-reaction model. Solving Equation (3.1) gives:

$$[\mathrm{N}](t) = \frac{[\mathrm{N}]_{source}}{1 + 2k_{R2}[\mathrm{M}][\mathrm{N}]_{source}\, t} , \tag{3.3}$$

where $[\mathrm{N}]_{source}$ is the atomic nitrogen concentration at the source exit. For an accurate determination of $[\mathrm{N}]_{source}$ it is critical to know the value of k_{R2}, which determines the total loss rate of atomic N. A value on the order of $4 \cdot 10^{-33}$ $cm^6 s^{-1}$ at 300 K for k_{R2} is often cited, where $[\mathrm{M}] = [\mathrm{N}_2]$, which leads to underestimation of the decay rate of atomic N [54,96–98]. A literature study reveals that an average value on the order of $1.5 \cdot 10^{-32}$ $cm^6 s^{-1}$ can be assumed, based on direct measurement techniques such as NO titration and ESR [99–104]. Only about 1 in 6 recombinations of atomic N lead to an $N_2(B)$ state [98], though this ratio has no effect on the results presented here, only on the absolute intensity of the FPS emission.

Aside from reactions R2 and R3, the concentration of $N_2(B)$ is reduced by quenching reactions, of which the following is the most relevant under our conditions [97]:

$$\mathrm{N_2(B)} + \mathrm{N_2} \rightarrow \mathrm{N_2(A)} + \mathrm{N_2} \tag{R4}$$
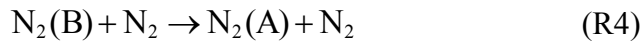
The rate coefficient of R4 for highly vibrationally excited $N_2(B, v' \geq 10)$ is approximately $3 \cdot 10^{-11}$ $cm^3 s^{-1}$ [92,105]. This reaction will far outweigh the loss rate due to spontaneous emission via reaction R3, at 10^5 s^{-1}. Quenching of $N_2(B)$ by oxygen- and hydrogen-containing species can be similarly neglected if the O_2 content is $\ll 10\%$. As we will show below, these conditions are met for the emission data. Reaction R4 with an N_2 concentration of $2.7 \cdot 10^{19}$ cm^{-3} predicts a 1/e
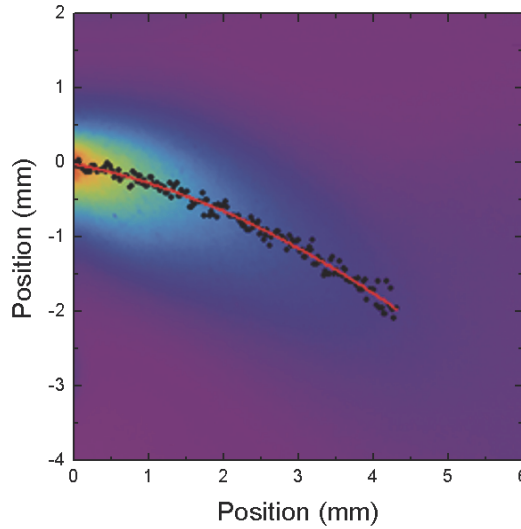
Figure 3.4: *iCCD image of the FPS emission intensity of the atmospheric plasma jet operated with a gas flow of 200 slm and an applied voltage amplitude of 11.6 kV. Black dots indicate the maximum value in each vertical column of pixels and the red line indicates a polynomial fit of these points, which consequently provides the trajectory of the gas flow.*

decay time for $N_2(B)$ of ~ 1 ns. At a flow rate on the order of 5 m/s, this leads to only a few tens of nanometers of displacement between creation and destruction. We can, therefore, use a steady-state approximation for the $N_2(B)$ concentration at any point in the plasma jet. Via reaction R2 and Equation (3.3), the relation between I_{FPS}, $[N_2(B)]$ and $[N]$ is then simply:

$$\frac{1}{\sqrt{I_{FPS}(t)}} \propto \frac{1}{\sqrt{[N_2(B)](t)}} \propto \frac{1}{[N](t)} \propto \left(1 + 2k_{R2}[N_2][N]_{source}t\right). \quad (3.4)$$

For simplicity, we assume the only third particle is N_2 [98]. Equation (3.4) shows that the decay of $(I_{FPS})^{-1/2}$ with time-of-flight from the source exit is a direct measure of $[N]_{source}$.

47
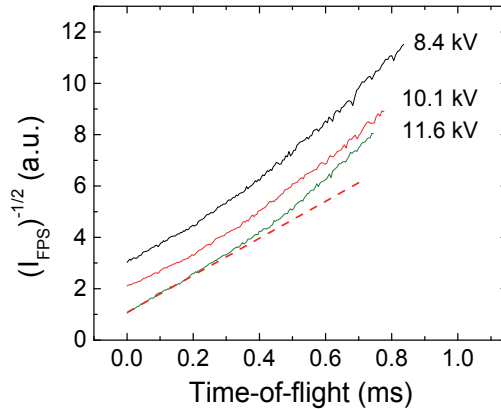
Figure 3.5: *Inverse square root of the FPS emission intensity as a function of time-of-flight on the center streamline of the jet at a flow rate of 200 slm. The data sets are translated on the vertical axis for clarity. The dashed line is a linear fit of the 11.6 kV data between 0 and 0.18 ms. The upward deviation of the data with respect to the initial linearity is due to increased losses of atomic N.*

An example of I_{FPS}, imaged using the iCCD camera with a macrolens (Figure 3.1, optical setup (III)), is shown in Figure 3.4. The spatial resolution is 40 pixels/mm. The conversion of this data to plots of $(I_{FPS})^{-1/2}$ as a function of time-of-flight in the jet, by making use of HW anemometer measurements, is treated in the Appendix. The final results for three applied voltage amplitudes are depicted in Figure 3.5. The $I_{FPS}(t)$ can only be determined up to ~ 4.5 mm (0.8 ms) from the source, as the emission intensity drops below the detection limit at this point.

Since the initial slope of $(I_{FPS})^{-1/2}$ in Figure 3.5 is indeed constant, and assuming the initial O_2 and H_2O concentrations in the process gas (at 3 ppm and 2 ppm, respectively) are negligible, this slope is a direct measure of the atomic N concentration in the source, [N]$_{source}$, via equation (3.4). The results are depicted in Figure 3.6 for a wide range of applied voltage amplitudes. The error bars in [N]$_{source}$ are due to the uncertainty in gas flow velocity and the fitting error of the initial slope, but do not include the systematic inaccuracy in recombination rate constant k_{R2}.
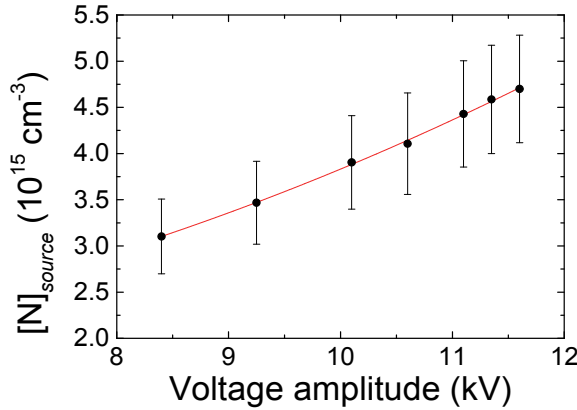
Figure 3.6: *Atomic nitrogen concentration at the source exit [N]$_{source}$ as a function of applied voltage amplitude in the DBD. The line is a guide to the eye.*
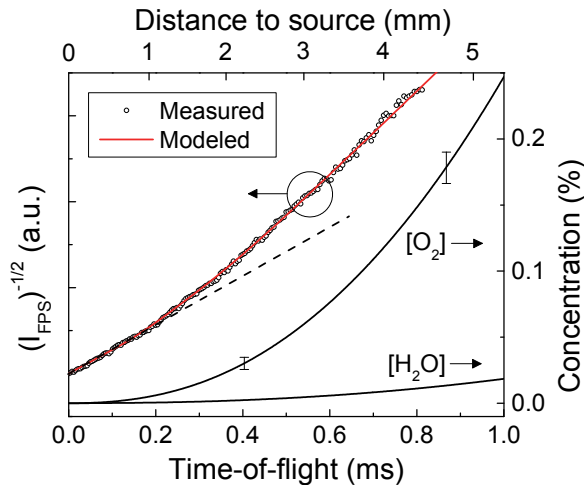
Figure 3.7: *Fit of [N$_2$(B)]$^{-1/2}$ to (I$_{FPS}$)$^{-1/2}$ at an applied voltage amplitude of 10.1 kV using the 1D convection-reaction model (left ordinate) and the increasing admixture of [O$_2$] and [H$_2$O] in the plasma jet leading to this fit (right ordinate). The 3 ppm [O$_2$] and 2 ppm [H$_2$O] contamination of the process gas is also taken into account. The fitted atomic N from the source, [N]$_{source}$, is 3% lower than expected from Equation (3.4).*

To check whether energy pooling from N$_2$(A), and chemical reactivity from admixture of O$_2$ and H$_2$O can be truly neglected in the above analysis, a 1D convection-reaction model containing 380 chemical reactions and 59 species is used. This model is described in detail in

the Appendix, section A3.2. In short, it is assumed that the decay of the emission on the center streamline of the jet can be described by solving a 1D chemical kinetic model over time, neglecting diffusion of species away from the center streamline. The results of this model are depicted in Figure 3.7. The O_2 and H_2O admixture remains well below 1% and, including energy pooling of $N_2(A)$, leads to no more than a 3% overestimation of $[N]_{source}$ in Figure 3.6, which is within the measurement error. The degree of dissociation of N_2 is less than $2 \cdot 10^{-4}$ based on this data, so that depletion of N_2 does not need to be considered.

3.4. Discussion

To evaluate $[N]_{source}$, obtained using 2D imaging, a comparison is made to published data on atomic N concentrations from various atmospheric pressure plasma sources obtained using conventional techniques, such as NO titration, absolute optical emission, or TALIF. This data is summarized in Table 3.1, where only the results for maximum $[N]_{source}$ are included. Though our values for $[N]_{source}$ are significantly higher than those of other DBD sources, they are well below those obtained using microwave plasma on Ar-N_2 mixtures [106]. With respect to the DBD sources in [79,80] and [96], these have estimated dissipated power densities of 8 W/cm^3 and 2 W/cm^3, respectively, while the PlasmaLine® source achieves 90 W/cm^3. Furthermore, the DBD geometry in [79,80] is cylindrical, but with a gap width of 1 mm, twice the minimum gap width of the PlasmaLine®, while the DBD in [96] has a planar geometry with a gap width of 2 mm. It seems plausible that DBD geometry can affect N concentration, even if only through a reduction of the dissipated power per volume of gas. In light of the above comparison, the absolute values of $[N]_{source}$ obtained using the 2D imaging technique appear reasonable, though we are mainly interested in the production efficiency of atomic N, not its absolute value.

To determine the production efficiency of atomic N in the DBD source, the specific energy input per N atom, E_N, is calculated using

Table 3.1: *Comparison of maximum atomic N concentrations from various plasma sources operated at atmospheric pressure. The energy input per N atom from the source E_N is given in eV/atom. It is assumed that the surface coverage $\beta = 1$ in all cases, though this is only certain for the results obtained in this work.*

Source type	Gas	$[N]_{source}$ $(10^{15}$ cm$^{-3})$	Method	P (W)	Φ (slm)	E_N (eV/atom)	Ref.
DBD	N$_2$	4.5	Emission	500	200	320	This chapter
DBD	N$_2$	1.0	NO titration	60	68	360	[79,80]
DBD (Townsend)	N$_2$	≤ 0.3	TALIF	1.5	variable	830	[96]
DBD (Filamentary)	N$_2$	≤ 0.3	TALIF	1.6	variable	300	[96]
Corona	N$_2$	0.5	NO titration	15	45	280	[81,182]
Electron beam	N$_2$	2.7	NO titration	600	2	420	[183]
Microwave	Ar, 0.3% N$_2$	17	NO titration	200	10	440	[106]
Arc discharge	He, 1.3% N$_2$	4.8	Calibrated emission	200	30	510	[184]

$$E_N = \frac{P}{\beta \Phi [\mathrm{N}]_{source}} \ , \tag{3.5}$$

where P is the input power in the system in W, Φ is the gas flow rate through the system in slm, β the surface coverage of the discharge as determined in Chapter 2, and $[\mathrm{N}]_{source}$ the steady-state atomic N concentration in the source, depicted in Figure 3.6. Note that the ratio of power P to the product of surface coverage and gas flow, $\beta\Phi$, is a measure of the energy-input per volume of gas and effectively takes into account the residence time of particles in the discharge. Values of E_N are included for all cases in Table 3.1, but it is assumed that $\beta = 1$, since no information regarding the surface coverage is provided in the cited publications. It can be seen that E_N is on the order of $300 - 500$ eV/atom, irrespective of the type of source or gas composition, though the DBD in Townsend mode is less efficient at 800 eV/atom [96]. It can be concluded that the atomic N production efficiency measured here falls within the expected range. A theoretical value of (240 ± 30) eV/atom was determined by Tsyganov *et al.* using a zero-dimensional chemical kinetic model of a uniform discharge in N$_2$ at atmospheric pressure [107]. This model assumes E-fields of < 35 kV/cm, based on gap voltage divided by gap width, and neglects the much higher transient E-fields which locally occur in filamentary
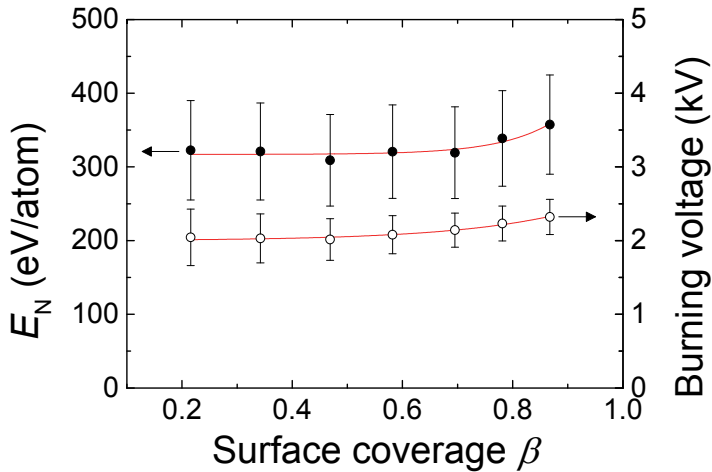
Figure 3.8: *The atomic N production efficiency E_N and the burning voltage of the discharge U_b as a function of surface coverage β. The surface coverage depends only on the applied voltage amplitude of the DBD. The lines are guides to the eye.*

microdischarges. The correspondence with the experimental values presented here is quite striking, however, which suggests that such simplifications can be made in chemical kinetic models of filamentary DBDs.

For variable β, the results of Equation (3.5) are depicted in Figure 3.8. While there is a clear increase in [N]$_{source}$ with increasing applied voltage amplitude, as depicted in Figure 3.6, the specific energy E_N is nearly constant. In other words, the increase in [N]$_{source}$ can be accounted for solely by an increase in the areal extent of the discharge, while the discharge itself, or the individual microdischarges it is composed of, remain unchanged. This is consistent with the results of Chapter 2, where it is shown that the burning voltage U_b of the discharge remains constant, independent of the applied voltage amplitude. The burning voltages U_b, obtained for the conditions used in this work, are also plotted in Figure 3.8. Since the burning voltage U_b is directly related to the reduced electric field, which determines the electron energy distribution function (EEDF) [58,59], it can be expected to determine the dissociation efficiency of N_2 for individual microdischarges. A similar independence of

production efficiency on applied voltage has been observed for both O_3 generation [62] and CO_2 dissociation [6] in DBDs.

3.5. Conclusions

It has been shown that direct 2D imaging of the FPS emission in a nitrogen atmospheric pressure plasma jet can be used to obtain atomic N concentrations in the source, $[N]_{source}$. An upper limit on the admixture of surrounding air in the jet can also be determined, where in the first 1 mm from the source O_2 and H_2O do not significantly affect the FPS emission. The obtained values of $[N]_{source}$ are in reasonable agreement with those obtained in other atmospheric pressure plasma sources using conventional techniques.

For the pure nitrogen jet used here, the specific energy input per nitrogen atom is found to be (320 ± 20) eV/atom, close to the theoretical minimum and comparable to the specific energy for other atomic nitrogen sources in the literature. More importantly, we observe that the specific energy does not depend on applied voltage amplitude. This is consistent with the electrical model presented in Chapter 2, where the burning voltage U_b remains constant as a function of applied voltage and only the surface coverage of the discharge increases. It is concluded that radical production is entirely determined by the density of microdischarges on the electrode surface, while individual microdischarges do not change significantly with voltage.

Appendix to Chapter 3

A3.1 Conversion of position to time-of-flight

For data analysis of the 2D images of the $N_2(B)$ emission, or I_{FPS}, the center streamline is determined by taking the point of maximum intensity along each vertical column of pixels in Figure 3.4 and fitting a third-order polynomial function $f(x)$ through these points. We then average the intensity over 4 pixels (0.1 mm) above and below this polynomial to obtain the I_{FPS} as a function of path length along the center streamline, where path length is calculated using the expression:

$$s(x) = \int_0^x \sqrt{1 + \left(\frac{\partial f(x')}{\partial x'} \right)^2} \, dx', \qquad (A3.1)$$

with x the distance to the source.

To apply Equation (3.3), described in the main text, to the optical emission data, the I_{FPS} as a function of path length must be converted to a function of time-of-flight from the source exit, *i.e.* the time it takes a test particle to reach a particular point along the streamline. For this purpose, cross-sectional flow velocity profiles of the jet are measured at various distances from the source using a calibrated flow sensor. These flow measurements are discussed in greater detail in [86]. Gaussian fits of these profiles provide peak velocity and FWHM at each point along the jet, results of which are depicted in Figure A3.1. The FWHM is corrected for the angle between streamline and measurement direction at each point. A suitable function $g(s)$ is fitted to the velocity data to obtain peak velocity as a function of path length s, which can then be used to convert to time-of-flight, t, via:

$$t(s) = \int_0^s 1 / g(s') ds'. \qquad (A3.2)$$
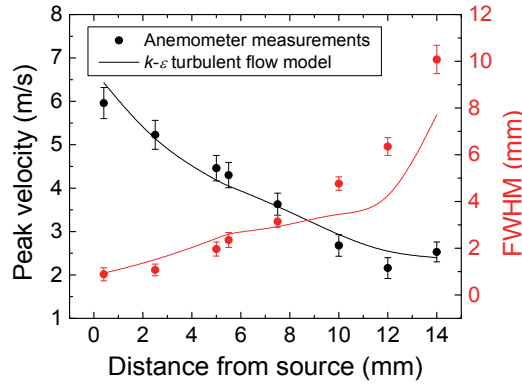
Figure A3.1: *Results of hot-wire anemometer measurements of the flow velocity in the jet as a function of distance from the source. All data is derived from cross-sections parallel to the center streamline and takes into account only a single jet. The lines are the results of a numerical k-ε model presented in [86].*

The additional step of first converting distance to path length along the streamline is necessitated by the large curvature of the jet, caused by underpressure in the region between the two jets. There is also a factor ~ 1.5 increase in FWHM between source exit and 4.5 mm downstream, which could present an additional loss channel for N and $N_2(B)$ along the center streamline. This loss is minimal during the first 1 mm from the source, since FWHM is relatively constant here.

A3.2 Chemical kinetic model

To check whether energy pooling from $N_2(A)$, and chemical reactivity from admixture of O_2 and H_2O can be neglected, an extensive chemical kinetic model is used. It is assumed that the decay of the emission on the center streamline of the jet can be described by solving a 1D chemical kinetic model over time, neglecting diffusion of species away from the center streamline:

$$\frac{\partial[X]}{\partial t} = \sum_i k_i [Y]_i [Z]_i - \sum_j k_j [Y]_j [X] + S_X . \tag{A3.3}$$

In this equation t is time-of-flight, [X], [Y] and [Z] are species concentrations as function of t in units of cm^{-3}, k_i and k_j reaction rate

Table A3.1: *Species considered in the 1D chemical kinetic model. The top rows show all species for which a non-zero initial value is used at t = - 0.2 ms from the source exit.*

Species	N	O_2	H_2O	N_2	$N_2(A)$	e	N_4^+
Initial value (cm^{-3})	from fit	$7.5\cdot10^{13}$	$5\cdot10^{13}$	$2.5\cdot10^{19}$	10^{15}	10^{13}	10^{13}

Species (zero initial value)	**Ground state:** O, O_3, NO, NO_2, NO_3, N_2O, N_2O_5, OH, HO_2, H, H_2, H_2O_2, HNO, HNO_2, HNO_3
	Excited: $N(^2D)$, $N(^2P)$, $O(^1D)$, $O(^1S)$, $O_2(a)$, $O_2(b)$, $N_2(B)$, $N_2(C)$, $N_2(a')$, NO(A), NO(B)
	Charged: N^+, N_2^+, N_3^+, O^+, O_2^+, $O_2^+(N_2)$, O_4^+, NO^+, $NO^+(N_2)$, $NO^+(O_2)$, NO_2^+, N_2O^+, H^+, H_2^+, H_3^+, H_2O^+, H_3O^+, OH^+, O^-, O_2^-, O_3^-, O_4^-, NO^- NO_2^-, NO_3^-, H^-, OH^-

coefficients leading to creation or destruction of species X in units of cm^3s^{-1} and S_X a time-dependent source term for species X in units of $cm^{-3}s^{-1}$, where applicable. In some cases reactions i and j are 1st or 3rd order instead of 2nd order and the units of k change accordingly. Equation (A3.3) is solved for 59 species, which are listed in Table A3.1. The 380 reactions and rate coefficients are listed on pages 157-168 of this thesis, where a constant gas temperature of 320K is assumed throughout the streamline.

Electrons are assumed to be cold, with T_e = 0.1 eV, so that electron impact reactions are neglected. The initial concentration of $N_2(A)$ in the discharge is taken from literature values for N_2 DBDs and is 10^{14} - 10^{15} cm^{-3} [108–111]. As can be seen in the schematic of Figure 3.1, the electrodes of the DBD do not extend towards the source exit but are receded by at least 1 mm. In terms of time-of-flight, $[N_2(A)]$ has been decaying for at least 0.2 ms before the starting point of the jet measurements. The initial conditions for the modeled species are therefore set at t = - 0.2 ms, as listed in Table A3.1. The increased admixture of O_2 and H_2O for $t > 0$ is taken into account by including suitable source terms S_{O_2} and S_{H_2O} for both these species. A relative
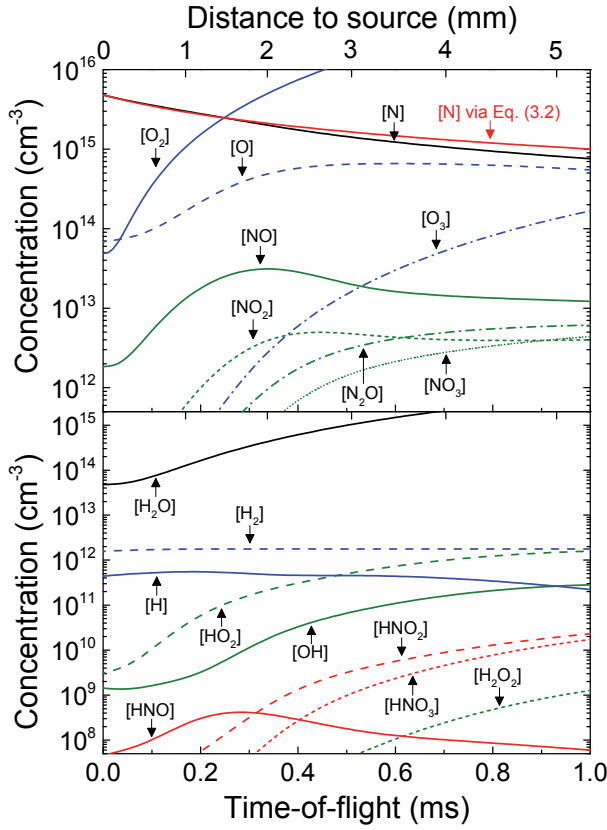
Figure A3.2: *Calculated ground state species concentrations in the jet using the 380-reaction model, with O_2 admixture from the surrounding air according to the fit in Figure 3.7. The red line near [N] indicates the atomic N concentration as it would be following Equation (3.2) from the main text, in the absence of O_2, H_2O and $N_2(A)$.*

proportion $S_{H_2O}/S_{O_2} \approx 0.074$ is assumed, corresponding to the conditions of the ambient air in the lab, with RH $\approx$ 50% at 20°C. The source term S_{O_2} is the time-derivative of the generalized logistic function, which gives a shape of the O_2 and H_2O uptake similar to the uptake of O_2 measured by Ellerweg *et al.* for a He plasma jet in ambient air [112]:

$$S_{O_2}(t) = \frac{\partial}{\partial t}\left(\frac{[O_2]_{max}}{1+(\tau/t)^a} \right), \tag{A3.4}$$

where $[O_2]_{max}$ is always set to the ambient level of 21% O_2, or $5.2 \cdot 10^{18}$ cm^{-3}. The time constant τ and the exponent a, along with $[N]_{source}$, are the three fitting parameters in the model. Best fits to the $N_2(B)$ concentration are obtained for $\tau \approx 6.7$ ms and $a \approx 2.3$ and $[N]_{source}$ only 3% lower than determined in the main text of this chapter. Calculated ground state species concentrations for an applied voltage amplitude of 10.1 kV between $t = 0$ and 1 ms are depicted in Figure A3.2. The initial concentration of electrons and ions, as well as the initial and final concentration of H_2O, have no appreciable effect on the $N_2(B)$ concentration. The main effect of the admixture of O_2 on $N_2(B)$ occurs via the formation of O and NO, which scavenge N via reactions R13, R14 and R6 in the list of reactions on pages 156-167. The effect of $N_2(A)$ is limited to increased dissociation of O_2 via reaction R85 and only slightly enhances $N_2(B)$ concentrations through the energy pooling reaction R1 in the main text.

Chapter 4

Charge Distributions in Planar DBDs as a Function of Filament Density

Since the physical properties of individual filaments in a DBD determine chemical process efficiency, knowledge of the statistical distribution of these physical properties over a large number of filaments is desirable. In this work, the transferred charge/pulse of individual filaments in the discharge gap is measured and statistical distributions are obtained for high filament number densities of up to 200 filaments/cm^2/cycle in air at 100 kHz. Log-normal distributions are observed for all DBD configurations studied, contrary to the normal distributions found in previous studies at lower filament number densities. With increasing applied voltage amplitude, the charge/pulse distributions remain unchanged and only the filament number density is seen to increase. Altering DBD geometry has a limited effect on the charge/pulse distributions, while burning voltage remains unaffected.

4.1. Introduction

The most interesting property of Dielectric Barrier Discharges (DBDs) is that, in most gases at atmospheric pressure, the plasma consists of many small, transient microdischarges with diameters of ~ 0.1 mm and durations on the order of 10 ns [51,113]. The short duration of these microdischarges, or filaments, combined with their large number density, is assumed to allow for a description of the DBD as a continuous plasma. This is done in *e.g.* equivalent circuits for DBDs where the gas gap is described as a single component with a constant voltage drop across the entire surface area, instead of the localized voltage drops that would occur for each individual filament, see, for instance, Chapter 2 of this thesis and [39,72]. Similarly, several modeling studies of DBDs assume the plasma to be a continuous medium at atmospheric pressure [107,114,115], an approach which may lead to large errors when considering that *e.g.* electron density and temperature are locally much higher within discrete filaments than they are in a continuous plasma with equal conduction current density. A number of modeling studies focus on the electrical dynamics of individual filaments [33,61,113,116–118], or their chemistry [60,62]. The relationship between these studies and the behavior of the DBD as a whole will depend on the variation between individual filaments and their number density over the electrode area [49]. As observed in Chapter 3, the physical properties of individual filaments appear to determine chemical process efficiency, while little variation in this efficiency is apparent as a function of applied voltage. In fact, the only control over radical production was determined by the filament number density. Here, we aim to test this observation further by studying the characteristics of a large number of filaments for a given DBD configuration. Furthermore, we will study the effect of different DBD geometries and dielectric materials on the filament distributions and burning voltages, in order to assess the degree to which DBDs can be controlled or optimized for a given process.
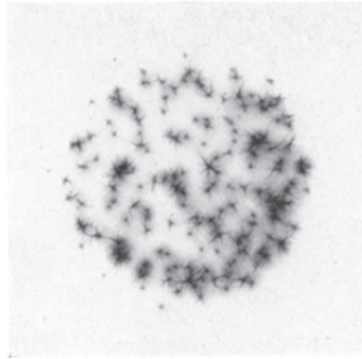
Figure 4.1: *Lichtenberg image of the footprints of individual filaments in a 34 mm diameter DBD in air obtained by Buss [120]. The number density of filaments is estimated at 15 cm^{-2} for a single discharge cycle.*

The present study is restricted to ambient air as process gas with no humidity control. Compared to filamentary discharges in pure nitrogen, both the average duration and transferred charge of filaments in air can be a factor of 2 - 4 shorter, while *Q-V* diagrams of the complete discharge are nearly identical [70,119]. Air will therefore have a 2 - 4 times higher filament number density compared to N_2. Increased humidity can lead to higher transferred charge and lower filament number density [39,70].

The number density of filaments in a DBD was first studied by Buss, who discovered that DBDs consist of individual microdischarges [120]. In his work, both electrodes were covered by photographic glass plates with a gas gap of 1 mm and subjected to a 10 kV stepped voltage, resulting in a single discharge. A Lichtenberg image, tracing the light intensity of individual filaments on the dielectric surface, is reproduced in Figure 4.1. Based on this image, a number density of 15 filaments/cycle/cm^2 can be determined. Similar photographic methods to obtain the number density of filaments have been applied by several authors [11,50,113,121], which, depending on applied voltage, result in number densities between 3 - 40 filaments/cycle/cm^2 for glass or quartz electrodes in air at atmospheric pressure. With increasing applied voltage, filament footprints tend to overlap during a half-cycle, so that accurate counting becomes difficult. Another obvious drawback of this method is that the physical properties of the

62
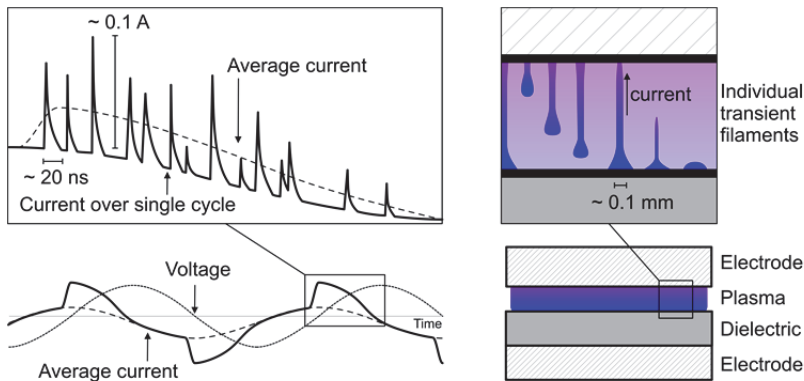
Figure 4.2: *Schematic of the applied voltage over and current through a DBD system, with a detail of the current pulses resulting from individual filaments (left). Schematic of a DBD system showing the development of individual filaments during a discharge (right). Current is only observed while a filament connects the two electrodes.*

individual filaments, such as the transferred charge, cannot be determined from these images. Also, since Lichtenberg images can only be obtained for one, or a few, discharge cycles, a statistically significant sample of the number density, or its development over time, is not easily obtained. An alternative approach would be to monitor the current through the DBD. Since the appearance of a filament in the gas gap leads to a corresponding 10 - 100 ns current pulse, the number density and transferred charge per filament can be derived from the current as a function of time. Current, voltage and a visual representation of the plasma are depicted schematically in Figure 4.2 for a planar DBD geometry, where the top-left box shows a detail of the current over time. In this depiction, filaments are sufficiently spread out over time so that they can be individually distinguished. Since this is not necessarily the case, previous studies of filamentary current are restricted to geometries favoring a single filament per voltage cycle. For example, Höft *et al.* use two spherical electrodes leading to a single filament per pulsed voltage cycle, with the transferred charge/filament following a Gaussian distribution [122]. Akishev *et al.* have a similar approach, using a sinusoidal voltage cycle, but only obtain the probability over time for the appearance of the single filament within the voltage half-cycle [121]. Hirth, Eliasson *et al.* and Braun *et al.* all use a small diameter current

probe embedded in a larger planar DBD, but only show data for individual current pulses, without rigorous statistical analysis [62,113,123]. Gibalov and Drimal *et al.* use electrode diameters up to 1.6 cm are used, but transferred charges from individual filaments are not obtained directly. Instead, the average charge of filaments is inferred from the surface charge on the dielectric at low filament number density and low frequencies of 50 Hz [124–127]. Jidenko *et al.* measure the current through a 3 cm^2 DBD and extract the charge/pulse using digital post-processing [128]. At voltages above the discharge ignition voltage, they encounter large number densities of filamentary current pulses, making it difficult to distinguish them individually. In addition, their work is restricted to symmetric DBDs, with both electrodes covered by dielectric material, while the asymmetric case is also of interest.

In this work, a different approach is taken to determine number density and transferred charge per filament. The discharge current from the DBD is passed through an analog circuit, termed Pulse Height Analyzer (PHA), which provides block-like pulses with a height equivalent to the transferred charge/pulse to an analog-to-digital-converter (ADC). This eliminates the need for digital post-processing and results in a time-resolution of 50 ns. Furthermore, statistically significant samples of filamentary current pulses can be obtained at any point within a half-cycle, so that the development of the charge/filament distributions can be monitored over time. To prevent overlapping of filamentary current pulses, as observed by other authors, electrode diameters in this work are between 3.0 and 6.0 mm. The focus is on asymmetric DBDs operated at 100 kHz, with the secondary electrode covered by either alumina or quartz, but results for symmetric DBDs are presented as well. Using thin dielectrics, high plasma current densities up to 32 mA/cm^2 are reached, for which charge/pulse and number density are reliably measured with errors below 20%.

This chapter is structured as follows: After a discussion of the experimental setup, we will show the influence of applied voltage amplitude on the filamentary current pulses, as well as their variation as a function of the phase of the applied voltage. After discussing the
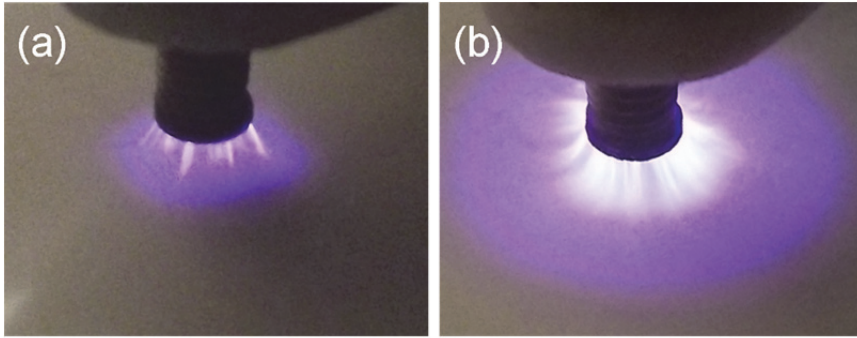
Figure 4.3: *Images of the DBD operated with a 1 mm air gap and a 1 mm alumina dielectric, with 100 kHz sinusoidal driving voltages of (a) 8 kV$_{pp}$, which is just above discharge ignition, and (b) 10 kV$_{pp}$. The top electrode has a diameter of 2.6 mm and the bottom electrode has a diameter of 20 mm.*

general characteristics of the filament distributions, we expand our analysis to include the effects of gap width, dielectric thickness and dielectric material. Finally, a discussion of the relationship between burning voltage and average charge/pulse is presented. We conclude with a summary of the most relevant observations.

4.2. Experimental setup

4.2.1 Small area DBD

A small area planar DBD with a custom generator and transformer circuit was built, providing sinusoidal applied voltages with peak-to-peak amplitudes between 1 - 10 kV$_{pp}$ at a frequency of 100 kHz to a brass top electrode of 3.0 or 6.0 mm diameter. Different bottom electrodes can be used, with diameters between 2.6 and 20 mm and are adjustable in height to provide various gap widths. One or both of the electrodes can be covered by dielectric material, which in this work consists of alumina and quartz of thicknesses between 0.5 and 2.0 mm, with relative permittivities, ε_r, of 10 and 4.2, respectively. The surface area of the dielectric material is large with respect to the electrode areas so that it always extends beyond the edges of the electrodes. To prevent unwanted discharging outside the air gap, above or underneath the dielectric, the spaces around the electrodes

are insulated using Teflon rings with silicone gel providing an air-tight seal. Examples of discharges in this system are shown in Figure 4.3, where a much larger bottom electrode is used so that the discharge spreads out and individual filaments are more easily distinguishable. Prior to any measurements, the DBD is allowed to heat up for several minutes to attain equilibrium. We therefore study only the steady-state behavior of the system.

4.2.2 Current measurements and PHA circuit

The DBD setup is integrated in the Pulse Height Analyzer (PHA) circuit, which is described in detail in the Appendix. This analog circuit determines the conductively transferred charge for many consecutive current pulses, termed charge/pulse, and plots the number of occurrences of a given charge/pulse in a histogram. This method is inspired by the BOL nuclear detection system developed in the 1970's by Nikhef [129–131]. The Appendix includes descriptions of the DBD plasma current measurements (Section A4.1), the components of the PHA circuit (Section A4.2), the calibration procedure (Section A4.3) and the influence of DBD electrode size on the PHA spectra (Section A4.4). Summarizing the Appendix, with the analog Pulse Height Analyzer circuit, charge distributions of filamentary DBDs in air can be accurately determined at high applied voltage frequency and amplitude of 100 kHz and 10 kV_{pp}, respectively. Two filaments may be counted as one when the filament number density is greater than 100 counts/cycle/cm^2, but this accounts for no more than 20% of filaments at 200 counts/cycle/cm^2, with little qualitative change in the distributions. Distributions measured with 6 mm diameter electrodes are very similar to those measured with 3 mm diameter electrodes, so that 3 mm electrodes are used for all subsequent measurements to minimize overlap of current pulses. Currently, the time resolution of the circuit is 50 ns. Though the circuit could be improved, the average duration of filamentary current pulses is similar. The PHA therefore operates at the physical limit for filamentary current analysis. To completely prevent overlap of current pulses, even smaller electrodes would need to be used, so that fewer filaments occur per cycle. This would, however, result in charge distributions more akin to single-filament distributions such as in [121,122].

Depending on DBD geometry, it is found that up to 75% of total plasma current during the negative half-cycle is not filamentary, but continuous in nature and can be identified as an Atmospheric Pressure Townsend Discharges, or APTD. This type of discharge does not contribute to the measured charge distributions presented in this chapter, because the PHA circuit is only sensitive to the rapid increases in current related to filaments, and the more gradual APTD current is filtered out. Since our interest here is in the statistical distribution of many interacting filaments, we focus the discussion on the positive half-cycle, though filamentary current pulses counted during the negative half-cycle are also presented. The APTD is discussed further in Chapter 5.

4.3. Results & discussion

4.3.1 Effect of applied voltage amplitude

Figures 4.4 and 4.5 depict the effect of increasing applied voltage on the charge distributions for DBDs with 1.0 or 0.6 mm alumina on the secondary electrode. For both dielectric thicknesses, overlapping current pulses in the PHA begin to occur from $N^+ > 100$ counts/cycle/cm^2, or 9 kV$_{pp}$ for 1.0 mm alumina and 8 kV$_{pp}$ for 0.6 mm alumina. At the highest plasma currents, overlap affects up to 20% of charge/pulse measurements during the positive half-cycle and 1 in every 5 filaments counted in the circuit actually consists of 2 filaments. However, the distributions do not change significantly as the voltages are increased above 9 kV$_{pp}$ (Figure 4.4) and 8 kV$_{pp}$ (Figure 4.5). In fact, the weighted average charge/pulse $<q_+>$ decreases from 0.8 nC to 0.7 nC for 1.0 mm alumina, and 1.0 nC to 0.9 nC for 0.6 mm alumina for lowest to highest applied voltage. If overlapping current pulses significantly affect the distributions, an increase in $<q_+>$ should become apparent, due to the adding up of the charge from several filaments in the PHA circuit. The distributions do not show any broadening at the high end of the charge/pulse spectrum, leveling off around 1.5 and 2.0 nC for both dielectric thicknesses, independent of applied voltage amplitude. Drimal *et al.*
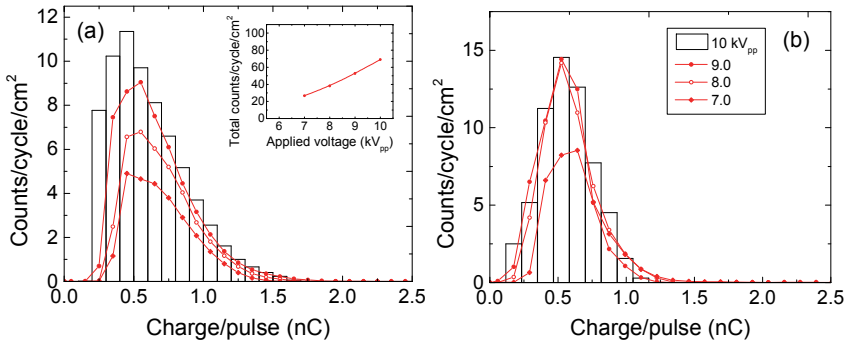
Figure 4.4: *Charge distribution for (a) positive current and (b) negative current for 1.0 mm alumina and a 0.6 mm air gap with increasing applied voltage amplitudes. The inset for (a) shows the total number of counts for the positive half-cycle as a function of applied voltage amplitude. Average plasma current increases from 0.3 mA (7 kV$_{pp}$) to 0.7 mA (10 kV$_{pp}$).*
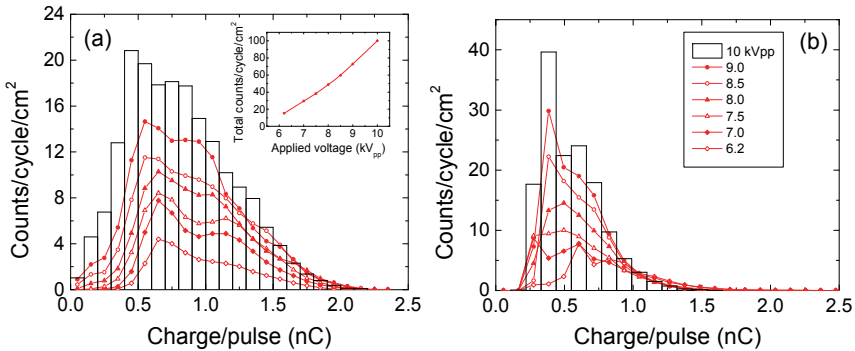
Figure 4.5: *Charge distribution for (a) positive current and (b) negative current for 0.6 mm alumina and a 0.6 mm air gap with increasing applied voltage amplitudes. Average plasma current increases from 0.4 mA (6.2 kV$_{pp}$) to 2.4 mA (10 kV$_{pp}$). The inset for (a) shows the total number of counts for the positive half-cycle as a function of applied voltage amplitude. For clarity, bars have been replaced by lines for all but the 10 kV$_{pp}$ data.*

and Jidenko *et al.* both observe secondary and tertiary peaks at higher charge/pulse in their distributions as a result of current pulses overlapping in time [124,128], where at least 30 times larger electrodes are used. It appears that, with the much smaller electrode area used here, filaments occurring at nearly the same time will reduce each other's charge/pulse. In other words, with filaments

occurring close together in both time *and* space, the adding up of the charge/pulse in the PHA of both filaments will not lead to a higher total charge/pulse than if a single filament occurred. This effect leads to little change in the charge distributions with increasing overlap of filaments in time. We can therefore conclude that filaments occurring simultaneously, up to several millimeters distant, significantly affect each other's dynamics. This effect is explained further in Chapter 5.

As observed in Figures 4.4 and 4.5, increasing the applied voltage leads to an increase in current through an increase in the number of filaments, *not* through an increase in the charge transferred by individual filaments. This same behavior as a function of applied voltage was observed for gap widths of 0.4 to 1.0 mm and alumina thicknesses of 0.6 to 2.0 mm. This is in agreement with the works of Drimal *et al*, Jidenko *et al.* and Akishev *et al*, where a nearly linear increase of filament number density is observed with increasing voltage [121,126–128] and is here confirmed to continue towards higher plasma current densities.

This is consistent with the observations made in Chapters 2 and 3, where it was found that both burning voltage U_b and N_2 dissociation efficiency E_N are independent of applied voltage amplitude. Here, we find that the average charge/pulse $<q_+>$ is also nearly independent of the applied voltage, with a decrease of 10% from lowest to highest applied voltage. Since the charge/pulse of a filament is the amount of charge that is moved to the opposite electrode before the electric field across the filament, and hence the burning voltage U_b, is quenched, it is reasonable to assume that the average charge/pulse is directly related to the burning voltage. The possibility of tuning the EEDF to a specific chemistry with a set DBD configuration is therefore limited, as was discussed in Chapter 3. The relationship between the average burning voltage during a half-cycle $<U_b>$ and charge/pulse $<q>$ for different DBD configurations and applied voltages is treated further at the end of this chapter.

4.3.2 Time dependence and log-normal distributions

In this section, the variation of charge/pulse with respect to the phase of the external voltage is studied. Figure 4.6 shows the normalized plasma current and applied voltage for the DBD with 0.6 mm alumina and 0.6 mm gap width at applied voltage amplitude of 8 kV_{pp} (~ 100 counts/cycle/cm^2). Indicated in this figure are the times at which distributions are obtained over 120 ns intervals at different points in the applied voltage cycle. The results of these 10 measurements are depicted in Figure 4.7. Each distribution is the average of the same 120 ns measurement window over $3.2 \cdot 10^6$ discharge cycles and therefore provides an accurate picture of the development of the discharge during a half-cycle. For the positive half-cycle, the discharge begins with current pulses at the low end of the distribution, as seen in (1), with the highest observed charge/pulse occurring after the average plasma current has reached its peak value, as seen in (4). This same behavior is reported by Akishev *et al*, where the highest current per filament and the highest filament number density is observed midway between discharge ignition and peak applied voltage [117,121]. Akishev *et al.* explain this via a single-filament model presented in [117] by showing that the phase of the external voltage at the moment of ignition is directly related to its peak current. A higher peak current very likely leads to a higher transferred charge, as shown by the data presented in Figure 4.7.

For each 120 ns interval, the distributions have multiple peaks as a function of charge/pulse. The total number of separate Gaussian-like peaks that can be identified in distributions (1) – (5) of Figure 4.7 is ~ 8, approximately equal to the average number of counts/cycle. This is in agreement with the results of Höft *et al.* and Akishev *et al*, who observe normal probability distributions for the charge of single filaments recurring in a single location [121,122]. The negative half-cycle has the bulk of its filamentary current pulses in the first ~ 1 µs of the discharge. At least half the total plasma current is not transferred via filamentary current pulses, but via APTD, which will be discussed further in Chapter 5.

The total averaged distributions (AVE) over the 4 µs measurement interval fit very well to a log-normal distribution, as depicted in
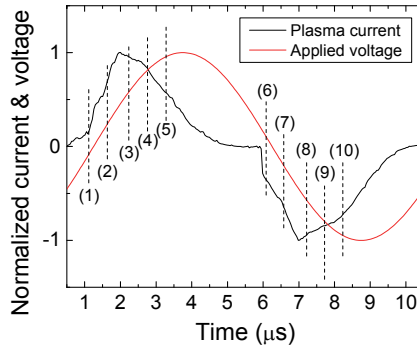
Figure 4.6: *Normalized plasma current and applied voltage over one cycle for a 0.6 mm air gap and 0.6 mm alumina on the secondary electrode at 8 kV$_{pp}$. The plasma current is averaged over 1024 cycles. Indicated by numbers (1) - (10) are the positions in time at which the charge/pulse distributions in Figure 4.7 are measured.*

Figure 4.7 for both positive and negative half-cycles. As a rule of thumb, the multiplicative standard deviation of the total averaged distributions $s^* \approx (1.4 \pm 0.4)$, where the lower limit of the distributions can be found at $<q_{+/-}>/2s^*$ and the higher limit at $<q_{+/-}>\cdot 2s^*$. So while individual filaments recurring in the same location exhibit transferred charges with a normal probability distribution, the aggregate of many filaments recurring in different locations will roughly follow a log-normal probability distribution.

Log-normal distributions develop for many systems undergoing growth over time. Examples include measures of length and weight of individuals within a species, the distribution of city sizes and the size distributions of coagulating aerosols [132–134]. In these cases, the origin of the log-normal distribution is an initial population of organisms, settlements or nucleation centers of normally distributed size, where the initially larger elements have a larger growth rate than the smaller elements, because growth rate is proportional to size. Progression over time then leads to a skewed distribution, because the elements at the higher end of the initial distribution reach proportionately greater sizes. It is interesting to note that in coagulation theory for aerosols, normal distributions of particle sizes within a closed system always progress toward a log-normal

71
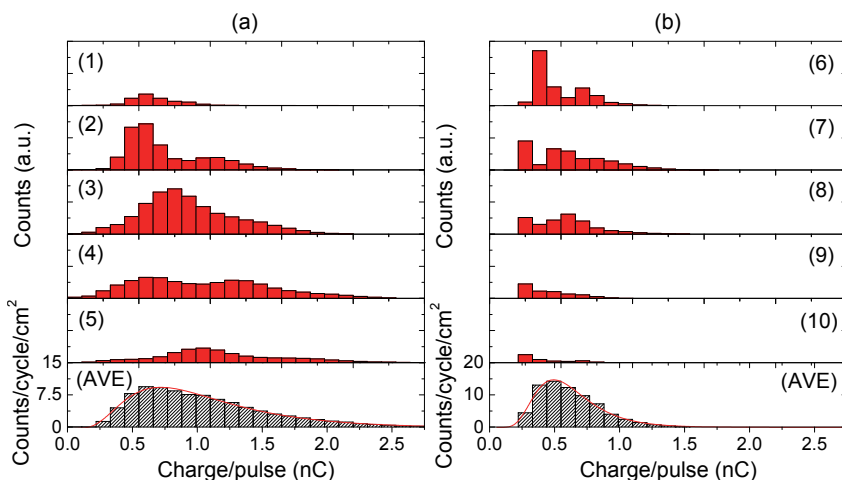
Figure 4.7: *Charge/pulse distributions over time for positive current, (1) - (5), and negative current, (6) – (10). The relative scale for positive and negative current is constant, with each distribution measured during 120 ns intervals at the points indicated in Figure 4.6. The bottom graphs in the figures shows the average distributions over the full 4 μs measurement interval, while the red lines are fitted log-normal distributions.*

distribution with multiplicative standard deviation of ~ 1.3 - 1.4 [134]. A similar process may be occurring in DBDs. Starting from an initially uncharged dielectric surface, the first filaments will deposit amounts of charge at different locations on the surface fitting a normal distribution [121,122]. The locations where charge is deposited will act as nucleation centers for succeeding filaments, because the local field strength is enhanced; the well-known 'memory effect' [51]. It is conceivable that locations with initially slightly larger amounts of 'memory charge' will lead to longer burning, or higher current filaments in subsequent discharge periods, leading to increased surface charge, while those locations at the lower end of the initial surface charge distribution will not accumulate charge as quickly over subsequent discharges. An increase in charge/pulse over two consecutive discharge periods has been observed in a DBD model calculation by Xu and Kushner [48]. Nonetheless, during steady-state operation, *i.e.* after many discharge periods, it could still be expected that all filaments will increase their local surface charge to some maximum value. This issue may be resolved simply by the fact that
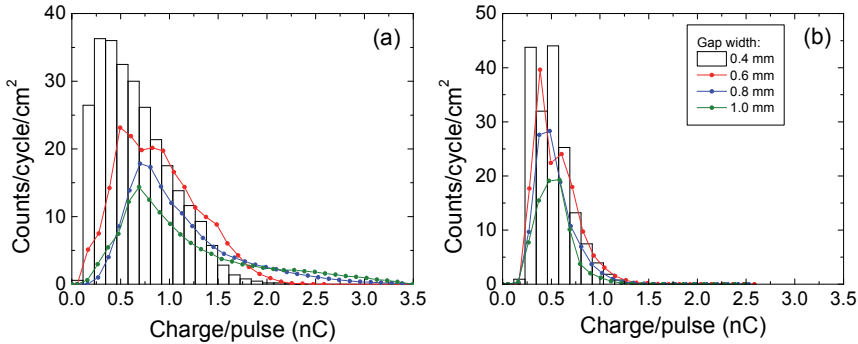
Figure 4.8: *Charge distribution for (a) positive current and (b) negative current in an asymmetric DBD in air with the secondary electrode covered by 0.6 mm alumina and variable gap widths between 0.4 - 1.0 mm. Driving voltage amplitude is 10 kV_{pp} for all configurations, leading to nearly equal conduction currents of ~ 30 mA/cm^2.*

the surface charge distribution is constantly developing as a function of time, due to interaction between the charges deposited by neighboring filaments in a discharge period. Bogaczyk *et al.* show that the pattern of free surface charges on the dielectric remains constant for no more than 10 - 12 consecutive voltage cycles in He/N_2 mixtures [135]. Similarly, Akishev *et al.* find that individual filaments in air re-ignite in the same location for up to 300 consecutive voltage cycles before significant 'relocation' of a filament occurs [117,121]. Stollenwerk *et al.* have observed collision processes between recurring filaments, leading to the annihilation of one of the filaments in succeeding voltage cycles [136]. A constantly changing surface charge distribution, *i.e.* locally accumulated charges have a limited lifetime, in combination with disproportionate growth for the locally greater accumulated charges, could then produce a log-normal distribution as observed here. Note that the moment of ignition of a filament within a discharge period may also be related to the surface charge distribution, as discussed at the beginning of this section, where the moment of ignition is also a determining factor in the peak current of that filament. The collective behavior of filaments leading to log-normal distributions may therefore be more complex than discussed here, though extensive modeling of this behavior is currently lacking in DBD literature.

4.3.3 Effect of gap width and dielectric thickness

The effect of gap width on the charge distribution of an alumina asymmetric DBD is depicted in Figure 4.8. In this figure, the plasma currents are ~ 30 mA/cm^2, independent of gap width. For the negative half-cycle there is little change in the distribution when increasing gap width from 0.4 to 1.0 mm, except that the contribution of APTD to the total plasma current increases. At 0.4 mm gap width, approximately 60% of the current can be accounted for by filamentary current pulses, while at 1.0 mm gap width this is only 25%. The positive half-cycle clearly shows a shift to lower charge/pulse as the gap width is decreased, from $<q_+>$ = (1.2 ± 0.1) nC to (0.7 ± 0.1) nC, while the higher gap widths of 0.8 and 1.0 mm have a long tail towards 3.5 nC. The effect of increasing average charge/pulse, $<q_+>$, with increasing gap width has been consistently observed by other authors in symmetric DBD configurations [124–128], but is here confirmed for the asymmetric configuration where the dielectric serves as the cathode. During the negative half-cycle, when the metal electrode is the cathode (emitter of electrons), this effect is clearly absent, as seen in Figure 4.8(b).

Increasing the dielectric thickness has the opposite effect of increasing gap width, as depicted in Figure 4.9. Increasing alumina thickness from 0.6 mm to 2.0 mm leads to a lowering of the average charge pulse, $<q_+>$, from (0.9 ± 0.1) nC to (0.8 ± 0.1) nC. The distributions also shrink on the vertical axis, as the plasma current at 8 kV$_{pp}$ decreases from 20 to just 2 mA/cm^2. Once again, the distributions of the negative half-cycle do not change significantly, except that for dielectric thicknesses between 1.0 - 2.0 mm all plasma current can be accounted for by filamentary current pulses, *i.e.* there is no APTD.

To determine the influence of dielectric material, charge distributions are also measured using quartz. Figure 4.10 depicts results for quartz thicknesses of 0.6, 0.9 and 1.1 mm and a gap width of 0.6 mm. The applied voltage was set to 9 kV$_{pp}$, instead of 8 kV$_{pp}$ in Figure 4.9, to compensate for the larger voltage drop over the dielectric. Plasma currents are significantly lower, however, at 2 - 6 mA/cm^2 for quartz thicknesses of 1.1 and 0.6 mm, respectively. As seen in Figure 4.10,
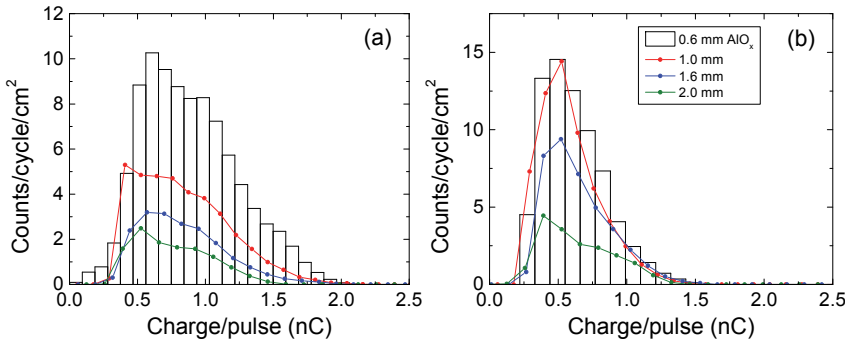
Figure 4.9: *Discharge distributions for (a) positive current and (b) negative current in an asymmetric DBD in air with a gap width of 0.6 mm and the secondary electrode covered by 0.6 to 2.0 mm alumina. The applied voltage amplitude is 8.0 kVpp.*
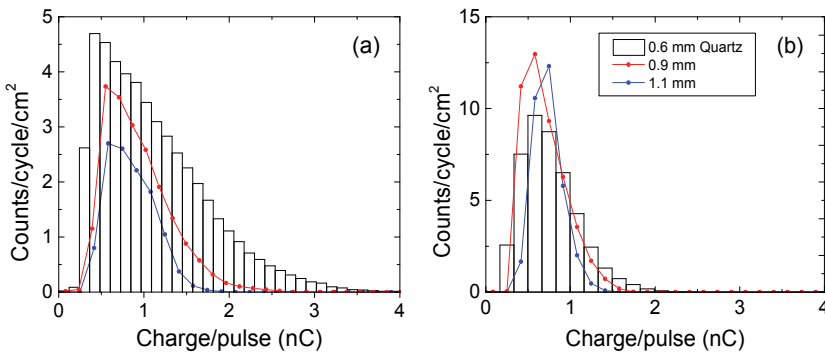
Figure 4.10: *Discharge distributions for (a) positive current and (b) negative current in an asymmetric DBD in air with a gap width of 0.6 mm and the secondary electrode covered by 0.6, 0.9 and 1.1 mm quartz. The applied voltage amplitude is 9.0 kV$_{pp}$.*

the positive half-cycle distributions for quartz show a larger change with dielectric thickness than alumina, which suggests the charge/pulse of filaments depends on the dielectric material. The negative half-cycle distributions remain similar to those for all other configurations, with $\langle q_- \rangle \approx 0.6$ nC. Little information is available in the literature for comparing $\langle q_- \rangle$ to $\langle q_+ \rangle$, though Gibalov *et al.* claim a ratio of 1:3 between $\langle q_- \rangle$ and $\langle q_+ \rangle$ for an asymmetric DBD with 1.35 mm gap width [124], similar to the results presented here.

4.3.4 Symmetric DBDs

For the symmetric case, no distinction can be made between positive or negative current, as in both directions the dielectric material serves as the cathode. We therefore compare charge distributions for symmetric configurations with the positive current distributions of the asymmetric configurations, where the dielectric also serves as cathode. If both electrodes are covered by dielectric material, a shift to lower charge/pulse occurs, as seen in Figures 4.11 and 4.12 for alumina and quartz, respectively. The average charge/pulse for 2 x 0.3 mm alumina, $<q> = (0.4 \pm 0.1)$ nC, as opposed to $<q_+> = (0.9 \pm 0.1)$ nC for 1 x 0.6 mm alumina. For quartz the difference is comparable, with $<q> = (0.4 \pm 0.1)$ nC for 2 x 0.5 mm quartz, compared to $<q_+> = (0.9 \pm 0.1)$ for 1 x 1.1 mm quartz. The values for $<q>$ are in good agreement with those found by Jidenko *et al.* for alumina [128] and Drimal *et al.* for quartz [126], though their results are closer to single-filament distributions at low applied voltage. The current densities for symmetric and asymmetric configurations are comparable for equal total dielectric thickness, with 30 mA/cm^2 for alumina and 2.0 mA/cm^2 for quartz, respectively. Covering both electrodes with a dielectric leads to ~ 2 times larger number density of filaments with ~ 2 times lower charge/pulse. This was not verified for a wide range of geometries, however, but similar observations were made in [137]. The fact that the charge/pulse is reduced for the symmetric configuration can be explained by the charge removed from one dielectric now being deposited on the opposite dielectric, instead of simply being removed from the gap via a conducting electrode. Any amount of charge conductively transferred from one dielectric to the other will lead to a doubled rate of reduction of the burning voltage across a filament, U_b, compared to the asymmetric configuration. This leads to extinction of the filament at only half the transferred charge.

In the case of quartz, the columns of the spectra in Figure 4.12 have been refined to 0.01 nC, to better show the structure. For the symmetric configuration, the spectra show up to four separate peaks with increasing applied voltage, equal to the average counts/cycle at each applied voltage. This indicates that the location and charge transferred per half-cycle of the filaments is more stable than for other configurations, leading to distinct peaks in the spectra. Similar to the
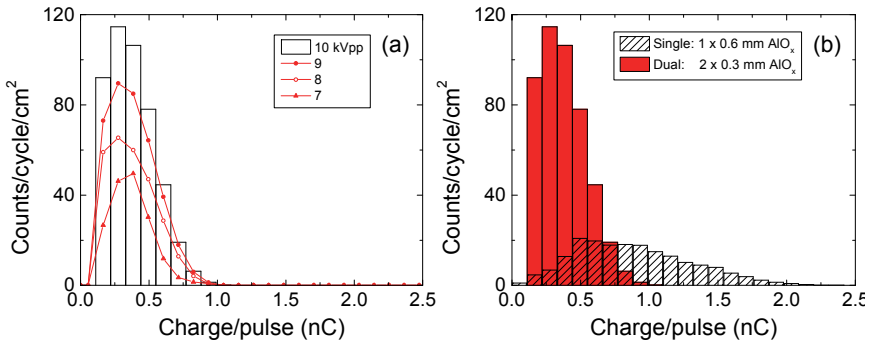
Figure 4.11: *(a) Discharge distributions for a symmetric DBD in air with both electrodes covered by 0.3 mm alumina and a 0.6 mm air gap at different voltage amplitudes. (b) Comparison of the same symmetric DBD with an asymmetric DBD of the same dimensions at 10 kV$_{pp}$.*
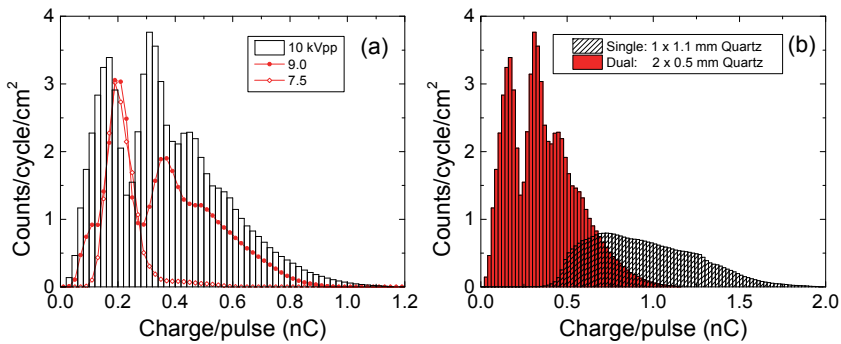
Figure 4.12: *(a) Discharge distributions for a symmetric DBD in air with both electrodes covered by 0.5 mm quartz and a 0.3 mm discharge gap at different voltage amplitudes. (b) Comparison of the same symmetric DBD with an asymmetric DBD with slightly thicker quartz and a gap width of 0.4 mm at 10 kV$_{pp}$. Note that the width of each column in these plots is only 0.01 nC, as opposed to the standard 0.1 nC.*

time-stepped measurements in Figure 4.7, it is argued that individual filaments recurring in roughly the same location have a normal distribution, while the combination of all filaments have a log-normal distribution.

4.3.5 Average charge/pulse and its relation to burning voltage

In this section, we summarize the charge/pulse measurements, show the variation in filament density, discuss the differences between dielectric materials and show how the burning voltage is affected by changes in the DBD configuration.

The results for asymmetric DBDs, with only the secondary electrode covered by a dielectric, are summarized in Figure 4.13. In order to plot the weighted average charge/pulse as a function of gap width, d_{gap}, dielectric thickness, d_{diel}, and relative permittivity, ε_r, we use the ratio between DBD cell capacitance C_{cell} and dielectric capacitance C_{diel}:

$$1 - C_{cell}/C_{diel} \approx \frac{1}{1 + d_{diel}/\varepsilon_r d_{gap}}, \tag{4.1}$$

which assumes that the gap and dielectric capacitances have an equal area and both can be described as ideal parallel plate capacitors. Equation (4.1) shows that if the capacitance of the dielectric is equal to the gap capacitance, $1 - C_{cell}/C_{diel} = 0.5$, and if the dielectric capacitance is far greater than the gap capacitance $1 - C_{cell}/C_{diel} \approx 1$. As seen in Figure 4.13(a), the weighted average charge/pulse during the positive half-cycle, is roughly linear with $1 - C_{cell}/C_{diel}$ for both quartz and alumina, though $<q_+>$ for quartz is ~ 0.3 nC higher at every point. For the negative half-cycle, depicted in Figure 4.13(b), $<q_->$ is roughly independent of material with a slight linear increase as a function of $1 - C_{cell}/C_{diel}$. As shown in the previous section, the average charge/pulse for symmetric DBD configurations, with equivalent capacitances, will be half that of the asymmetric configurations. Figure 4.14 depicts the filament density during the positive half-cycle, N^+, at a voltage amplitude of 10 kV$_{pp}$ for the same configurations as Figure 4.13. As seen in Figure 4.14, filament density increases significantly with lower dielectric thickness (higher C_{diel}), while increasing gap width (lower C_{gap}) leads to a small decrease in filament density. This data shows that altering the DBD configuration has a larger effect on filament density than on the individual filaments themselves.
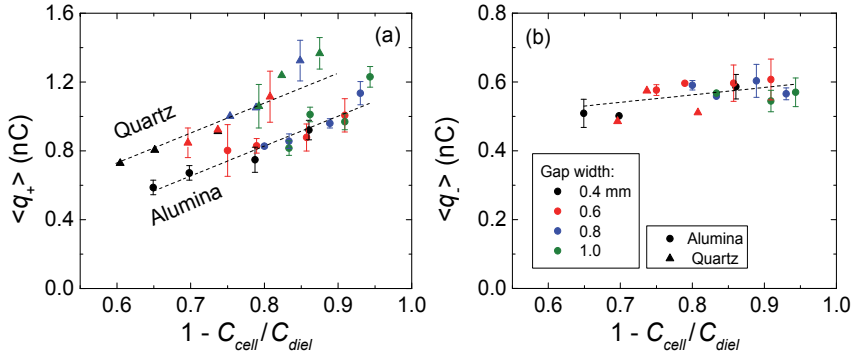
Figure 4.13: *Weighted average charge/pulse for (a) positive current and (b) negative current for all asymmetric DBD configurations used in this work. For a given gap width, the dielectric thicknesses for the data points from left to right are 2.0, 1.6, 1.0 and 0.6 mm for alumina and 1.1, 0.9 and 0.6 mm for quartz, respectively. The vertical bars indicate the range of the average charge/pulse for different applied voltage amplitudes, if measured. The dashed lines are guides to the eye.*
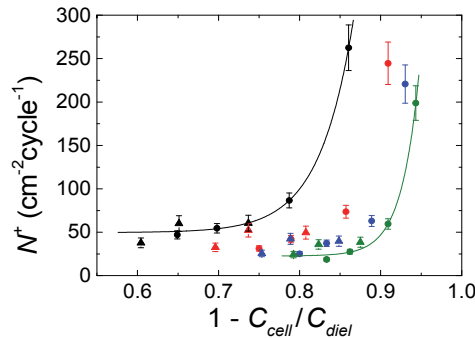
Figure 4.14: *Filament density at applied voltages of 10 kV_{pp} for the positive half-cycle for all asymmetric DBD configurations used in this work, including quartz and alumina dielectrics. Colour coding is the same as in Figure 4.13. The lines are guides to the eye.*

Previous work by Gibalov and Drimal *et al.* for symmetric DBDs shows the same values for the average charge/pulse as the data in Figure 4.13(a), to within a factor of two [118,124,126,127]. In [118,124] they show that the average charge/pulse increases as a function of specific dielectric capacitance, defined as ε_r/d_{diel}, by 0.9 nCmm for a gap width of 1.35 mm. However, this rate is determined for materials with relative permittivities ε_r between 7.5 and 1000 and is, consequently, based on a much wider range of specific dielectric capacitances than measured here. Gibalov and Drimal *et al.* conclude

from their measurements that there is little dependence on dielectric material beyond its relative permittivity, *i.e.* beyond its basic electrical properties. Though not pictured in Figure 4.13(a), the rate of increase with ε_r/d_{diel} measured here is 0.08 nCmm for quartz and 0.02 nCmm for alumina, both lower than determined in [118,124] and with a significant difference between the materials. Clearly, there is a difference between filament dynamics beyond the electrical capacitance of the dielectric layer. To determine the influence of surface temperature, an IR thermometer was used on the dielectrics after 6 minutes of discharging. For both alumina and quartz, surface temperature is 40 - 50 °C, irrespective of material thickness and gap width, ruling out thermal properties as the cause of the differences in charge/pulse. The influence of surface roughness, the secondary electron emission coefficient γ, and the energy at which surface charges can be trapped may both play a role in the dynamics of the filamentary discharge [138]. For example, quartz has an electron affinity $\chi = 1.3$ eV, versus $\chi = 2.5$ eV for alumina [139], which implies charges are trapped less effectively in quartz than alumina.

The linear behaviour of $<q_+>$ as a function of $1 - C_{cell}/C_{diel}$ in Figure 4.13(a) cannot be easily accounted for, though $1 - C_{cell}/C_{diel}$ is equal to the proportion of gap voltage to external voltage, U_{gap}/V, if the effect of dielectric surface charging is neglected. The gap voltage U_{gap} will, however, be significantly affected by charges on the dielectric left behind during discharges in the previous half-cycle. The resulting gap voltage is the burning voltage U_b. To investigate this further, the average burning voltages $<U_b>$ during the filamentary discharges are obtained for various DBD configurations, using the method presented in Chapter 2. The results of several runs, where both $<U_b>$ and $<q^+>$ are measured simultaneously for various applied voltage amplitudes, are depicted in Figure 4.15(a). This data shows that the burning voltage $<U_b>$ is relatively independent of average charge/pulse $<q^+>$. The same values for $<U_b>$ are plotted as a function of the root-mean-square gap voltage $U_{gap,RMS}$ in Figure 4.15(b). The latter is a measure of the voltage over time within the gap, in the absence of surface charging. Though $U_{gap,RMS}$ varies from 1.5 - 3.6 kV for the applied voltages used with these configurations, it has little effect on $<U_b>$. It seems, therefore, that DBDs tend toward an equilibrium where $<U_b>$
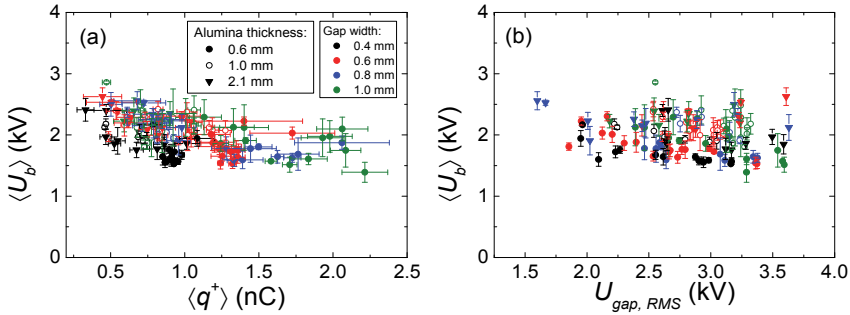
Figure 4.15: *Average burning voltage $<U_b>$ as a function of (a) average charge/pulse $<q^+>$ and (b) root-mean-square gap voltage $U_{gap,RMS}$ during the positive half-cycle for 12 DBD configurations using alumina. Note that these measurements were performed at a different time from those in Figure 4.13, with different alumina samples and relative humidity.*

is nearly constant, despite variable gap widths, dielectric thicknesses and external voltages.

The burning voltage $<U_b>$ is not directly related to the breakdown voltage V_B as predicted by the Paschen curve. Increasing the gap width from 0.4 mm to 1.0 mm leads to an increase of the breakdown voltage V_B in air from 3.5 kV to 7.4 kV; both larger than $<U_b>$ [140]. The effect of the secondary electron emission coefficient γ, with values on the order of a few percent, lowers V_B by no more than ~ 0.1 kV [78]. The origin of the deviation between $<U_b>$ and V_B can be sought in (*i*) the presence of net space charge near anode or cathode in a DBD in steady-state operation [141] and (*ii*) the highly non-uniform electric fields resulting from residual charges on the dielectric [142]. Both (*i*) and (*ii*) are components not included in the derivation of Paschen's law [143]. It is worth noting that in computational models of single filaments, initial gap voltages *above* the breakdown voltage V_B are commonly used [33,34,37,142,144], in clear contradiction to the lower burning voltages for multi-filament discharges found here. In *e.g.* the models of Yurgelenas *et al*, a DC gap voltage of 5 kV is used to generate a weak Townsend discharge during the so-called pre-breakdown phase [34,37,38,142]. This Townsend discharge leads to a positive space-charge region near the anode, which subsequently develops into a cathode-directed filament. In a DBD in steady-state operation there will already be ions in the gap, left behind during previous discharges [117,145]. As shown by Kozlov *et al*, the pre-

existing negative ions in air discharges lead to filament propagation at lower fields due to additional electrons supplied by detachment processes [35]. We will not attempt to provide a quantitative explanation for the observed values of the burning voltage U_b here, but will instead focus on the fact that U_b is a constant throughout a discharge half-cycle. The relations between average burning voltage $<U_b>$, external voltage V, average charge/pulse $<q>$, filament number density N^+ and the surface charge state of the dielectric are discussed in Chapter 5.

4.4. Conclusions

Studying the transferred charge/pulse for a large number of filaments we find that the shape of the charge distributions does not change significantly with applied voltage amplitude. Small changes in the transferred charge/pulse can be achieved by varying gap width, dielectric thickness or dielectric material, but for a given external voltage, the largest changes are in the filament density. Similarly, burning voltage was found to be nearly independent of DBD configuration and external voltage. Similar to the conclusions drawn in Chapter 2 and Chapter 3, control over the discharge is mainly limited to changing the density of filaments.

In more detail, the findings in this chapter are:

(1) For a set DBD configuration, increasing the applied voltage leads to an increase in current through an increase in the number of filaments, *not* through an increase in the charge transferred by individual filaments. The filament number density increases nearly linearly with plasma current, with only a ~ 15% decrease in the average charge/filament. Though this has been observed previously [121,126–128], it is here shown to continue toward higher plasma currents. Increasing gap width or reducing dielectric thickness leads to only a limited increase in the average charge/pulse and the width of the distribution; by no more than a factor of 2 for the configurations studied here. The average charge/pulse is

shown to roughly scale with $1 - C_{cell}/C_{diel}$. Changing from an asymmetric to an electrically equivalent symmetric DBD configuration can lower the charge distribution by a factor of 2, including its standard deviation.

(2) The charge/filament distributions fit very well to a log-normal distribution, with multiplicative standard deviation $s^* \approx (1.4 \pm 0.4)$, where the lower limit of the distributions can be found at $<q_{+/-}>/2s^*$ and the higher limit at $<q_{+/-}> \cdot 2s^*$. Previous studies found normal distributions for the charge/filament, which have multiplicative standard deviation $s^* = 1$, because only single filaments were measured through the choice of geometry [121,122], or because of low filament number density at low applied voltages [124–128]. The log-normal distribution can arise from the development of memory charge on the surface of the dielectric, where regions with above-average charge tend to accumulate more charge over several discharge cycles than regions with less charge.

(3) Contrary to the conclusions of Gibalov *et al.* in [118,124], the effect of dielectric material on the filament dynamics is not determined solely by the relative permittivity ε_r. The rate of increase of the average charge/pulse with specific dielectric capacitance, ε_r/d_{diel}, is 0.08 nCmm for quartz and 0.02 nCmm for alumina. Moreover, quartz leads to ~ 0.3 nC higher average charge/pulse as a function of $1 - C_{cell}/C_{diel}$ than alumina. These differences between alumina and quartz may originate from surface roughness, differences in secondary electron emission and the energies at which memory charges can be trapped in the material.

(4) In steady-state operation, the average burning voltage $<U_b>$ varies little with applied voltage amplitude or DBD configuration. It seems that DBDs tend toward an equilibrium where $<U_b>$ is constant by changing the dielectric surface charge distribution (memory charge) and, hence, the voltage in the gap. The average burning voltage $<U_b>$ is also significantly lower than that predicted by Paschen's law, which may be due to (*i*) the presence of net (space-)charge near anode or cathode in a DBD in steady-state operation and (*ii*) the highly non-uniform electric fields resulting from

residual charges on the dielectric. Existing models of single filaments assume the burning voltage is greater than that predicted by Paschen's law, in clear contradiction to the experimental results obtained here.

Appendix to Chapter 4

This appendix describes the DBD current measurements used for calibration of the PHA data (Section A4.1), a detailed description of the PHA circuit (Section A4.2), the calibration procedure for both axes of a PHA spectrum (Section A4.3) and the influence of DBD electrode size on the PHA spectra (Section A4.4).

A4.1 Current measurements

Time-averaged currents per half-cycle are measured using the setup depicted in Figure A4.1, where diodes and a switch ensure current is only measured when it is positive or negative. The relative difference between the resulting average currents in the positive and negative directions, $<i(t)>_+$ and $<i(t)>_-$, are always lower than 5% prior to plasma ignition and roughly 3% when filaments are present in the gap, which are considered to be the maximum measurement errors.

The plasma current $i_{plasma}(t)$ can be calculated using [72]:

$$i_{plasma}(t) = \frac{1}{1 - C_{cell}/C_{diel}}\left[i(t) - C_{cell}\frac{dV(t)}{dt}\right]. \qquad (A4.1)$$

When measuring only positive or negative current, $<i(t)>_{+/-}$, Equation (A4.1) can be rewritten to:
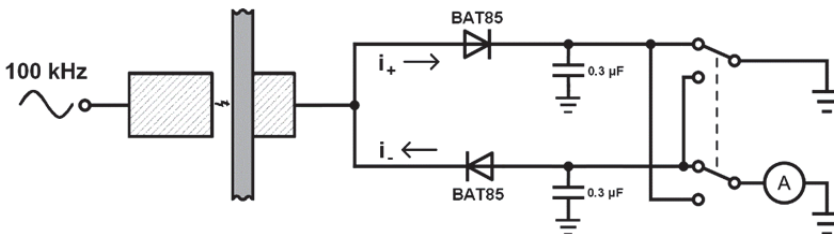
Figure A4.1: *Schematic of the current measurement setup. The average current through the DBD is measured for either positive or negative current using diodes.*
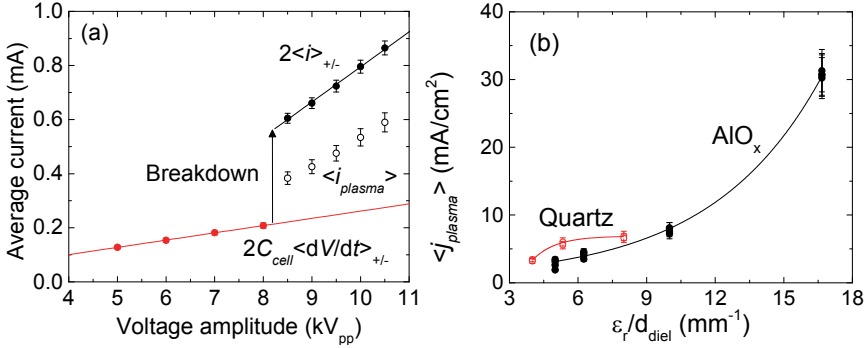
Figure A4.2: *(a) Average current as a function of peak-to-peak voltage amplitude for a 0.8 mm air gap with 1.0 mm alumina as dielectric and an electrode area of 7 mm². (b) The average current densities $<j_{plasma}>$ at maximum applied voltage of 10 kV$_{pp}$ as a function of ε_r/d_{diel}, for both alumina and quartz. The effect of gap width on the plasma current is minimal.*

$$\frac{1}{2}\left\langle i_{plasma} \right\rangle = \frac{1}{1 - C_{cell}/C_{diel}}\left[\left\langle i(t) \right\rangle_{+/-} - C_{cell}\left\langle \frac{dV(t)}{dt} \right\rangle_{+/-} \right]. \quad (A4.2)$$

Here, $<i_{plasma}>$ is the average plasma current over time, with the factor 1/2 due to only positive or negative average current, $<i(t)>_{+/-}$, being measured. The term $C_{cell}<dV(t)/dt>_{+/-}$ is the capacitive component of the average current in the positive or negative direction. For equal sized electrodes, the prefactor in Equation (A3.2) can be simplified to:

$$\frac{1}{1 - C_{cell}/C_{diel}} = 1 + \frac{d_{diel}}{\varepsilon_r d_{gap}}, \quad (A4.3)$$

where d_{diel} and d_{gap} are the thickness of the dielectric and the width of the air gap, respectively, and ε_r is the relative permittivity of the dielectric material. Equations (A4.2) and (A4.3) can be used to determine $<i_{plasma}>$ from average current measurements, $<i(t)>_{+/-}$ as a function of voltage amplitude. An example of this is shown in Figure A4.2(a), where $C_{cell}<dV(t)/dt>_{+/-}$ is extrapolated to voltages above breakdown, which is then subtracted from the average current $<i(t)>_{+/-}$ above breakdown, while the remainder is corrected by the factor in

Equation (A4.3) to obtain $<i_{plasma}>$. Including the uncertainties in d_{diel}, d_{gap} and ε_r, the error in $<i_{plasma}>$ is around 10%.

Depending on the choice of dielectric and gap width, time-averaged plasma current densities up to 32 mA/cm^2 are achieved in the DBD. Figure A4.2(b) shows the current density $<j_{plasma}>$ for electrode areas of 7 mm^2 at the maximum applied voltage amplitude of 10 kV$_{pp}$ for all asymmetric DBD configurations used in this work. Gap widths between 0.4 and 1.0 mm are used, but current density is roughly independent of gap width within the error of the measurement.

A4.2 PHA circuit

Following is a step-by-step description of the components of the PHA circuit, depicted schematically in Figure A4.3.

DBD
The DBD, integrated in the PHA circuit, has one electrode attached to the 100 kHz sinusoidal driving voltage, while the other electrode is linked to the PHA circuit. In this case, the secondary electrode is not grounded as would be the case during normal operation of a DBD. Instead of grounding, the voltage on the secondary electrode is corrected by the **100 kHz compensation** circuit. This circuit corrects any capacitive coupling between the primary electrode and the secondary electrode by subtracting the capacitively induced voltage at the secondary electrode. However, during discharging, the presence of filaments provides current pulses to a 750 pF capacitor which charges up to ≤ 3 V. These low voltages are the only deviations from grounded voltage that the secondary electrode is subject to. Also indicated in the diagram are the capacitances to ground of the electrodes, 60 pF and 9 pF, respectively, which are high and low enough, respectively, not to affect the measurements. Depending on the size of the electrodes, the dielectric material, or the width of the air gap, the electrode-to-electrode capacitance of the DBD itself is between 0.1 - 0.7 pF.

(1) Pulse height pathway

The filamentary current pulses rapidly charge the 750 pF capacitance by several volts, which discharges over 400 Ω with a deacy time of

~ 0.3 μs. The 400 Ω resistivity consists of 2 parallel placed resistors indicated as '1k5' and '500' in the diagram of Figure A4.3. The decay time of ~ 0.3 μs is much longer than the duration of a filament (~ 20 - 40 ns), so that the peak voltage on the 750 pF capacitor is an accurate measure of the total conductively transferred charge of a single filament across the air gap of the DBD, via the relation $Q = CV$. The time-dependent voltage on this part of the circuit is measured via the 400 Ω resistor, which is used as a variable gain, and passes through the **Shaper**. The Shaper modifies the positive or negative voltage signal on the 750 pF - 400 Ω RC components to 50 ns block-like pulses with a height corresponding to the peak voltage on the 750 pF capacitor. It is the height of these block-like pulses which are eventually accumulated in the PHA spectra. Note that the actual height of these block-like pulses depends on the variable gain setting on the 400 Ω resistor, which needs to be taken into account when calibrating the spectra. The Shaper is followed by a switch, so that only positive or negative pulses, from either the positive or negative voltage half-cycles, are selected for analysis.

Note that it is possible for multiple filamentary current pulses to occur within the ~ 0.3 μs relaxation time of the 750 pF measurement capacitance. This is corrected for by the Shaper, as is schematically depicted in Figure A4.4. Since the block-like pulses after the Shaper have a duration of 50 ns, filamentary current pulses separated by less than 50 ns may lead to errors in the PHA spectrum. This is discussed further in Section A4.4.

(2) Pulse rise pathway

The current signal from the discharge leads to current through the 750 pF capacitor and a corresponding slope of the voltage across this capacitor. The fast rising slope, or leading edge, of this voltage, which occurs whenever there is a filamentary current pulse, is adjusted by the **Differentiator**. This component differentiates the current signal and creates a 5 ns voltage pulse with a height corresponding to the

Figure A4.3: *Schematic of the Pulse Height Analyzer (PHA) circuit for DBDs, explained in detail in the text.*

rising slope of the voltage on the 750 pF capacitor. This signal is then measured via a 100 Ω resistor set up as a variable gain and passes through an amplifier (**Ampl.**). The gain and amplifier settings are used to optimize the signal-handling of these 5 ns pulses. Here also, a switch is used to select between positive and negative pulses for further analysis. The pulse rise pathway serves to count the number of filamentary current pulses occurring in the DBD and provides a gating signal for the PHA, which is discussed further in the section on discrimination**.**

(t) Time pathway

The time pathway is indicated as "t" in Figure A4.3. Here, the sinusoidal driving voltage is used as an indicator of time and is fed into the **Cross-over detection**, where the zero-crossing of the voltage is detected twice per full cycle. Either positive or negative cross-overs are selected using a switch, sending a single 5 ns pulse per full cycle to the **Delay** and **Measurement period** segments, which together provide an on/off signal of 4 μs duration to the rest of the circuit. An additional segment, termed **Subdivisions**, is used to further shrink the 4 μs measurement window into a 120 ns measurement window. Each full cycle this 120 ns measurement window is shifted forward in 166 ns increments to cover the entire 4 μs window in 24 full cycles. By selectively triggering only once every 24 full cycles, the same 120 ns measurement window is used in the detection of filaments, while triggering each full cycle, the entire 4 μs window is scanned by the detection circuit. See Figure A4.5 for an overview of delay, measurement period and subdivisions.

Discrimination

The 50 ns pulse height and 5 ns pulse rise signals pass through two separate discriminators, **Discr. I** and **Discr. II**. These two components are both on/off gated by the 4 μs measurement window from the time pathway. Discr. I can be adjusted to admit only pulse height signals with a certain minimum height. This setting is used to prevent noise in the signal from registering on the left-hand-side of the spectrum and is never set too high, or a strong cut-off becomes apparent in the spectrum. Discr. II can be set to admit only current pulses with a sufficiently high rising slope. Though no pulses are admitted to the
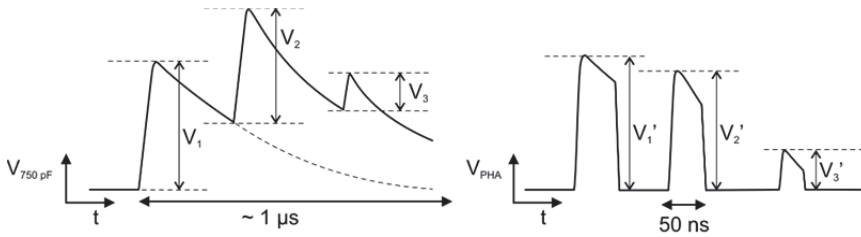
Figure A4.4: Schematic representation of the voltage on the 750 pF capacitor if multiple filamentary current pulses occur within the discharge time of the capacitor (left) and the block-like pulse height peaks to the PHA spectrum, after correction by the Shaper Clip component (right).
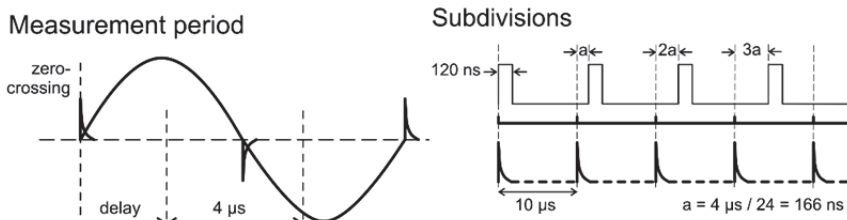
Figure A4.5: *Schematic overview of the 4 µs measurement window with zero-crossing pulses indicated on the 100 kHz AC driving voltage (left) and the 24 x 120 ns subdivisions, which are delayed every full cycle by increments of 166 ns to cover the entire 4 µs measurement window (right). Note that delay with respect to the zero-crossing pulses is not indicated in the right-hand figure, but is active here as well.*

PHA spectrum if set too high (> 300 MV/s on 750 pF), decreasing its setting to much lower values was found to have little effect on the PHA. The output from Discr. II leads to **Counter *N1***, which provides the number of fast changes in slope on the 750 pF capacitor over the full 4 µs measurement window. The two discriminators are followed by **Coin. I**, or Coincidizer I, which passes on the 5 ns pulse rise signal only if its initial slope is coincident with the pulse height signal. **Counter *N2*** provides a reference value for the number of counts at this stage and always has between 99% to 95% the value of Counter *N1*. **Coin. II**, or Coincidizer II only passes on the pulse rise signal during the 120 ns measurement windows from the **subdivisions** component. The number of counts at this stage is registered by **Counter *N3***, which has roughly 1/33 the value of *N2*, because the measurement duration is now only 120 ns instead of 4 µs, see Figure A4.3. For all counters *N1*, *N2* and *N3*, values are obtained separately

for positive and negative half-cycles and expressed in units of counts/cycle/cm^2. The value of *N1* provides the most reliable measure of filamentary current pulses in the DBD and is therefore used throughout this work as a reference value, termed $N^{+/-}_{measured}$ from here on.

ADC

After discrimination and coincidation, the 5 ns pulse rise signal is used to trigger the **Gate**, which passes the 50 ns pulse height signals to an analog-to-digital converter (**ADC**). The ADC has a resolution of 1/1000 the maximum pulse height. In the data analysis this resolution is converted to 0.1 nC for clarity and consistency between different measurements. The ADC used here has a down-time of up to ~ 3 μs between receiving the 50 ns pulse height signals, which therefore significantly reduces the total number of counts incorporated into a spectrum. To obtain a statistically significant sample, each PHA spectrum is collected in 32 s of total measurement time, which at a driving voltage frequency of 100 kHz corresponds to $3.2 \cdot 10^6$ discharge cycles. When measuring spectra as a function of time, collection of data occurs only once every 24 full cycles (see the section on time pathway) and longer measurement times are used.

A4.3 Calibration of spectra

The values on the horizontal axis of the spectra are determined by gain and scaling settings in the PHA circuit. This axis was calibrated by providing a single current pulse to the 750 pF measurement capacitor. Since the peak voltage on the 750 pF capacitor, V_{peak}, can be measured, the location of the resulting single peak on the PHA spectrum can be converted to charge/pulse via:

$$Q_{peak} = \left(1 + \frac{d_{diel}}{\varepsilon_r d_{gap}}\right) C_{750\,pF} V_{peak}\,, \qquad (A4.4)$$

where the prefactor, described by Equation (A4.3), needs to be included in the calibration for each DBD configuration, to convert the

charge measured in the external circuit to the transferred charge in the gap [72]. A systematic error on the horizontal axis of 0.15 nC is estimated, based on repeated calibration measurements. With the horizontal charge/pulse axis known, the weighted average charge/pulse can be determined from a PHA spectrum using:

$$\left\langle q_{+/-} \right\rangle = \frac{\sum q_i n_i}{\sum n_i} , \qquad (A4.5)$$

where $<q_{+/-}>$ is the weighted average charge/pulse for positive or negative voltage half-cycles, q_i and n_i are the charge/pulse and number of counts on the ith channel, respectively. For ease of comparison, each spectrum is interpolated in steps of 0.1 nC, instead of the 1000 channels of the PHA component.

From the average charge/pulse, $<q_{+/-}>$, the expected average number of counts/cycle during either the positive or negative voltage half-cycles can be determined from the relation:

$$N_{\text{expected}}^{+/-} = \frac{\left\langle i_{plasma} \right\rangle}{\left\langle q_{+/-} \right\rangle} \frac{1}{2fA} , \qquad (A4.6)$$

Where $N_{\exp ected}^{+/-}$ is the average number of counts per cycle per cm^2 of electrode area, $<q_{+/-}>$ the average charge/pulse in coulomb, $<i_{plasma}>$ is the average plasma current in amperes, which is the same for positive and negative half-cycles, f is the frequency of the driving voltage and A the surface area of the electrodes in cm^2.

The values of the expected average number of counts per cycle $N_{\exp ected}^{+/-}$, calculated from Equation (A4.6) can be compared to those determined directly in the PHA circuit for either positive or negative half-cycles, $N_{measured}^{+/-}$, as discussed in the section on Discrimination. Comparing these two numbers provides a measure of the number of pulses missed by the PHA circuit. The number of counts $N_{measured}^{+/-}$ should not exceed $N_{expected}^{+/-}$, to within the margin of error. It is possible, however, that $N_{expected}^{+/-}$ is significantly larger than $N_{measured}^{+/-}$. Calibration
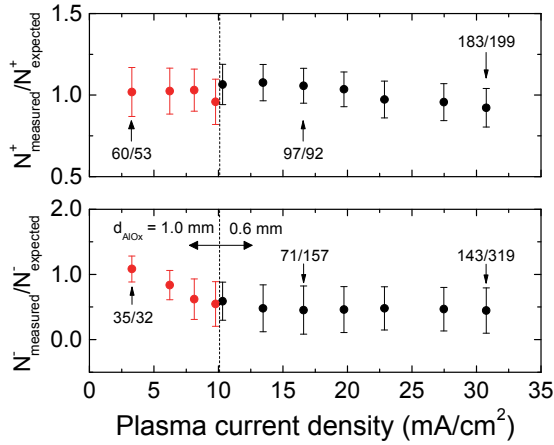
Figure A4.6: *The ratios $N^{+/-}_{measured} \big/ N^{+/-}_{expected}$ for positive and negative half-cycles. Indicated in the figure are selected values for $N^{+/-}_{measured} \big/ N^{+/-}_{expected}$. Gap width is 0.6 mm and electrode diameters are 3.0 mm, while for both alumina thicknesses the applied voltage amplitudes are between 7 and 10 kV$_{pp}$.*

of the vertical axis is achieved by ensuring that the sum of all 0.1 nC wide columns in a spectrum add up to the average number of counts per cycle per cm^2. Whether $N^{+/-}_{expected}$ or $N^{+/-}_{measured}$ is used as the average number of counts per cycle per cm^2 is discussed in the next section.

Measured versus expected counts in the PHA circuit
By comparing the number of counts calculated from Equation (A4.6), $N^{+/-}_{expected}$, with the number of counts detected directly in the PHA circuit, $N^{+/-}_{measured}$, the detection capabilities of the PHA circuit can be investigated. The ratios between the two values $N^{+/-}_{measured} / N^{+/-}_{expected}$ $N^{+/-}_{measured} / N^{+/-}_{expected}$ are plotted in Figure A4.6 for a representative set of measurements, involving electrode diameters of 3.0 mm, an air gap of 0.6 mm and alumina thicknesses of 0.6 and 1.0 mm. As can be seen in the top panel of Figure A4.6, the ratio $N^{+/-}_{measured} / N^{+/-}_{expected}$ remains approximately ~ 1 within the measurement error for all plasma current densities, indicating that minimal current pulses are missed by the PHA circuit.

Murata *et al.* have shown that a filamentary discharge can trigger other filaments in the vicinity, leading to chains of overlapping
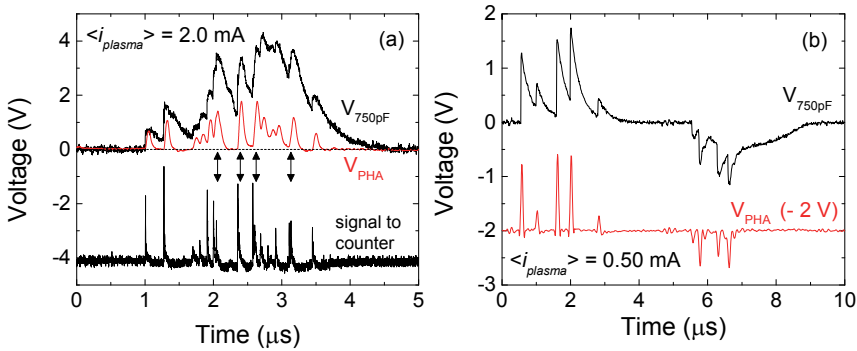
Figure A4.7: (a) Single-shot measurement of $V_{750\,pF}$, V_{PHA} and the signal to the counter N1 during the positive voltage half-cycle for a DBD with high filament number density. (b) Single-shot measurement of $V_{750\,pF}$ and V_{PHA} for a DBD at low filament number density for both voltage half-cycles.

current pulses within the space of about 1 cm^2, complicating charge/filament measurements [146]. Both Gibalov *et al.* and Jidenko *et al.* observe this effect using electrode areas of ~ 3 cm^2 [124,125,128]. To investigate this, single-shot measurements of the voltage on the 750 pF capacitor, $V_{750\,pF}$, the voltage to the PHA, V_{PHA}, and the signal to the counter (pulse rise pathway) are obtained at high plasma currents. Figure A4.7(a) shows an example of these voltages over time, where 17 filamentary current pulses occur within one positive voltage half-cycle, with 1 to 1 gain between $V_{750\,pF}$ and V_{PHA}. Comparing the signal to the counter with V_{PHA}, four cases can be identified where two filaments in rapid succession lead to a single 50 ns pulse height signal. The average time between two consecutive current pulses is ~ 30 ns, determined from many single-shot measurements. For the conditions used in Figure A4.7(a), ~ 200 counts/cycle/cm^2 occur during the positive half-cycle. For an electrode diameter of 3.0 mm, this translates to ~ 14 counts within the 4 μs measurement window, or an average time between pulses of 4 μs / 14 = 300 ns. If filaments occur randomly in time, overlap to within 30 ns will occur in 30 ns / 300 ns = 10% of cases. The frequency of overlapping current pulses observed in our measurements is closer to 20% at high plasma current densities, supporting the observation of Murata *et al.* The effect of this overlap on the charge distributions is discussed in greater detail in the section on applied voltage amplitude in the main text. As can be seen in Figure A4.7(b), overlapping current pulses are absent at lower plasma currents. To correct for

missed counts in the positive half-cycles, the expected number of counts, $N^+_{expected}$, is used to scale the charge distributions for the remainder of this work.

In the bottom panel of Figure A4.6, the ratio $N^{+/-}_{measured} / N^{+/-}_{expected}$ shows lower values than those seen for positive current. For the lowest plasma current it is still ~ 1, but decreases to ~ 0.5 for higher plasma currents. The reason for this is revealed when looking at the voltage over time on the 750 pF measurement capacitance, V_{PHA}, depicted in Figure A4.7(b). In this figure it can be seen that a continuous voltage envelope is present, without an exponential decay. This implies that there is continuous current from the DBD which lasts for several microseconds. For negative half-cycles, the electrons are emitted from the brass primary electrode (conductive cathode), which can lead to different discharge behavior compared to when the dielectric material serves as electron emitter (dielectric cathode) [113,123]. As can be easily determined from the ratio $N^{+/-}_{measured} / N^{+/-}_{expected}$, more than half the total plasma current can be carried by these continuous discharges. This discharge is identified as an Atmospheric Pressure Townsend Discharge, or APTD [66], discussed further in Chapter 5. In any case, this part of the discharge is not detected by the PHA circuit and will not show up in the measured charge distributions or be counted towards $N^-_{measured}$. This can be seen in Figure A4.7(b), where only the short duration current pulses in $V_{750\,pF}$ are converted to V_{PHA}. Contrary to the positive half-cycle, we can assume that the charge distributions obtained from the negative half-cycle are not representative of the entire half-cycle and that, consequently, missed counts should not be corrected for by using Equation (A4.6). For the remainder of this work, the vertical axis of negative half-cycles is scaled using $N^-_{measured}$ instead of $N^-_{expected}$.

A4.4 Electrode size

The ability to discern individual current pulses in the PHA circuit places a limit on the surface area of the electrodes, since for larger
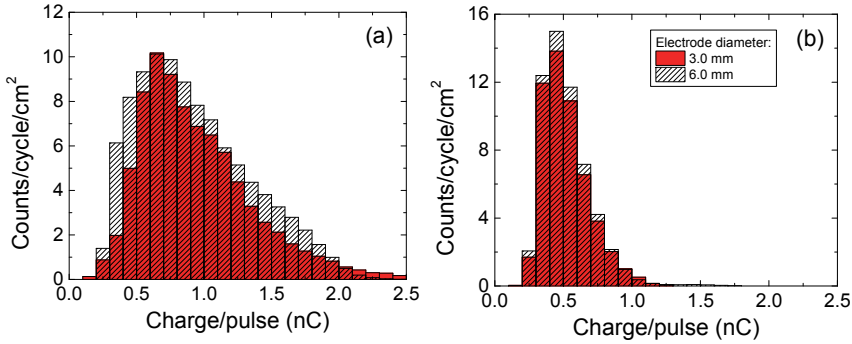
Figure A4.8: *Charge distribution for (a) positive current and (b) negative current in an asymmetric DBD in air with a gap width of 0.6 mm and a secondary electrode covered by 0.6 mm alumina for two different electrode diameters at an applied voltage amplitude of 8 kV$_{pp}$.*

electrodes the odds of multiple filaments occurring in rapid succession increases. The electrodes should not be so small, however, that the charge distributions hold no similarity to large-area DBDs. To investigate this, spectra are obtained from a DBD with cylindrical electrodes with a diameter of 3.0 mm (electrode area 7 mm^2) and compared to those obtained with 6.0 mm diameter electrodes (electrode area 28 mm^2). A representative measurement is depicted in Figure A4.8, where the DBD has a gap width of 0.6 mm and 0.6 mm alumina on the secondary electrode. The shape of the distributions does not differ significantly when the electrode area is increased by a factor of 4. For the positive half-cycle, the ratio of the expected number of counts and those detected by the PHA circuit, $N^{+/-}_{measured}$ / $N^{+/-}_{expected}$ is 0.6 ± 0.2 for the larger area electrode, while it is 1.0 ± 0.1 for the smaller area electrode. Despite the PHA circuit missing a large number of counts for the larger electrode, the positive half-cycle distributions are very similar, indicating that missing counts, or many filamentary current pulses following in rapid succession, does not radically alter the resulting distribution. For the negative half-cycle, no current pulses are missed, even for the larger electrode, though in both cases at least half the total current does not occur in the form of filamentary current pulses, as discussed in the previous section. There

is a small difference in current density between the two electrode areas, 26 mA/cm^2 for 3.0 mm electrodes and 32 mA/cm^2 for 6.0 mm electrodes. In Figure A4.8, this difference in current density leads to a higher number of counts for the 6.0 mm electrodes. The discharge extends somewhat beyond the edges of the electrodes, so that the difference in current density and the number of counts, determined via Equation (A4.6), can be attributed to an underestimation of the surface area of the plasma. If the discharge extends, on average, a certain distance beyond the electrode edge, the 6.0 mm electrode will be affected more than the 3.0 mm electrode, leading to a greater overestimation of the current density in the 6.0 mm data. All further measurements are performed with electrode diameters of 3.0 mm, since this allows for the detection of all current pulses and minimizes the absolute underestimation of electrode area.

Chapter 5

From Discrete Filaments to Multi-filament Discharges

DBDs under sinusoidal driving voltage possess a nearly constant gap voltage, or burning voltage, during discharging. This allows for an equivalent circuit description of DBDs which assumes discharging occurs uniformly across the surface. Since DBDs actually consist of many spatially separated, transient microdischarges, a mechanism must exist which ensures filaments occur at a constant voltage, while the external voltage is changing. Individual filaments are also roughly equivalent, whether the number of filaments in a half-cycle is low, or high, or whether the pre-existing deposited charge density on the dielectric is low, or high. A mechanism consistent with all these observations is suggested; namely the constant redistribution of surface charge on the dielectric. It is found that, while part of the surface charge deposited during previous discharge cycles can be immobile on the surface over longer time periods, the larger fraction of the deposited surface charge must be mobile on time-scales of ≥ 100 ns.

5.1. Introduction

Dielectric Barrier Discharges (DBDs) in filamentary mode consist of many small, transient microdischarges with diameters of ~ 0.1 mm and durations on the order of several 10's of nanoseconds, distributed over the dielectric surface [51]. Each filament leads to current pulses with peak plasma currents > 10 mA, giving rise to average conductively transferred charge/pulse of up to several nC's. The collective behavior of many such filaments over a discharge period is the topic of this chapter. Under sinusoidal driving voltage, measurements of the charge in the DBD, Q, with respect to the external voltage, V, lead to parallelogram-shaped Q-V diagrams with a well-defined slope ζ_{diel} during the discharge period, which is lower than, or equivalent to, the dielectric capacitance C_{diel}, see Figure 5.1. These Q-V diagrams, are the topic of Chapter 2 of this thesis, where the filamentary discharge is essentially treated as a continuous plasma over time and modeled using a simple equivalent circuit. In Chapter 2 it was also made clear that the constant slope ζ_{diel} during discharging points to a constant gap voltage, termed the burning voltage U_b, and that this voltage does not change as a function of applied voltage amplitude. In Chapter 3 it was shown that because of this constant U_b, the only control over N_2 dissociation is achieved by changing the
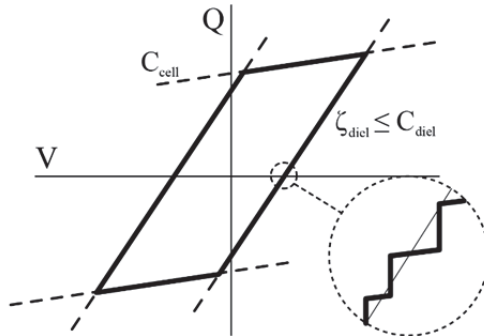
Figure 5.1: *Schematic Q-V diagram of a DBD under sinusoidal driving voltage. The continuous slope in the Q-V diagram during discharging actually consists of separate, fast changes in charge, leading to an average slope smaller than, or equal to, the dielectric capacitance C_{diel}.*

density of filaments and not the filaments themselves. In Chapter 4, moreover, the discrete nature of the plasma over time was investigated and the charge transferred by *individual* filaments determined. In the current chapter, the link between these discrete current pulses and the seemingly continuous behavior of the discharge averaged over many filaments is discussed by examining *Q-V* diagrams obtained from a DBD setup with an area small enough to contain no more than ~ 10 filaments per half-cycle. The main goal is to explain the constant slopes ζ_{diel} observed in *Q-V* diagrams, a problem directly related to why the burning voltage U_b remains the same for individual filaments throughout a discharge half-cycle.

The dynamics of individual filaments have been studied in detail, both through experiment and modeling, see *e.g.* [34,43,51,52] for reviews on this subject. The discussion here will be limited to cathode-directed filaments, where only the cathode is covered by dielectric material; the voltage in the gap drops from the surface of the anode to the surface of the cathode. The development of such a filament over time is summarized in Figure 5.2, where different phases are distinguished:

(1) The pre-breakdown phase. Electrons emitted from the cathode surface are accelerated to the anode by the electric field in the gap. A positive space charge is accumulated in front of the anode, because electrons are more mobile, leaving behind positive ions. The pre-breakdown phase lasts for at least 0.1 μs, before the start of each half-cycle [35,147]. Finally, a high local electric field strength is created in front of the anode, towards the cathode. If it reaches a certain critical level, the breakdown starts from near the anode surface towards the cathode. The voltage drop in the gap at breakdown is the burning voltage U_b. The plasma current associated with the pre-breakdown phase is only a few percent of the current through a filament [148].

(2) The propagation phase. The local electric field strength is enhanced by rapid ionization, giving rise to increased electron temperature, which further enhances field strength and ionization, etc. This ionization wave typically takes 1 - 2 ns to
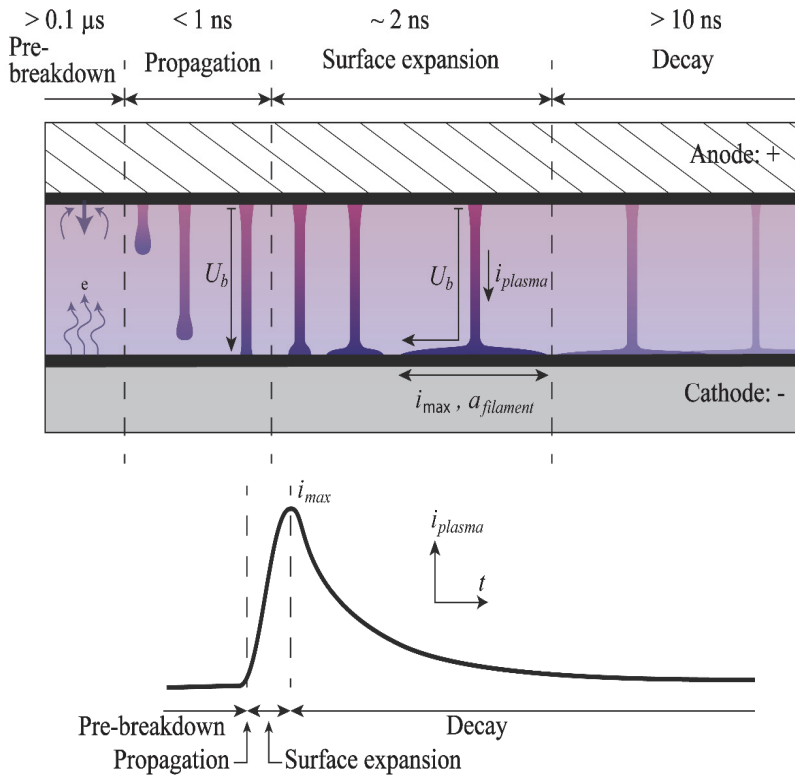
Figure 5.2: *Dynamics of an individual, cathode-directed filament with a conducting anode and a dielectric cathode. The external voltage drop and gap voltage drop are downward in this figure. The width of a filament is approximately 0.1 mm for air at atmospheric pressure, while the surface expansion is on the order of 1 mm [33,117,125].*

reach the cathode [52]. The voltage across the filament is the burning voltage U_b, with a plasma current i_{plasma} observable in the external circuit after the filament has propagated across the gap. Note that most of the voltage drop U_b is concentrated in the filament head because the trailing filament channel is highly conductive and, therefore, has a low voltage drop. Upon contact with the dielectric, most of the voltage U_b is within 200 μm of the cathode surface; the so-called cathode fall [27,28,46,118,149]. For single filament models, the filament channel was shown to have a voltage drop of 10 kV/cm, compared to around 400 kV/cm for the cathode fall

[38,145]. While the filament channel is quasi-neutral, charge separation occurs near the cathode surface.

(3) The surface expansion phase. As the filament reaches the dielectric surface of the cathode, its large potential with respect to the surrounding surface and the local removal of negative charge leads to a strong radial electric field, which allows the plasma to extend over the surface [33,118]. Most of the burning voltage U_b now drops from the location of the filament column to the edge of the surface expansion region [27,33]. The filament itself remains 'pinched' because of the short duration of the surface expansion, leaving both electron temperature and density high throughout the conductive plasma column. Maximum plasma current, i_{max}, is reached when the contact area of the filament with the cathode, $a_{filament}$, is highest [117].

(4) The decay phase. The radial electric field strength at the edge of the surface expansion wave decreases with distance from the filament, while at the same time the voltage drop across the filamentary plasma column becomes even lower. While the filament burns, it also removes more and more negative charge from the surface, negating the electric field across the filament channel. The combination of these processes leads to the decay phase of the filament, where the plasma current drops by an order of magnitude within < 100 nanoseconds [42,61,121,145]. Note that charge carriers in the filament channel may remain in the gap after filament extinction, particularly the positive and negative ions, which have a low mobility [117,145].

From the point of view of *individual* filaments, the plasma current is naturally limited by the rate at which charges can be conductively transferred from the dielectric surface to the opposite electrode. However, even in the absence of pre-existing charge on the dielectric, filaments could form simultaneously across the surface, provided they are sufficiently separated. This could lead to very high total (peak) currents through the DBD system, over a short time period of ~ 10 ns. If there is charge already on the dielectric, left behind during previous discharge cycles, simultaneous ignition of filaments across the surface
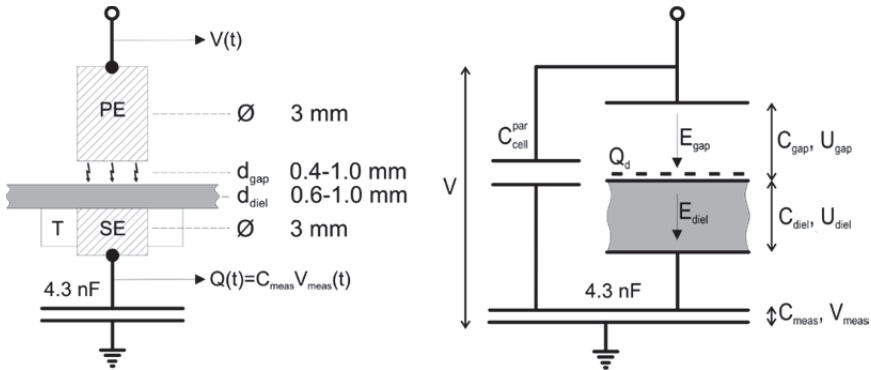
Figure 5.3: *Schematic of the setup, depicting the applied voltage measurement V(t) and the charge measurement Q(t), which is the voltage over the measurement capacitor $V_{meas}(t)$ multiplied by the capacitance C_{meas}. Primary electrode, secondary electrode and Teflon ring are indicated as PE, SE and T, respectively. The diagram on the right-hand-side depicts the equivalent circuit in terms of capacitances and deposited surface charge Q_d. The component C_{cell}^{par} is the parasitic capacitance of the DBD system from the primary electrode to the secondary electrode and measurement capacitor, with C_{gap} and C_{diel} ideal plate capacitors modeling the region where discharging takes place.*

may become even more likely, as this charge will allow for filament ignition at lower external voltages due to the resulting field-enhancement in the gap [34,37,38]. In this work, pre-existing charge, left behind by preceding discharges is referred to as *deposited* surface charge, Q_d, to distinguish it from polarization charge induced by the external voltage in the capacitive elements of the DBD. Note that we cannot distinguish between *deposited* or *donated* charges, *i.e.* if the dielectric becomes positively charged, we cannot say whether electrons were removed from the surface, or positive charges added, or a combination of both. Deposited charge Q_d only refers to the *net* charge state of the dielectric surface.

An important observation related to the deposited surface charge Q_d is that plasma current is not limited by the dielectric barriers. To clarify this point, consider an equivalent circuit such as that depicted on the right-hand-side of Figure 5.3, specifically the capacitances C_{gap} and C_{diel}. In the commonly used simplest electrical model of a DBD, the gap capacitance C_{gap} is bypassed by a parallel, conducting component which models the plasma. In such a model, the plasma current i_{plasma}

is limited by the dielectric barrier in series with the conducting component and can, therefore, never exceed the dielectric capacitance multiplied by the time-derivative of the external voltage:

$$i_{plasma}(t) \leq C_{diel} \frac{\partial V(t)}{\partial t} \quad . \qquad (5.1)$$

Equation (5.1) holds for the equivalent circuit, because the current through the circuit depends on the change of voltage across the dielectric and this change can never exceed the change in external voltage $V(t)$. This electrical model does not consider that the dielectric surfaces in DBDs can donate or deposit charge and that the plasma current is then only limited by the rate of change of this deposited charge Q_d:

$$i_{plasma}(t) = \frac{\partial Q_d(t)}{\partial t} \quad . \qquad (5.2)$$

In other words, if there is a current, i_{plasma}, flowing through the gap, this implies the charge state Q_d of the insulating dielectric surface is changing at a corresponding rate. This can be understood by again considering the maximum current that can pass through the dielectric capacitor: if there is, for example, an amount of deposited charge on the surface of the dielectric and it is removed at a certain rate through discharging in the gap, the voltage drop across the dielectric will change at an exactly proportional rate. Current through the dielectric is therefore always consistent with the plasma current, and there is essentially no maximum to the plasma current dictated by the external voltage. Of course, in a practical system the plasma current would be limited by the current that can be supplied by the power source, but for a well-designed system this current is never the limiting factor in the plasma current.

Why then does discharging of the dielectric occur in such a way that current pulses lead to an average slope which is commonly identified as the dielectric capacitance C_{diel} in Q-V diagrams [39]? Or, at low applied voltage and low filament density, why does the slope follow the effective dielectric capacitance corresponding to the fraction of

the surface participating in the discharge? Moreover, it was shown in Chapter 4, that there is no significant difference between charge/pulse distributions as a function of applied voltage amplitude, nor does the moment of ignition of a filament during the discharge half-cycle lead to large differences between filaments [117,121]. This implies that individual filaments are roughly equivalent, whether they ignite at low external voltage, or at higher external voltage, whether the number of filaments in a half-cycle is low, or high, or whether the pre-existing deposited charge density on the dielectric is low, or high.

A physical mechanism must exist which prevents the entire surface from discharging at the same external voltage and which gives rise to the parallelogram-shaped Q-V diagrams for DBDs with sinusoidal driving voltage, without that mechanism having a significant influence on the charge/pulse or burning voltage from filament to filament. The main goal of this work is to elucidate this mechanism.

5.2. Experimental setup

5.2.1 Small area DBD

A small area planar DBD with a custom generator and transformer circuit was built, providing sinusoidal applied voltages with peak-to-peak amplitudes between 1 - 10 kV_{pp} at a frequency of 100 kHz to a brass top (primary) electrode of 3.0 mm diameter, which is adjustable in height to provide various gap widths. The bottom (secondary) electrode also has a diameter of 3.0 mm and is covered by dielectric material, which in this work consists of alumina of 1.0 or 0.6 mm thickness and a relative permittivity, $\varepsilon_r = 10.0$. The surface area of the dielectric material is large with respect to the electrode area so that it always extends beyond the edges of the electrodes. To prevent unwanted discharging underneath the dielectric, the space around the secondary electrode is insulated using a Teflon ring, with silicone gel providing an air-tight seal. The DBD is operated in ambient air throughout this work, with no humidity control.

The charge in the system, $Q(t)$, is measured using a 4.3 nF polystyrene-based capacitor in series with the DBD, as indicated on the left-hand-side of Figure 5.3. The measurement capacitance is far greater than the maximum capacitance of the DBD configuration, which is between 0.24 – 0.33 pF, and therefore has no appreciable effect on the voltage drop across the DBD. The voltage measurements on the capacitor include a low-pass filter to remove RC components above 50 MHz, effectively smoothing the signal. The applied voltage is measured simultaneously using a custom-built voltage probe with an attenuation of 1000:1. Both charge and voltage data were stored using an Agilent InfiniiVision 5000 digital oscilloscope. Calibration measurements were performed to ensure that both voltage probe and current monitor have the same time delay within the sampling rate of the scope (~ 0.4 ns).

5.2.2 Approach

Q-V data is acquired for 8 different configurations, with gap widths of 0.4, 0.6, 0.8 and 1.0 mm and dielectric thicknesses of 0.6 and 1.0 mm, over the widest possible range of external voltage amplitudes and corresponding filament number densities.

We study only the steady-state behavior of the system, *i.e.* when a fully developed distribution of deposited charge is present on the dielectric. To clarify the concept of steady-state operation, consider that there is initially no deposited charge in the DBD system, as these charges are only expected to remain stable for several seconds [150]. While the very first filament ignites at relatively high voltage, the accumulation of deposited charge on the dielectric leads to an enhanced field in the gap for the following voltage half-cycle of opposite polarity. For a fully developed distribution of surface charge, a lower external voltage amplitude will then be sufficient to maintain the discharge [151]. To compensate for the initial absence of deposited charge, the discharge is first ignited at this relatively high external voltage amplitude, after which the voltage is turned back to just above the amplitude at which discharging is still observed. From this point several Q-V measurements are performed with increasing applied voltage amplitude. In this way, the development of the steady-
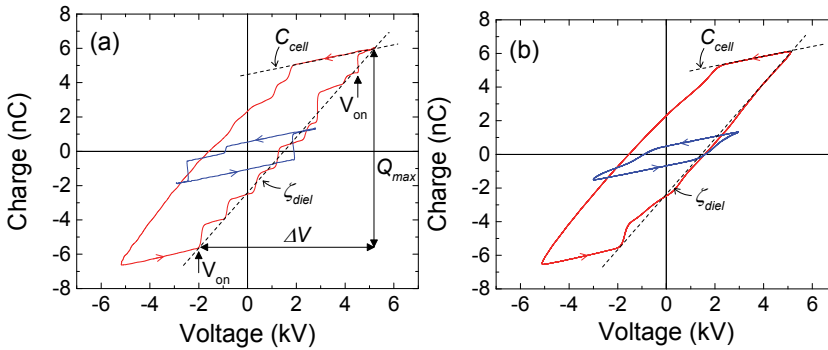
Figure 5.4: *(a) Single-shot Q-V diagrams of an asymmetric DBD with 0.6 mm alumina and a 0.6 mm gap width at applied voltage amplitudes of 5.6 kV$_{pp}$ (blue) and 10.4 kV$_{pp}$ (red). Individual filamentary discharges are clearly distinguishable. For the higher applied voltage amplitude, the downward slope on the left is mostly smooth, indicating a Townsend-like discharge. (b) Averaged Q-V diagram over 4096 cycles.*

state discharge over the widest possible range of filament number density is studied. Both single-shot and averages over 4096 full cycles are measured at each applied voltage amplitude. At every external voltage amplitude, the DBD is allowed to heat up for several minutes to ensure a steady-state. Examples of single-shot and average *Q-V* diagrams are depicted in Figure 5.4(a) and Figure 5.4(b), respectively.

The positive half-cycle is defined as the period in which current is positive, *i.e.* from the primary electrode (anode) to the secondary electrode (cathode) and $Q(t)$ is increasing. During the negative half-cycle the current is negative, *i.e.* from the secondary electrode (anode) to the primary electrode (cathode) with $Q(t)$ decreasing. The focus in this work is on the positive half-cycle, where the single-shot data such as depicted in Figure 5.4(a) shows a stepped increase of Q with increasing external voltage V, consistent with individual filamentary discharges. We refer to this stepped slope as the 'staircase' throughout this work.

109

5.3. Theory

5.3.1 Charge measurements

During steady-state operation of the DBD, negative deposited surface charges are accumulated on (during the negative half-cycle) or removed from (during the positive half-cycle) the dielectric surface. A basic equation can be derived relating the measured charge in the system Q to the external voltage V and the deposited surface charge Q_d, based on the equivalent circuit depicted on the right-hand-side of Figure 5.3. With the full derivation given in the Appendix, the result is:

$$Q(t) = C_{meas}V_{meas}(t) = \left(C_{cell}^{par} + C_{cell}^{ideal}\right)V(t) + \left(1 - \frac{C_{cell}^{ideal}}{C_{diel}}\right)Q_d(t), \quad (5.3)$$

where C_{meas} and V_{meas} are the measurement capacitance and voltage, respectively, C_{cell}^{par} the parasitic cell capacitance and C_{cell}^{ideal} the cell capacitance of the discharging region, consisting of C_{gap} and C_{diel} in series. It is assumed in the derivation of Equation (5.3) that C_{gap} and C_{diel} are ideal plate capacitors of equal area, with no edge effects. Note that C_{cell}^{ideal}, C_{gap} and C_{diel} are the *apparent* capacitances of the discharging region as they appear in the equivalent circuit, making the circuit consistent with the Q-V diagrams. The equivalent circuit, by definition, assumes charging and discharging of the dielectric occurs uniformly. The *apparent* capacitance C_{diel} can be higher than the *actual* capacitance C_{diel}^{actual} of the dielectric because the *apparent* discharged area $A_{discharge}$ of the dielectric is overestimated by neglecting the influence of non-uniform deposited charges. This is illustrated schematically in Figure 5.5.

Note that Equation (5.3) is essentially the same as the equation for plasma current and conductively transferred charge in Chapter 2, provided $C_{cell}^{par} = 0$. The effect of parasitic capacitance on the charge measurement is no more than an additional term $C_{cell}^{par}V$, which can be

Deposited charge Q_d on area $A_{discharge} \propto C_{diel}$

Deposited charge Q_d on area $A_{discharge}^{actual} \propto C_{diel}^{actual}$

σ_d

x

Dielectric

Electrode

(a)   (b)
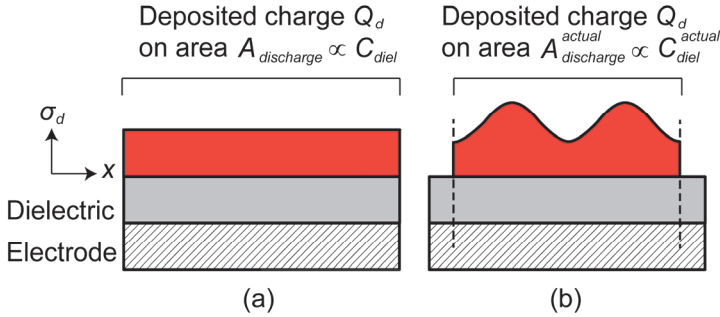
Figure 5.5: *Schematic of the charge distribution on the dielectric at the beginning of a half-cycle for (a) an equivalent circuit model, which implicitly assumes all charge on the dielectric is uniformly distributed and (b) a more realistic charge distribution. The total charge Q_d is the same in both cases and so is the apparent capacitance C_{diel}, but for (b) the physical area affected by deposited charges $A_{\mathrm{discharge}}^{actual}$ is smaller, as well as the actual capacitance of the underlying dielectric $C_{\mathrm{diel}}^{actual}$.*

easily determined, as described in the Appendix, A5.2, and corrected for by subtracting it from the *Q-V* diagrams [70]. The relevant *apparent* capacitances can be written as $C_{cell}^{ideal} = C_{cell} - C_{cell}^{par}$ and $C_{diel} = \zeta_{diel}^{sat} - C_{cell}^{par}$. Equation (5.3) also shows that *Q-V* diagrams need not be symmetric around the *Q*-axis and that offsets can occur if $Q_d(t)$ does not average out to zero over a full period.

In our analysis, we assume the gas in the gap is quasi-neutral after each filament has ignited and any net charge is found near the dielectric. For a quasi-neutral volume plasma, the electric fields will be constant, the same as for an empty gap. We treat the filamentary discharges as near-instantaneous events which locally transfer charge to and from the dielectric surface. This is a reasonable assumption, considering nearly all of the plasma current is concentrated within less than a dozen ten nanosecond bursts, compared to the 5 microsecond duration of a half-cycle. The concentration of residual plasma, present between filamentary discharges, is discussed in the Appendix, A5.1. It is concluded that any residual charge carriers in the gap have a concentration $\leq 10^{11}$ cm^{-3}, primarily consisting of positive and negative ions.

5.3.2 Maximum apparent discharge area and fractional discharge area

The maximum *apparent* area covered by the discharge, $A_{discharge}$, can be calculated from the *apparent* dielectric capacitance C_{diel} via:

$$A_{discharge} = \frac{d_{diel}}{\varepsilon_0 \varepsilon_r} C_{diel} . \qquad (5.4)$$

As already mentioned, C_{diel} may be larger than the actual capacitance C_{diel}^{actual} of the dielectric covered by discharges, so that $A_{discharge}$ via Equation (5.4) is an overestimation. Since we lack data on the true discharged area, the maximum area $A_{discharge}$ will be used regularly throughout this work, though deviations will be discussed as needed. The effective dielectric capacitance, ζ_{diel}, is a key parameter. The same as in Chapter 2, it is defined here as:

$$\zeta_{diel} = \frac{Q_{max}}{\Delta V} , \qquad (5.5)$$

with Q_{max} the *average* change in $Q(t)$ during a discharge half-cycle and ΔV the corresponding *average* change in external voltage $V(t)$, as indicated in Figure 5.4(a). The surface coverage β, which includes the effect of surface expansions, is calculated using [152]:

$$\beta = \frac{\zeta_{diel} - C_{cell}}{\zeta_{diel}^{sat} - C_{cell}} , \qquad (5.6)$$

where C_{cell} is the cell capacitance, obtained directly from the *Q-V* diagrams as indicated in Figure 5.4(a) and ζ_{diel}^{sat} the saturated effective dielectric capacitance at high applied voltage amplitude (equal to $\zeta_{diel}^{sat} = C_{diel} + C_{cell}^{par}$).

Note that Equation (5.6) is derived from the equivalent circuit model [152]. The constant ignition and extinction of individual filaments over the discharge area is treated as a *uniform* plasma with a time-dependent plasma current corresponding to the sum of plasma current

from individual filaments present at a given time and an apparent area $\beta A_{discharge}$ corresponding to the area (dis-)charged by all filaments during a half-cycle. Here, Equation (5.6) will be related to the discrete case where individual filaments are distinguishable in the Q-V data, by comparing the value of β over many cycles to the average number of filaments per half-cycle N. The coverage β is independent of the interpretation of the various (effective) capacitances, it is simply a measure of the 'saturation' of the discharge as it progresses from no discharge ($\zeta_{diel} = C_{cell}$, $\beta = 0$) to a discharge with a maximum coverage ($\zeta_{diel} = \zeta_{diel}^{sat}$, $\beta = 1$).

5.3.3 Effective dielectric capacitance and 'staircase'

The definition of the effective dielectric capacitance, ζ_{diel}, as described by Equation 5.5, can be rewritten to include the characteristics of the 'staircase' as seen for the positive half-cycle in Figure 5.4(a). The *average* horizontal step size in the Q-V diagrams during a discharge, $\langle dV \rangle$, is equal to

$$\langle dV \rangle = \frac{\Delta V}{N}, \tag{5.7}$$

with ΔV the change in external voltage during the discharge period and N the *average* number of filaments per half-cycle. Similarly, the *average* vertical step size, $\langle dQ \rangle$, can be defined as

$$\langle dQ \rangle = \frac{Q_{max}}{N}, \tag{5.8}$$

though it should be emphasized that $\langle dQ \rangle$ is not equal to the average charge conductively transferred through the gap by a filament. This latter, referred to as the average charge/pulse, $\langle q \rangle$, can be defined as

$$\langle q \rangle = \frac{\Delta Q_{dis}}{N}, \tag{5.9}$$

where ΔQ_{dis} is the total *average* conductively transferred charge during a discharge half-cycle, as discussed in Chapter 2. Using

Equation 2.9 from Chapter 2, Q_{max} is equal to the sum of ΔQ_{dis} and the capacitively transferred charge during a half-cycle:

$$Q_{\max} = \Delta Q_{dis} + (1 - \beta) C_{cell}^{ideal} \Delta V + C_{cell}^{par} \Delta V , \qquad (5.10)$$

where $1 - \beta$ is the fraction of the electrode area behaving as a capacitor during the discharge and $C_{cell}^{par} \Delta V$ the contribution of the parasitic capacitance. Substituting Equation (5.10), (5.9) and (5.7) in (5.5) we obtain:

$$\zeta_{diel} = (1 - \beta) C_{cell}^{ideal} + C_{cell}^{par} + \frac{\langle q \rangle}{\langle dV \rangle} , \qquad (5.11)$$

which shows that the *average* slope of the 'staircase' results from two purely capacitive elements with the addition of vertical steps with a height corresponding to the average charge/pulse $<q>$, followed by an average increase of the external voltage $<dV>$. Comparing Equation (5.11) to Equation (2.6) from Chapter 2 we find for the relationship between $<dV>$, $<q>$ and β [152]:

$$\frac{\langle q \rangle}{\langle dV \rangle} = \beta C_{diel} . \qquad (5.12)$$

Equation (5.12) is essentially the definition of C_{diel} for a 'staircase' slope with vertical step size $<q>$ and horizontal step size $<dV>$. Over the following sections we will discuss the interpretation of C_{diel} in more detail. While β, $<q>$ and $<dV>$ are only defined over an entire discharge half-cycle, individual filaments will deviate from this ideal behavior, possessing a charge/pulse q with subsequent voltage increase dV which may be higher, or lower, than the average. Both the causes of, and the influence of these deviations on the behavior of the discharge will be included in the treatment of the data.

5.4. Observations from the *Q-V* diagrams

5.4.1 Negative half-cycle: partial APTD

Returning to the single-shot and averaged Lissajous figures depicted in Figures 5.4(a,b), the decrease of Q with decreasing external voltage (negative half-cycle), only shows individual steps during the first part of the discharge, but rapidly becomes smooth. This was already discussed in Chapter 4, where it was found that, depending on DBD geometry, up to 75% of total plasma current is not filamentary, but continuous in nature. This discharge can be identified as an Atmospheric Pressure Townsend Discharge, or APTD. This discharge is homogeneous over the (partial) area of the DBD and has low plasma current density and low volume ionization compared to the filamentary discharge, where current and plasma species are concentrated in various, separate ~ 100 μm channels.

Following Naudé *et al.* [66], during APTD, the voltage drop in the gap U_{gap} will be nearly constant, so that the plasma current i_{plasma} through the DBD system is described by:

$$i_{plasma}(t) = C_{diel} \frac{\partial V(t)}{\partial t}.$$ (5.13)

Both the left- and right-hand-side of Equation (5.13) are plotted in Figure 5.6(a), showing that this relation indeed holds during part of the negative half-cycle. Note also that filamentary current pulses always significantly exceed $C_{diel}\partial V(t)/\partial t$. Figure 5.6(b) shows the time-integrated plasma current during the APTD, q_{APTD}, as a function of the total conductively transferred charge ΔQ_{dis} for three DBD configurations. From the results plotted in Figure 5.6(b), it is found that the contribution of APTD increases with conductively transferred charge ΔQ_{dis} (which increases with applied voltage amplitude) and is higher for thinner dielectrics and wider gaps.
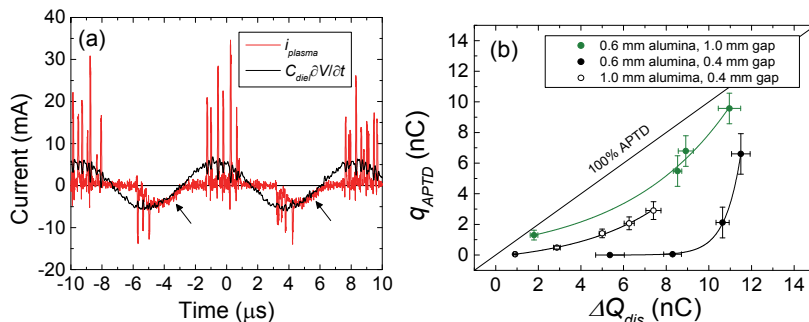
Figure 5.6: *(a) Plasma current i_{plasma} versus $C_{diel}\partial V/\partial t$ for 0.6 mm alumina and 0.6 mm gap width at 10.5 kV_{pp}, with arrows indicating the APTD during the negative half-cycle. (b) Charge deposited via APTD as a function of the total conductively transferred charge ΔQ_{dis}. For each DBD configuration depicted the applied voltage amplitude increases from 7 kV_{pp} to 10 kV_{pp}. The lines are exponential fits and serve as guides to the eye.*

APTD in air was also observed by Osawa *et al.* using double alumina dielectrics and a 2 mm gap width at applied voltage frequencies up to 1.1 kHz [76]. In an asymmetric DBD configuration, with on one side alumina and on the other a glass dielectric, they reported alternating generation of filamentary discharge and APTD every half-cycle [77]. In the setup used here, we observe APTD when the metal electrode serves as cathode. Following the work of Yurgelenas *et al*, we argue that the contribution of APTD to the discharge is inversely related to the degree of non-uniformity of the electric field at the metal electrode [38]. The pre-breakdown phase, depicted in Figure 5.2, is essentially a Townsend discharge, where electrons released from the cathode multiply as they are accelerated through the gas gap. Only when the resulting positive space charge at the anode reaches some critical value, a local transition to a filament occurs. It was shown by Yurgelenas *et al*, using a computational model, that for variations in the electric field perpendicular to the electrode surfaces of $< 1\%$, or for periodic variations in the surface charge with a length scale of ≥ 2 mm, transition of the initial Townsend discharge to a filament does not occur, even at gap voltages equal to the breakdown voltage [37,38]. Since a non-uniform charge distribution can only be found on the dielectric, the perpendicular electric fields at the metal electrode

116
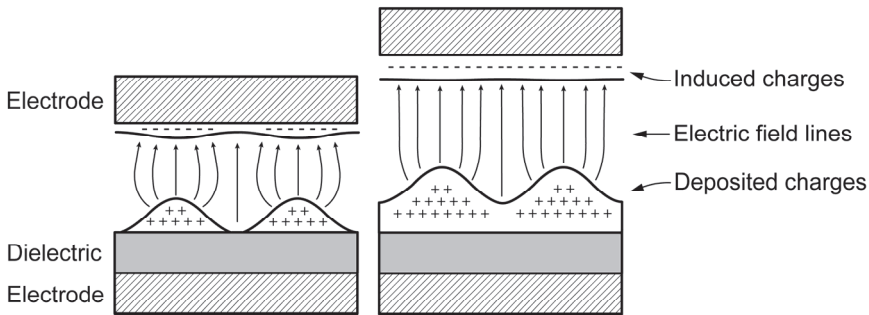
Figure 5.7: *Schematic representation of non-uniform distributions of deposited surface charges on the dielectric, which induces surface charges in the opposing metal electrode. For clarity the induced charges are depicted outside the top electrode, while in reality they are within the metal surface. The induced charges are more uniformly distributed than the deposited charges, so that the electric field in the gap perpendicular to the electrode surfaces will be more uniform near the top electrode than near the dielectric. This effect increases with increasing gap width as well as with increased residual (quasi-neutral) plasma in the gap.*

are mostly uniform along the surface. Any surface charges on the metal electrode are induced by the deposited charges on the opposing dielectric. This is sketched in Figure 5.7. This relatively uniform field, along with a lower work function for the metal electrode, may suppress formation of filaments during the negative half-cycle. This explanation is consistent with Figure 5.6(b), since an increase in gap width will lead to a relatively more uniform field near the metal electrode. Moreover, as voltage is increased and more plasma is ignited in each half-cycle, the time-averaged density of residual charge carriers in the gap will increase. This residual plasma will further shield the metal electrode from the non-uniform charge density on the dielectric. This suppresses filament formation and, therefore, leads to a larger contribution of APTD to the discharge in the negative half-cycle.

5.4.2 Memory effect

Bogaczyk *et al.* show that the memory effect of individual filaments, related to the pattern of deposited surface charges on the dielectric, is active for 10 - 12 consecutive voltage cycles in He/N_2 mixtures [135].
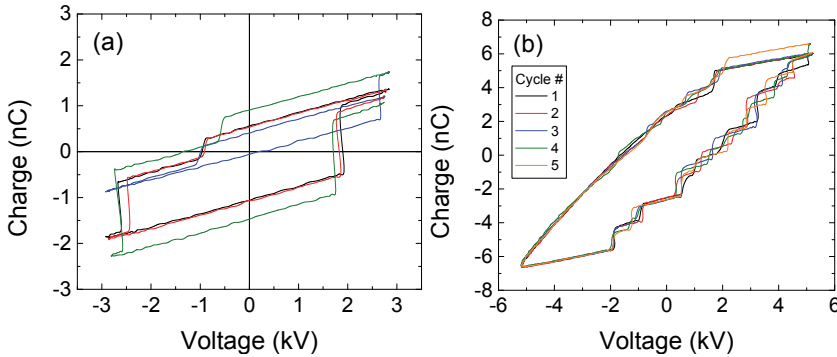
Figure 5.8: *(a) Cycle-to-cycle variation in surface charge observed at low filament density for 4 full cycles for the same DBD configuration as Figure 5.4. (b) Cycle-to-cycle variation at high filament density.*

Similarly, Akishev *et al.* find that individual filaments in air can re-ignite in the same location for 300 consecutive half-cycles [117,121]. It should be noted that this memory effect is related to the spatial reproducibility of filaments, while the temporal reproducibility is known to be much weaker, *i.e.* a filament at a given location in the DBD may reform at random times within the half-cycle [35,117,121]. Over 4096 voltage cycles, the pattern of surface charges changes sufficiently to lead to randomized charge/pulse, while the moments of discharge of individual filaments may become randomized after a single voltage cycle.

Here, no data is available regarding the spatial memory effect and only the temporal memory effect can be observed. Figures 5.8(a,b) show the cycle-to-cycle variation for a single DBD configuration at both high and low filament number density. In Figure 5.8(a) there are usually 2 filaments ignited during the negative half-cycle and only 1 during the positive half-cycle. During the 3rd negative half-cycle one filament is skipped, which also affects the subsequent positive half-cycle, where a larger external voltage is now needed to ignite the filament. The moments of discharge are usually reproduced to within several tenths of kV's. For Figure 5.8(b), at higher filament number density, only the first 3 filaments of the positive half-cycle appear to show this same temporal reproducibility. The variation in moment of ignition of later filaments is actually due to there being more or less

118

filaments per half-cycle N. While the average number of filaments is 8, the 3rd cycle has 7 and the 4th has 10. During the 3rd cycle, the 7 filaments have on average a higher charge/pulse, while during the 4th cycle the charge/pulse is lower. Since the average slope (ζ_{diel} in Figure 5.4(a)) is always roughly the same from cycle to cycle, variations in moment of discharge are actually due to variation in the charge/pulse of preceding filaments. In other words, if the charge/pulse q of a preceding filament is low, a succeeding filament will tend to ignite after a relatively lower increase in external voltage dV and, therefore, the time between filaments is shorter. Deviations of the charge/pulse q from the average $<q>$, lead to roughly proportional deviations dV from $<dV>$, which will leave the average slope ζ_{diel}, described by Equation (5.11), virtually unaffected.

The influence of the APTD on the (spatial) memory effect is unknown, though the memory effect is likely reduced by the uniform charging of the surface. For the purposes of this work, however, it is sufficient to assume that the memory effect is active to some extent, as it is a common feature of filamentary DBDs.

5.5. Quantitative analysis of Q-V diagrams

5.5.1 Capacitances and discharge area

By determining the average slope during discharging, defined by Equation (5.5), the effective dielectric capacitance ζ_{diel} is obtained over a wide range of conditions. To reduce errors, this was done for the Q-V data averaged over 4096 cycles, as depicted in Figure 5.4(b). The results are plotted in Figure 5.9 as a function of applied voltage amplitude for all 8 DBD configurations used in this work. For each dielectric thickness, the effective capacitance ζ_{diel} saturates to a constant value ζ_{diel}^{sat}. The fitting function is a single-exponential, as proposed by Reichen *et al.* for the increase of effective dielectric capacitance with applied voltage [71]. Total cell capacitance C_{cell} is found by linear fits of the Q-V data between discharges and was found to be roughly independent of applied voltage amplitude for a given DBD configuration. We find ζ_{diel}^{sat} = 1.17 pF and 1.59 pF, depending
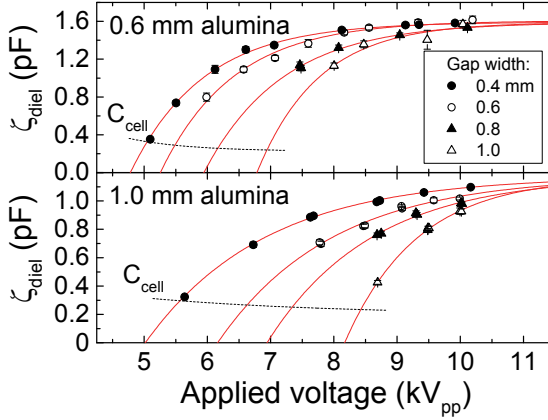
Figure 5.9: *Average effective dielectric capacitances, ζ_{diel}, for 8 different DBD configurations as a function of applied voltage amplitude. The red lines are least-squared fits of single exponential functions saturating to the same value for each of the two dielectric thicknesses. The dotted lines indicate the cell capacitance C_{cell} for a given configuration. Within the error, there is no distinction between positive and negative cycles.*

on dielectric thickness, and C_{cell} = 0.24 pF up to 0.33 pF, depending on both gap width and dielectric thickness. Using the method described in the Appendix, the lowest parasitic capacitance C_{cell}^{par} = (0.08 ± 0.01) pF is found for a DBD configuration with 1.0 mm alumina and 0.4 mm gap and the highest, C_{cell}^{par} = (0.16 ± 0.02) pF, for 0.6 mm alumina and 1.0 mm gap. The error also includes a 4% uncertainty in dielectric thickness and gap width. We find dielectric capacitances C_{diel} = (1.05 ± 0.06) pF and (1.44 ± 0.06) pF for alumina thicknesses of 1.0 and 0.6 mm, respectively. Note that while the dielectric capacitance C_{diel} does not deviate strongly from ζ_{diel}^{sat}, the contribution of the parasitic capacitance C_{cell}^{par} to the total cell capacitance C_{cell} can be close to 50%.

Applying Equation (5.4), an *apparent* discharge area $A_{discharge}$ = (11.7 ± 1.1) mm^2 and (9.9 ± 0.8) mm^2 is found for 1.0 and 0.6 mm alumina, respectively, including a 4% error in dielectric thickness. Within the error, similar values of $A_{discharge}$ are found for the two dielectric thicknesses, though it may be possible that the discharge area is

physically larger for a thicker dielectric. Considering that the secondary electrode only has a diameter of 3 mm (area 7.1 mm^2), the discharge appears to extend, on average 0.4 mm and 0.3 mm beyond the electrode edge for a dielectric thickness of 1.0 mm and 0.6 mm, respectively. While the discharge seems slightly conical at high applied voltage amplitudes, with a wider base at the dielectric surface than the area of the bottom electrode, the area $A_{discharge}$ should be verified independently using *e.g.* Lichtenberg images. The discharged area $A_{discharge}$ calculated using Equation (5.4) may be overestimated because the dielectric capacitance C_{diel}, as derived from the *Q-V* data using the equivalent circuit model, is only an apparent value. As depicted in Figure 5.5, a non-uniform charge distribution may lead to a lower actual discharged area $A_{\text{discharge}}^{actual}$.

5.5.2 Step sizes *<dV>* and *<q>* as a function of *N*

The average horizontal step size in the *Q-V* diagrams during a discharge, *<dV>*, is defined by Equation (5.7). The average number of filaments can be determined directly from the *Q-V* diagrams in Figures 5.5(a,b), but is determined for a larger number of cycles via the method discussed in Chapter 3, where current pulse counting is achieved with a time resolution of 50 ns using a fast analog circuit [153]. Both *<dV>* and *ΔV* from averaged *Q-V* data are depicted in Figure 5.10. While *ΔV* increases with the number of filaments, *<dV>* asymptotically decreases to a constant value with increasing *N*.

The average charge/pulse *<q>* was determined in Chapter 3 to be nearly constant with increasing number of filaments. For example, from ~ 1 filament per half-cycle to ~ 10 filaments per half-cycle, *<q>* decreases from 1.0 nC to 0.9 nC for 0.6 mm alumina and from 0.8 nC to 0.7 nC for 1.0 mm alumina, for a gap width of 0.6 mm.

Since *<q>* is virtually independent of *N*, while *<dV>* decreases with *N*, this suggests there is interaction between individual filaments: even though they occur one after the other during a half-cycle and have, on average, the same charge/pulse, the step size *<dV>* depends on the number of filaments that occur during that half-cycle. This is
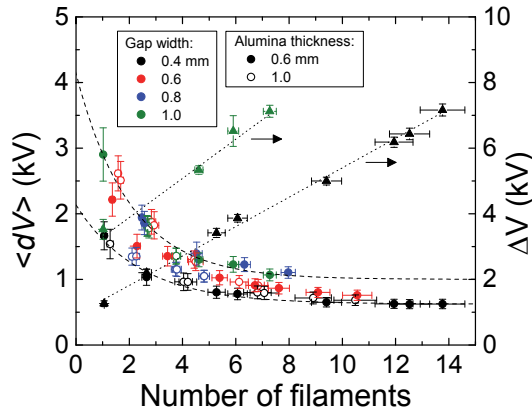
Figure 5.10: *Average horizontal step size <dV> between filaments in the single-shot Q-V diagrams as a function of the number of filaments during the positive half-cycle. For 1 filament per half-cycle <dV> is the remaining external voltage increase until maximum voltage is reached. Triangles indicate ΔV for a gap width of 0.4 and 1.0 mm with 0.6 mm alumina. The data is averaged over 4096 voltage cycles. The dashed and dotted lines are guides to the eye.*

similar to the observation made for individual filaments in Section 4.2, where variations in charge/pulse q of preceding filaments affect the external voltage increase dV after which the next filament ignites, so that the 'staircase' is seen to roughly maintain the same slope ζ_{diel}. According to Equation (5.12), $<dV>$ should be inversely proportional to the surface coverage β.

5.5.3 Surface coverage β as a function of N and extent of surface expansion

By comparing the effective dielectric capacitance ζ_{diel} to its saturation value ζ_{diel}^{sat}, the surface coverage during a half-cycle β can be determined, as defined by Equation (5.6). By analyzing the data as a function of filament number density N, the average coverage of a single filament can be related to the average coverage attained by multiple filaments, providing additional insights into the way multiple filaments interact. In Figure 5.10, β is plotted as a function of the average filament number density $N/A_{discharge}$ during the positive half cycle. Plotting the data as a function of $N/A_{discharge}$ is convenient for
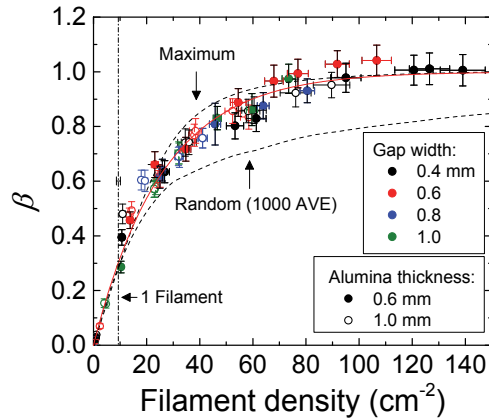
Figure 5.11: *Average surface coverage of the discharge β as a function of filament density $N/A_{discharge}$ during the positive half-cycle. The vertical line indicates when only a single filament ignites per half-cycle. The red line is Equation (5.14), while the two dashed lines indicate the maximum coverage by equidistant filaments (top) and the average coverage over 1000 cycles of randomly placed filaments (bottom), all with $<a_{filament}>/A_{discharge} = 0.32$.*

comparing the data and reveals a universal trend for *β* as a function of filament number density. The average number of filaments for each DBD configuration and applied voltage was obtained using the method discussed in Chapter 4. Since there is little difference in ζ_{diel} between positive and negative half-cycles, the same surface coverage applies to the negative half-cycle, though the filament number density only applies to the positive half-cycle. In Figure 5.11 there are also several data points with less than one filament per half-cycle, corresponding to < 10 filaments/cm². These belong to discharges at applied voltage amplitudes close to the extinction voltage, where filaments are observed to ignite only once in every 2 - 4 full cycles. This leads to proportionally lower ζ_{diel} slopes in the averaged Lissajous figures such as depicted in Figure 5.4(b), making *β* determined via Equation (5.7) a time-averaged value, no different from all other data points in the figure.

Of special interest here is the average surface coverage when there is only a single filament in the gap. Depending on dielectric thickness, *β* ≈ 0.36 for 0.6 mm alumina and *β* ≈ 0.30 for 1.0 mm alumina. Due to the difference in total discharge area this corresponds to an average

area per filament $\langle a_{filament} \rangle \approx 3.5 \text{ mm}^2$ and a radius of $\sim 1.1 \text{ mm}$ for both alumina thicknesses. This area can be identified as the average extent of a single surface expansion. As discussed in the introduction, the radial extent of the surface expansion is limited by the decreasing radial electric field strength at the edge of the surface expansion wave with distance from the filament channel. The extent of the surface expansion found here is consistent with numerical models in air: Papageorghiou *et al.* find $\sim 1.4 \text{ mm}$ for a cathode-directed streamer [33], and Akishev *et al.* a radius of 2 mm [117]. Based on their numerical model, Gibalov *et al.* state that the radial extent of the cathode-directed streamer is approximately proportional to the square root of the relative dielectric permittivity, resulting in 0.6 mm in the case of alumina [125].

While a single filament covers an average area $\langle a_{filament} \rangle \approx 3.5 \text{ mm}^2$, the addition of a second filament leads to an increase in coverage to only $\sim 5.6 \text{ mm}^2$. There is, consequently, a 20% overlap between the surface expansions of the two filaments if both filaments cover an average area $\langle a_{filament} \rangle$. To a good approximation, the *maximum* coverage by a number N overlapping circles with area $\langle a_{filament} \rangle$ within a larger circle with area $A_{discharge}$ is:

$$\beta = 1 - \left(1 - \frac{\langle a_{filament} \rangle}{A_{\text{discharge}}} \right)^N , \qquad (5.14)$$

which is based on the principle that the first filament leaves a fraction $1 - \langle a_{filament} \rangle / A_{discharge}$ of the electrode area uncovered, with the next filament leaving, on average, that same fraction of the remaining area uncovered, etc. Fits of this equation are included in Figure 5.11. For comparison to Equation (5.14), two more models are included in Figure 5.10, both based on individual filaments covering an area $\langle a_{filament} \rangle$. The first is the maximum coverage that can be attained by N overlapping circles, which assumes equidistance, illustrated in Figure 5.12. The second model determines the average coverage attained by N circles if their placement within the discharge area is entirely random, but averaged over 1000 cycles. The results of both models, with $\langle a_{filament} \rangle / A_{discharge} = 0.32$, are obtained numerically

Number of filaments →

2 3 4 5 6

54 % 69 % 79 % 86 % 90 %

Area covered →
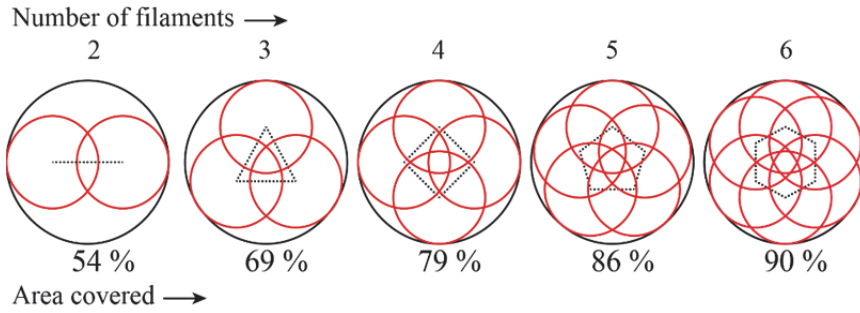
Figure 5.12: *Equidistant, overlapping circles, corresponding to the area of a single surface expansion (red), within the total discharge area (black) for a ratio $<a_{filament}>/A_{discharge}$ = 0.32. The discharged area per half-cycle depicted here corresponds well with Equation (5.14) and roughly matches the surface coverage β in Figure 5.11. The black dotted lines connect the locations of the individual filaments.*

using the software package *Mathematica*. Comparing the two models in Figure 5.11 indicates that the average surface coverage *β* is described best by Equation (5.14), which is close to the model where equal filaments form as far away from each other as possible within the confines of the electrode area, as depicted in Figure 5.12. Note that Equation (5.14) only gives a close approximation of the coverage depicted in Figure 5.12, under the condition that $<a_{filament}>/A_{discharge} >$ 0.25, while the actual analytical expression for the surface coverage depicted in Figure 5.12 is far more cumbersome and not provided here. The condition $<a_{filament}>/A_{discharge} > 0.25$ arises from the fact that at lower ratios, the diameter of the smaller circles is less than half that of the bigger circle and a hole will appear in the middle of the electrode.

It should be stressed that Equation (5.14) is only consistent with the average behavior over many cycles and that filaments are also observed to form near the electrode edge. A filament forming near the electrode edge could have a surface expansion wave propagating beyond the (secondary) electrode. Charging of the dielectric beyond the electrode edge still contributes to the total charge *Q* measured on the measurement capacitor, and this effect is already implicitly included in the determination of the parasitic capacitance. The main conclusion is that individual surface expansion waves will overlap

with those of preceding filaments, as depicted in Figure 5.12. Since in reality not all filaments are equal during a half-cycle, variations in the area per filament $a_{filament}$ may be expected. This relation between the charge/pulse q of an individual filament and its area remains to be investigated, but over many cycles the assumption of filaments with average $<a_{filament}>$ corresponding to an average charge/pulse $<q>$ remains valid.

5.6. Multi-filament dynamics

5.6.1 The 'staircase': evidence of mobile deposited charge

A summary of the observations made in the preceding sections will be given below, followed by an explanation of the 'staircase' observed for multi-filament discharges.

In terms of electrical equivalent circuits for DBDs, there is no limit to the plasma current in the gap for a (dis-)charging dielectric surface. In the absence of a mechanism preventing filaments from occurring simultaneously, the entire dielectric surface could, theoretically, be discharged at once. Nevertheless, filaments are separated in time and follow a 'staircase' in the Q-V diagram with step sizes in the external voltage *between* filaments dV roughly corresponding to the charge/pulse of the *preceding* filament q (Figure 5.7). For Q-V diagrams averaged over many cycles, the average charge/pulse $<q>$ is independent of the number of filaments per half-cycle N, while $<dV>$ asymptotically decreases to a constant value as a function of N (Figure 5.10). The moments of ignition of multiple filaments within a half-cycle are clearly not completely random, but give a slope in the Q-V diagram equal to ζ_{diel}.

In Figure 5.11 it is shown that the average surface coverage β as a function of the number of filaments per half-cycle N follows the same trend for all DBD configurations. This trend can be accounted for by assuming individual filaments cover an average area $<a_{filament}>$, with consecutive filaments overlapping, but forming as far away from each other as possible within the confines of the discharged area $A_{discharge}$.

126

Each filament in this model discharges the dielectric surface by the average charge/pulse <q> via the surface expansion mechanism discussed in the introduction. This process is fast and will occur within tens of nanoseconds, accounting for the periodic steep slopes observed in the *Q-V* diagrams and the high current pulses in Figure 5.6(a).

It should be emphasized that the 'staircase' shows some deviation from the slope ζ_{diel}, as can be seen in Figure 5.4(a), *i.e.* the charge/pulse *q* of an individual filament only corresponds approximately to a voltage step *dV* between filaments. There is, consequently, some stochastic component involved in the discharge dynamics. Similarly, a stochastic component can be inferred from the variations in charge/pulse *q* between filaments within the same discharge period, which lead, over many discharge cycles, to log-normal distributions of charge/pulse [153]. From cycle to cycle, however, the slope ζ_{diel} is always roughly similar, as seen *e.g.* in Figure 5.8(b), which shows that the stochastic behavior does not greatly affect the overall shape of the *Q-V* diagrams.

The data is consistent with the development of the surface charge as depicted in Figure 5.13, which is discussed step by step below. The discussion is aimed specifically at cathode-directed streamers, for which (net) negative charge is extracted from the dielectric.

(1) A filament will preferentially form at locations of increased charge density. Filament ignition will occur when the gap voltage equals the burning voltage U_b, which, with increasing external voltage, will occur first at the point of highest net negative charge density at the surface. These peak charges, referred to as 'memory charges' and indicated in green in Figure 5.13, are static on the time-scales of the DBD and remain immobile for at least longer than one half-cycle. While we have no direct measurement of memory charge in this work, only of the net average charge near the dielectric, it is included to account for the memory effect as well as the stochastic component of DBDs, *e.g.* differences in charge/pulse between filaments. Most of the net charge at the

surface can be considered laterally mobile, however, on time-scales of > 100 ns and is referred to as 'mobile charge', indicated in red in Figure 5.13. The possible physical origins of the memory and mobile charges are discussed at the end of this section. If there is a significant contribution of APTD to the negative half-cycle, the initial memory charge peak in this step may be absent, because APTD is expected to charge the dielectric surface uniformly.

(2) As the filament interacts with the surface and the surface expansion occurs, negative charge is locally extracted from the surface, which reduces the burning voltage U_b across the surface expansion region. Both the mobile negative charge and the memory charge are locally reduced, and the latter can become (partially) inverted, accounting for the memory effect during the next half-cycle. The amount of charge replacement for memory charges likely depends strongly on the dielectric material, *i.e.* the density of available trap states, but also on the plasma-surface interaction, *i.e.* the fluxes of species to the surface and their penetration into the surface.

(3) Between steps (1) and (3) only several tens of nanoseconds have passed. This time-scale is too short for the mobile charge to have redistributed significantly, due to its limited mobility. Redistribution of this charge mostly occurs after the filament is decaying. If charges are too mobile, the filament would not extinguish because the local gap voltage (burning voltage U_b) can be maintained until all mobile charge on the dielectric surface is removed, or until the external voltage begins to decrease.

(4) After a time > 100 ns, the mobile charges will again be distributed uniformly on the surface. The gap voltage will have been reduced over an area $> a_{filament}$.

The charge distribution before and after discharging in steps (1) and (4) in Figure 5.13 is consistent with the charge patterns measured directly by Bogaczyk *et al.* using a BSO crystal as dielectric in a He/N_2 DBD [135,150,154]. Their measurements show mostly flat charge distributions interspersed by Gaussian peaks at the locations of the filaments, where both the uniform charge and the Gaussian peaks
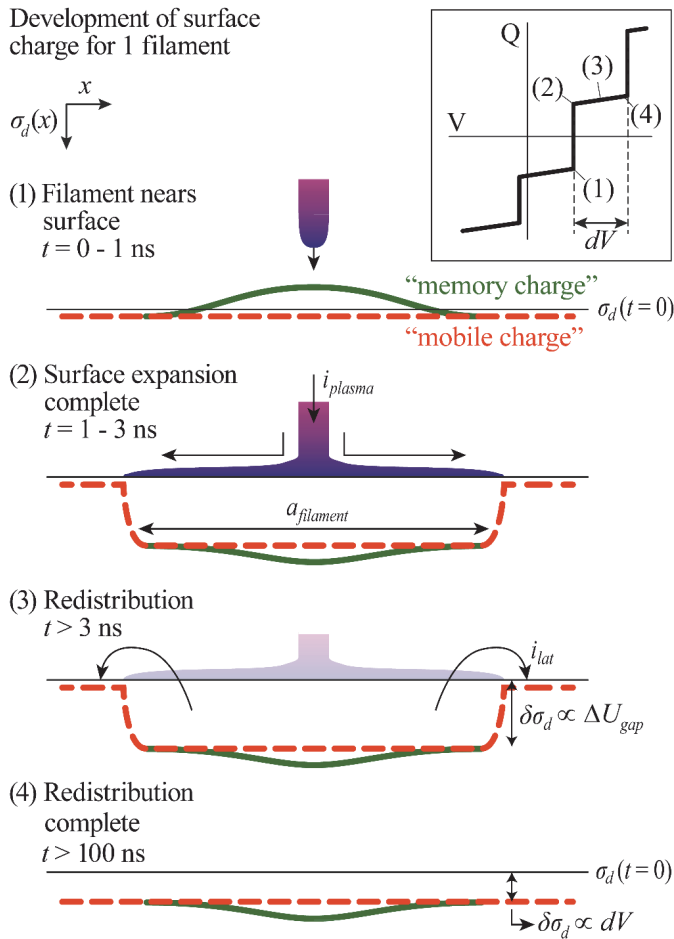
Figure 5.13: *Schematic development of the net surface charge density for a single filament. Negative charge is plotted in the positive vertical direction. There is an initial deposited charge density $\sigma_d \neq 0$ on the surface at $t = 0$, remaining after the previous filamentary discharge. The inset shows a segment of a Q-V diagram with the approximate occurrences of steps (1)-(4). If there is a significant contribution of APTD to the negative half-cycle, the initial memory charge peak in step (1) may be absent, because APTD is expected to charge the dielectric surface uniformly.*

become inverted after each half-cycle is completed. The Gaussian 'memory charges' have different amplitudes and widths for the positive and negative half-cycle and, therefore, depend on the direction of propagation of a filament.

The static memory charge peaks must be due to charges trapped in the top layers of the dielectric material during previous contact with a filament, in states at a low enough energy to become immobile. Using a steady-state model, Heinisch *et al.* show that for a dielectric with positive electron affinity, such as alumina with $\chi = 2.5$ eV [139], an Electron Surface Layer (ESL) will form from plasma-supplied electrons *below* the surface, which outweigh electrons trapped in image states above the surface by a factor of 10^7 [155]. Penetration of electrons into the material via a sub-surface ESL will lead to significant trapping in impurities or intrinsic deep trapping states within the material and give rise to the net negative, non-uniform 'memory charges' centered at the locations of filaments [155,156]. Trapping of electrons in alumina after exposure to DBD in air was investigated by Ambrico *et al.* using thermoluminescence data, where trap energies of $0.5 - 0.9$ eV below the conduction band minimum were found [157,158]. Positive charge, both mobile and immobile (if this distinction exists for positive charge), can result from extraction of electrons from the valence band of the dielectric through *e.g.* recombination with positive ions and capture by $N_2(A\ ^3\Sigma_u^+)$ metastables, explored by Heinisch and Bronold *et al.* in [156,159,160]. Note that the *net* deposited surface charge results from the sum of negative and positive deposited charges.

In the model of Heinisch *et al*, the electrons in the ESL are located in the conduction band of the alumina dielectric and may therefore result in mobile charge. Their model does not take into account the effect of electron trap sites below the conduction band, however, nor do they, as yet, model the time-dependent behavior for transient plasma. As stated by Heinisch and Bronold *et al.* in [156], the time-scales on which charges are trapped in a dielectric are directly related to the states in which they are trapped and both questions require further theoretical and experimental study. Akishev *et al*, on the other hand, suggest that the conductivity of residual plasma leads to redistribution of charge on the dielectric surface [117]. Both possibilities are discussed further in at a later stage.

5.6.2 Local gap voltage and extinction of a filament

To show there is quantitative agreement between the development of the surface charge as suggested by Figure 5.13, the burning voltage U_b observed in Q-V diagrams during discharging, and the average area coverage of a filament $\langle a_{filament} \rangle$, we investigate the extinction of single filaments. During step (2) in Figure 5.13, the filament removes a set charge $\langle q \rangle$ from the dielectric surface, resulting in an average drop in the local gap voltage ΔU_{gap}. This local drop in gap voltage must be sufficient to reduce the burning voltage U_b for recombination to overtake ionization processes in the filament channel. Similarly, ΔU_{gap} cannot exceed the burning voltage U_b, or the polarity of the voltage across the filament would reverse during discharging, which is non-physical. Below, the maximum area a single filament can discharge will be estimated from the assumption that $\Delta U_{gap} \leq U_b$. In this analysis the influence of memory charge is neglected.

The gap voltage averaged over the entire electrode area is given by:

$$U_{gap}(t) = \left(1 - C_{cell}^{ideal}\big/C_{diel}\right)\left(V(t) - \frac{Q_d(t)}{C_{diel}}\right),$$ (5.15)

which is the standard equation for gap voltage found in *e.g.* [72], but with the externally measured charge Q substituted by Equation (5.3). Given that the external voltage $V(t)$ is nearly constant during the short time frame of the filamentary discharge, and the change in Q_d is $\langle q \rangle$, we have for the *local* change in gap voltage ΔU_{gap}:

$$\Delta U_{gap} = \frac{\left(1 - C_{cell}^{ideal}\big/C_{diel}\right)\langle q \rangle}{\left(\langle a_{filament} \rangle\big/A_{\text{discharge}}\right)C_{diel}} \leq U_b \ ,$$ (5.16)

where the fractional area covered by a filament $\langle a_{filament} \rangle/A_{discharge}$ is a scaling factor for the dielectric capacitance C_{diel}, so that ΔU_{gap} is the local gap voltage drop, instead of the average gap voltage drop over the entire electrode area. Equation (5.16) allows for an estimation of the (minimum) ratio $\langle a_{filament} \rangle/A_{discharge}$ by considering the effect of discharging on the gap voltage, instead of determining it from
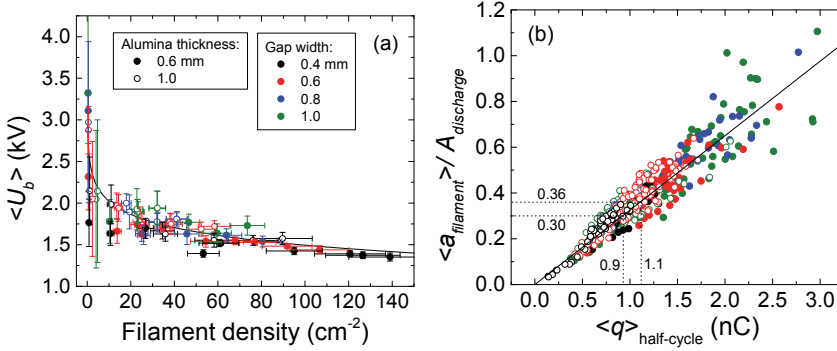
Figure 5.14: *(a) Average burning voltage $<U_b>$ over 4096 cycles as a function of filament density, (b) the fractional area $<a_{filament}>/A_{discharge}$ over which removal of a charge $<q>$ can lead to extinction of a filament, determined per half-cycle. The fractional area must be near or above the black solid line, or the drop in local gap voltage ΔU_{gap} would exceed the burning voltage U_b.*

effective dielectric capacitance ζ_{diel}, as was done in the previous section. An average burning voltage $<U_b>_{half-cycle}$ is determined per half-cycle via the method discussed in Chapter 2 and compared to the average charge/pulse per half-cycle $<q>_{half-cycle}$ [152,153]. Results for the average burning voltage over 4096 half-cycles are depicted in Figure 5.14(a), while the minimum ratio $<a_{filament}>/A_{discharge}$ for single half-cycles, calculated using Equation (5.16), is plotted in Figure 5.14(b). Because of a large variation in $<q>_{half-cycle}$ there is a wide range in $<a_{filament}>/A_{discharge}$ and it can be seen, for instance, that a single filament can cover the entire discharge area. More importantly, by comparing the average surface coverage over many cycles determined in Section 5.3 to the results of Figure 5.14(b), we find that for $<a_{filament}>/A_{discharge} = 0.30$ and 0.36 an average charge/pulse $<q> \approx$ 0.9 and 1.1 nC, respectively, is expected to extinguish a filament. This roughly corresponds to the average transferred charge/pulse determined in Chapter 4 and mentioned in Section 5.2, where $<q> = $ 0.7 - 0.8 nC for 1.0 mm alumina ($<a_{filament}>/A_{discharge} = 0.30$) and $<q>$ = 0.9 - 1.0 nC for 0.6 mm alumina ($<a_{filament}>/A_{discharge} = 0.36$) [153]. We conclude that step (2) in Figure 5.13 is consistent with observations from the data and that extinction of a filament can be accounted for by a local reduction of the gap voltage over an area corresponding to $<a_{filament}>/A_{discharge}$.

Equation (5.16), derived from a simplest equivalent circuit, assumes charging of the dielectric occurs uniformly over the area $<a_{filament}>$ and neglects the influence of non-uniform memory charge. The memory charge, as depicted in Figure 5.13, has a local maximum at the location of a filament column. As the filament reaches the cathode and this local maximum is reduced or inverted, the reduction in gap voltage ΔU_{gap} at the location of the filament column is greater than that of the surrounding area covered by the surface expansion. To determine the effect this would have on the radial extent of the surface expansion wave would require detailed modeling and is beyond the scope of this work.

5.6.3 Redistribution of charge between filament ignitions

The redistribution of charges between steps (3) and (4) in Figure 5.13 is inferred from (I) the existence of an average slope ζ_{diel} in the Q-V diagrams and (II) the reduction in the average external voltage increase between filaments $<dV>$ with an increasing number of filaments N. We will first argue why the data is inconsistent with the view that all charge on the surface is immobile, *i.e.* memory charge.

If all deposited surface charges remained immobile, the effect of a single average filament would be limited to an area $<a_{filament}>$. Consequently, suppression of the next filament could only occur if this area overlaps with the point of ignition of the previous filament. In Figure 5.12, it can be seen that this overlap does begin to occur, on average, for ≥ 5 filaments per half-cycle. Each filament could then suppress the ignition of 2 neighboring filaments, but $\sim N/3$ filaments could still ignite simultaneously.

Differences in memory charge could also never account for the step-by-step nature of the discharge, since an immobile surface charge distribution for N different points of ignition would then necessitate N different amplitudes, with precise increments, for a 'staircase' to develop. In other words, the first filament in a half-cycle would ignite at the point of highest peak memory charge, with the next filament igniting at the next highest peak memory charge, with the difference

in amplitude between two consecutive memory charge peaks corresponding to $<dV>$, etc. Such a precisely stepped charge distribution is highly unlikely to develop, especially considering that the memory charge deposited by each filament would have to anticipate the number of filaments in a cycle in order to conform to the inverse dependence of $<dV>$ on N.

Instead, redistribution of mobile surface charge provides a consistent framework. If an average single filament removes a charge $<q>$ at some point in the half-cycle, redistribution of charge from outside the area of influence $<a_{filament}>$ of that filament would (I) prevent filament ignition elsewhere in the gap because the gap voltage is also dropping outside this area of influence and (II) the reduction of surface charge density throughout the discharge area requires the external voltage V to increase by an amount corresponding to $<q>$ before the next filament can ignite. Comparing Equation (5.12) for the relation between $<q>$ and $<dV>$ to Equation (5.15) for the gap voltage $U_{gap}(t)$, we can state that redistribution of charge is consistent with the gap voltage over time if C_{diel} is scaled by the β factor. This can be made explicit by substituting Equation (5.3) into Equation (2.3) from Chapter 2, which after rearranging gives:

$$U_{gap}(t) = \left(1 - C_{cell}^{ideal} / C_{diel}\right)\left(V(t) - \frac{Q_d(t)}{\beta C_{diel}}\right). \qquad (5.17)$$

If a charge $Q_d = <q>$ is locally removed over an area $<a_{filament}>$, but is effectively removed over an area corresponding to β via redistribution, the external voltage V has to be increased by an amount $<dV>$ to return U_{gap} to its previous value before further filaments can ignite.

Redistribution of charge over an area corresponding to β is already implied by Equation (5.12), since the equivalent circuit model from which this equation is derived assumes the entire area corresponding to βC_{diel} is discharged uniformly and not locally. Since discharging is actually local, we arrive at the likelihood that charges must be redistributed after each filament for the alternative equivalent circuit model to be consistent with measurements. Equation (5.12) and the

alternative equivalent circuit do not provide the correct physical interpretation of C_{diel}, however. Since $<q>$ consists of both mobile charge and memory charge, $<q> = <q>_{mobile} + <q>_{memory}$, and only the mobile charge is redistributed, we rewrite Equation (5.12) to:

$$\frac{\langle q \rangle_{mobile} + \langle q \rangle_{memory}}{\langle dV \rangle} = \beta C_{diel} . \qquad (5.18)$$

Further realizing that only the mobile charge $<q>_{mobile}$ can affect the horizontal step size $<dV>$, we can also state that:

$$\frac{\langle q \rangle_{mobile}}{\langle dV \rangle} = \beta C_{diel}^{actual} , \qquad (5.19)$$

where βC_{diel}^{actual} is the contribution to the effective slope ζ_{diel} if there was only mobile charge and no memory charge. In other words, if all charge were mobile, the maximum attainable slope in Q-V diagrams would equal C_{diel}^{actual}. In reality, the presence of immobile memory charges increases the observed slope, through an average addition of $<q>_{memory}$ to each vertical step of the 'staircase', without affecting the horizontal step size $<dV>$. As was already depicted schematically in Figure 5.5, the capacitance C_{diel}^{actual} corresponds to an *actual* discharged area $A_{discharge}^{actual}$ that is smaller than the *apparent* discharged area $A_{discharge}$ as obtained from the equivalent circuit model. The coverage β on the other hand is an observable, defined by Equation (5.6) and described by Equation (5.14), and depends on the ratio $<a_{filament}>/A_{discharge}$, not on the absolute value of $A_{discharge}$. Equating Equations (5.18) and (5.19), an estimate of the deviation between *apparent* and *actual* discharged area can be given by comparing the values obtained for $A_{discharge}$ in Section 5.1 and assuming $A_{discharge}^{actual}$ equals the geometric electrode area of 7.1 mm^2. For 1.0 mm and 0.6 mm alumina we find that $C_{diel}^{actual} / C_{diel} = A_{discharge}^{actual} / A_{discharge}$ equals 0.7 and 0.8, respectively. Via Equation (5.18) and (5.19) this would correspond to a 70% to 80% contribution of mobile charge $<q>_{mobile}$ to the total transferred charge $<q>$.

The existence of a 'staircase' with an average slope ζ_{diel} implies that mobile charges are redistributed over an area $\beta A_{\text{discharge}}^{actual}$, which is the area covered by previous discharges. This suggests that the mobility of mobile deposited charges in the dielectric depends on recent contact with transient filaments, *i.e.* mobility is limited to a specific area. If mobile charge could redistribute over the entire electrode area, or beyond, <dV> would be independent of the number of filaments/cycle, contrary to observation. Note also that for higher charge/pulse, when q is greater than <q>, dV is also greater than <dV> and vice-versa, consistent with the 'staircase', although the details will depend on the relative contributions of mobile and memory charges to the total transferred charge.

To estimate the lateral current over the surface i_{lat}, involved with filling the 'hole' left behind in the surface charge density by a filament, such as depicted in step (3) of Figure 5.13, the time between filaments is estimated from the maximum rate of change of the external voltage:

$$\Delta t = \langle dV \rangle \Big/ \frac{\partial V(t)}{\partial t} \geq \frac{\langle q \rangle}{\beta C_{diel}} \Big/ 2\pi f V_p , \qquad (5.20)$$

with f and V_p the frequency and amplitude of the external voltage, respectively and the inequality is based on Equation (5.12) for <dV>, *i.e.* the average time between filaments must be equal to, or greater than <dV> divided by the maximum rate of change of the external voltage V. Taking <q> ≈ 1 nC, βC_{diel} ≈ 1 pF, f = 100 kHz and V_p = 5 kV, gives $\Delta t \geq 0.3$ μs. Following Equation (5.16), the 'hole' in the surface charge can be represented by a capacitor:

$$C_{hole} = \frac{\left(\langle a_{filament} \rangle \big/ A_{\text{discharge}} \right)}{\left(1 - C_{cell}^{ideal} \big/ C_{diel} \right)} C_{diel} \qquad (5.21)$$

which can be used to define the RC-time, τ, via

$$\tau = R_{lat} C_{hole} \ , \tag{5.22}$$

with R_{lat} the lateral impedance of the surface charge with respect to the 'hole'. With $\Delta t = \tau \geq 0.3$ µs, $<a_{filament}>/A_{discharge} \approx 0.3$ and $C_{cell}^{ideal}/C_{diel} \approx 0.1$, it is found that $R_{lat} \geq 1$ MΩ. Note that we use C_{diel} in our calculations, instead of C_{diel}^{actual}, since we do not know the exact value of the latter. The average lateral current i_{lat} can be estimated via:

$$i_{lat} = \frac{\langle q \rangle}{\tau} = \frac{\langle q \rangle}{R_{lat} C_{hole}} \leq 3 \text{ mA}. \tag{5.23}$$

This lateral current cannot be observed in the external circuit, but it is significantly lower than the (peak) plasma current for filaments, as seen in Figure 5.6(a). This means that the lateral current can never be high enough to maintain a single filamentary discharge, again consistent with Figure 5.13. The mobility of the charge on the surface is sufficient to provide redistribution of charge *between* filament ignitions, but insufficient to allow a single filament to discharge the entire surface. The lateral impedance $R_{lat} \geq 1$ MΩ matches with calculations by Akishev *et al*, who take several 100 MΩ resistors in parallel to represent residual surface conductivity in their single filament model [117]. In an electrical equivalent circuit model for DBDs at 50 Hz proposed by Tay *et al*, a surface impedance of 1.0 to 4.5 MΩ between filaments is used to reproduce experimental *Q-V* diagrams [161].

Using the estimates made above, we can speculate on the nature of the mobile charge. Assuming an annulus-shaped conductor of thickness δ with an inner radius of $r_{filament} \approx 1$ mm and an outer radius of $R_{electrode} = 1.5$ mm we have:

$$R_{lat} \approx \frac{\rho_{lat}}{2\pi\delta} \ln \left| \frac{R_{electrode}}{r_{filament}} \right| \approx 0.06 \frac{\rho_{lat}}{\delta} \ . \tag{5.24}$$

If the lateral current flows in a sub-surface ESL with a penetration depth $\delta \leq 10^{-2}$ cm, or through residually conductive plasma above the

surface with a similar spatial extent, an impedance of 1 MΩ corresponds to $\rho_{lat} < 2 \cdot 10^5$ Ωcm.

As suggested by Akishev *et al.* in [117], the conductivity of residual plasma could play a role in the redistribution of charge on the dielectric surface. During steady-state operation and between filament ignitions, residual plasma with charge densities around 10^{11} cm^{-3} may still be present in the gap [162]. As discussed in the Appendix, Section A5.1, the residual plasma will contain an electron density << 10^9 cm^{-3} and is therefore mostly composed of positive and negative ions. With mobilities $\mu_{ion}^{+/-}$ on the order of 2 cm^2/Vs, [163–165], the expected resistivity of the residual plasma is on the order of $\rho \approx 10^7$ Ωcm; too low for the mobile charge. Though the gas-phase electron mobility $\mu_e = 600$ cm^2/Vs [166], the electron density near the surface must be at least 10^{10} cm^{-3} to obtain the required resistivity, which would quickly be lost to attachment or be absorbed by the dielectric [155].

If, instead, the sub-surface ESL is responsible for the mobile charge, and its effect is similar to doping or electron irradiation, we find in [167] that Cr^{3+}-doped alumina has a *bulk* resistivity of ~ 10^{11} Ωcm at temperatures of 400 K, while even heavily electron-irradiated alumina (at an electron flux of 10^{14} cm^{-2}s^{-1} with a mean energy of 1 MeV) heated to 700 K does not have a bulk resistivity below ~ 10^7 Ωcm. Ca^{2+}-doped alumina does have a bulk resistivity of < 10^5 Ωcm at temperatures ≥ 1000 K, though in this case the dominant charge carriers are identified as protons originating from hydrogen impurities [168]. Assuming electrons are the dominant charge carriers for undoped alumina exposed to plasma, we can estimate the mobility μ_e of mobile electrons in the area affected by filaments using:

$$\rho_{lat} \approx \frac{1}{e\mu_e n_e} = \frac{\delta}{e\mu_e \sigma_e} \ , \tag{5.25}$$

where the electron density n_e in the ESL is converted to a surface density $\sigma_e = n_e \delta$ and e is the electron charge. Substituting Equation (5.25) in (5.24) and solving for μ_e we obtain:

$$\mu_e \approx \frac{0.06}{eR_{lat}\sigma_e} \ . \tag{5.26}$$

The maximum negative charge density at the dielectric is - 60 nC/cm^2, corresponding to $\sigma_e \geq 4 \cdot 10^{11}$ electrons/cm^2. The value of σ_e may be greater, because we only observe the *net* charge density and part of the sub-surface electron density may be offset by positive charges, such as holes in the valence band. With $R_{lat} \geq 1$ MΩ we obtain $\mu_e \leq 1$ cm^2/Vs. For comparison, in Ca^{2+}-doped alumina at 1000 K, the charge-carrying protons have a density $n_p \approx 10^9$ cm^{-3} and a mobility $\mu_p \approx 10^{-3}$ cm^2/Vs [168]. For undoped alumina at 290 K, the electron is the dominant charge carrier with a density $n_e \approx 10^7$ cm^{-3} and a mobility $\mu_e \approx 3$ cm^2/Vs, increasing to $\mu_e \approx 16$ cm^2/Vs at 450 K [169]. While these *bulk* electron mobilities are already higher than those expected for mobile charge, they may not reflect the conditions applicable to the dielectric surface during and within a few microseconds after plasma exposure. For instance, the bulk values may only be applicable at very low carrier densities. Similarly, the dielectric exposed to plasma may have a high positive charge density in conjunction with a high electron density, because holes in the valence band are continuously created by impinging metastables [156,159,160]. The effect that this may have on surface charge transport is as yet unexplored, though our results suggest that the conductive behavior will be significantly different than that in the bulk of doped or undoped dielectrics. Note, however, that any changes to the surface are reversible within seconds, since no hysteresis was observed in the *Q*-V diagrams when lowering the applied voltage amplitude. Because of this, we discount the possibility that *e.g.* a thin carbon layer containing the mobile charge is locally deposited under plasma exposure.

5.6.4 Memory charge: estimates of charge non-uniformity

While the contribution of mobile charges to the electrical dynamics was discussed in the previous sections, the stochastic effect of memory charge has, so far, not been treated. In this section, the local variation in surface charge is estimated from the external voltages at which individual filaments ignite. Essentially, the stochastic deviations of the 'staircase' from the ideal slope, ζ_{diel} in Figure 5.4(a), can be expressed in terms of variations of the surface charge density. Since we lack a detailed electrical model of the discrete filamentary discharge, we are limited to the simple equivalent circuit model which assumes a maximum average slope C_{diel} with corresponding area $A_{discharge}$ and a *uniform* deposited charge distribution. We determine the average deposited surface charge density $\sigma_{d,average}$ in this model by rewriting Equation (5.3):

$$Q(t) = C_{cell}V(t) + \left(1 - \frac{C_{cell}^{ideal}}{C_{diel}}\right)\beta A_{\text{discharge}}\sigma_{d,average}(t). \quad (5.27)$$

If the surface charge density is locally higher than average, filaments will preferentially form at these locations due to local field enhancement in the gap. The local variation in surface charge is estimated from the external voltages at which individual filaments ignite. Using Equation (5.4) as a starting point, the deposited surface charge density at which discharging is expected to occur, $\sigma_{d,expected}$, can be calculated. To do this, it is assumed that a filament will form whenever the local gap voltage U_{gap} is equivalent to the average burning voltage per half-cycle $<U_b>_{half-cycle}$, as was done for Figure 5.13(b). Using this average $<U_b>_{half-cycle}$ we can calculate $\sigma_{d,expected}$ for individual filaments igniting at a given external voltage V_{on}, where any variation in $\sigma_{d,expected}$ from filament to filament is now an indicator of the non-uniformity of the surface charge density. With the derivation given in the Appendix, the equation for $\sigma_{d,expected}$ is:
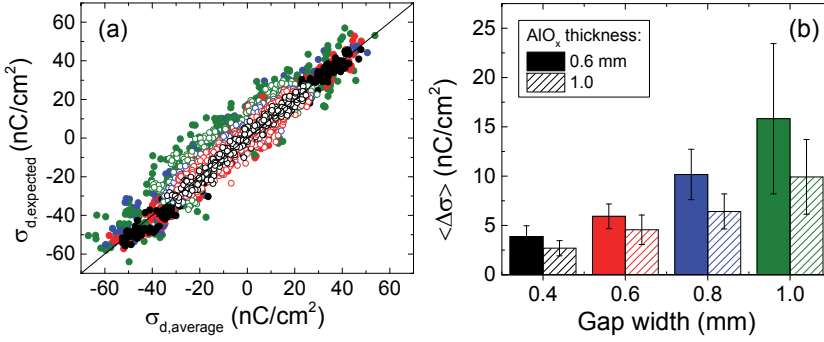
Figure 5.15: *(a) The expected deposited surface charge density on the dielectric surface versus the average deposited surface charge density for all positive half-cycle filaments and all 8 DBD configurations at different voltage amplitudes. Each data point represents a single filament. Color coding and symbols are the same as in Figure 5.14(a). (b) The average of the deviation Δσ between $\sigma_{d,expected}$ and $\sigma_{d,average}$ for each DBD configuration.*

$$\sigma_{\text{d,expected}} = \frac{\varepsilon_0 \varepsilon_r}{d_{diel}} \left(V_{on} - \frac{1}{1 - C_{cell}^{ideal}/C_{diel}} \langle U_b \rangle_{half-cycle} \right), \qquad (5.28)$$

where V_{on} is the external voltage at which a filament ignites during a half-cycle, as indicated for two filaments in Figure 5.4(a), at the beginning of this chapter. Since we employ a model which assumes the surface charge distribution is uniform, $\sigma_{d,expected}$ is an apparent surface charge density. Though this is a very crude model, it allows for comparison of the deviations between measured 'staircases' and ideal 'staircases' (where q is always exactly proportional to dV) for the complete range of DBD geometries and applied voltage amplitudes.

Results of $\sigma_{d,expected}$ are plotted as a function of $\sigma_{d,average}$ for individual filaments in Figure 5.15(a), while the average of the deviation $\Delta\sigma = |\sigma_{d,expected} - \sigma_{d,average}|$ is plotted in Figure 5.15(b) for each DBD configuration. The deviation $\Delta\sigma$ does not depend strongly on the number of filaments per half-cycle, hence the average is taken over all applied voltage amplitudes per DBD configuration. From Figure 5.15(a) we can conclude that the deviations of $\sigma_{d,expected}$ with respect to

141

Development of surface charge for 3 filaments (µs timescale)
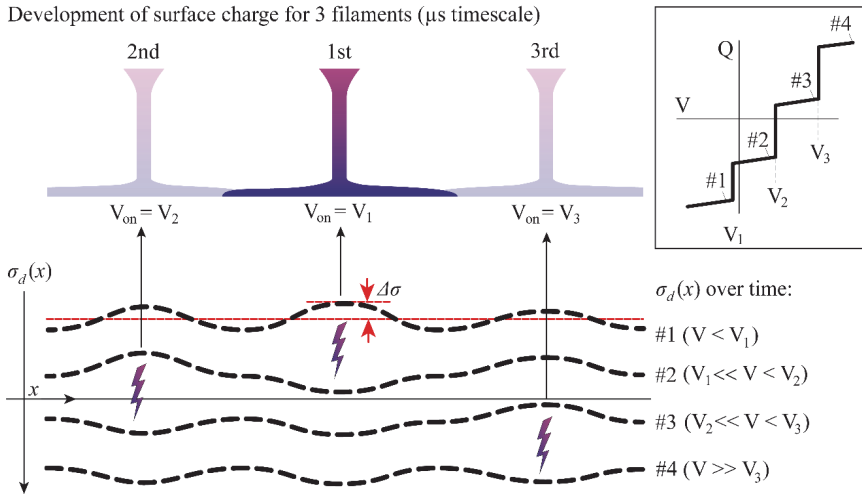
Figure 5.16: *Development of the deposited surface charge density σ_d as a function of position x, at four different instances (#1-4) during the positive half-cycle, indicated in the Q-V diagram in the upper right-hand-side. Each dashed line represents σ_d after redistribution from a preceding filament has been completed. For #1 the deviation $\Delta\sigma$ between $\sigma_{d,expected}$ and $\sigma_{d,average}$ is indicated. Negative charge is plotted in the positive vertical direction.*

$\sigma_{d,average}$ are in equal measure above or below the $\sigma_{d,expected} = \sigma_{d,average}$ line. The *apparent* non-uniformity of surface charge is between 3 and 15 nC/cm^2 for average surface charge densities between $\pm$ 30 and $\pm$ 60 nC/cm^2. In Figures 5.15(a,b) it can be seen that the deviations are larger for greater gap widths and slightly larger for thinner alumina, showing that the deviations from an ideal 'staircase' are highest for larger gaps and thinner dielectrics. This is consistent with the results of Chapter 4, where larger gap widths and thinner dielectrics are shown to lead to significantly higher average charge/pulse with broader distributions. With $\langle\Delta\sigma\rangle$ a measure of the surface charge non-uniformity, and this non-uniformity attributed to memory charge, it appears that the memory charge gives rise to variations in the charge/pulse of filaments. The proportion of memory charge to mobile charge cannot be determined from $\langle\Delta\sigma\rangle$, however, and this value should be treated as a relative measure of non-uniformity. Comparing the variation of $\langle\Delta\sigma\rangle$ with DBD configuration to the

results for $\langle a_{filament}\rangle$ depicted in Figure 5.14, the latter predicts larger $\langle a_{filament}\rangle$ for higher $\langle q\rangle$, which has here been related to higher $\langle\Delta\sigma\rangle$.

The overall surface charge development discussed in the previous sections can be summarized by Figure 5.16. The 1st filament occurs at the point of highest memory charge and after this filament has occurred, the average charge density over the entire region has been lowered via redistribution of the mobile surface charge, so that the 2nd filament will require a significantly higher external voltage to ignite, i.e. $V_2 \gg V_1$ in Figure 5.16. If no redistribution of surface charge takes place after the 1st filament, the charge density σ_d at the locations of the 2nd and 3rd filament remain largely unaffected due to the limited spatial extent of the 1st filament. This would then provide a large enough gap voltage for the 2nd and 3rd filament to ignite soon after, or simultaneously with, the 1st filament, i.e. $V_1 \approx V_2 \approx V_3$. Memory charges give rise to earlier ignition than expected from the average surface charge density and provide a stochastic element to the development of the 'staircase'.

5.7. Summary & conclusions

Discharges in the gap interact with the dielectric surface, depositing or removing charges. The total charge state of the surface can be determined via a measurement capacitor in series with the DBD. By measuring *Q-V* diagrams in this way for a DBD with a total discharge area not much greater than the area discharged by a single filament, the electrical dynamics of multi-filament discharges can be investigated.

In the *Q-V* diagrams, individual filaments appear as discrete steps on the *Q*-axis, which appear one after the other, with well-defined steps on the *V*-axis. The average slope in *Q/V* diagrams during discharging, ζ_{diel}, depends on the average surface coverage β of the discharge, which in turn is a function of the number of filaments *N* occurring in the half-cycle. This effective dielectric capacitance ζ_{diel} as a function of β can be described by combining Equation (5.5) with Equations (5.18) and (5.19):

$$\zeta_{diel}(\beta) = (1-\beta)C_{cell}^{ideal} + \beta C_{diel}^{actual}\left(1 + \frac{\langle q \rangle_{memory}}{\langle q \rangle_{mobile}}\right), \qquad (5.28)$$

where we neglect the parasitic capacitance C_{cell}^{par} in order to describe our results in the most general terms. The capacitance C_{cell}^{ideal} is then the measured slope in the *Q-V* diagram when there is no discharging, $<q>_{memory}$ and $<q>_{mobile}$ are the memory and mobile portions of the average conductively transferred charge of a filament, respectively, and C_{diel}^{actual} the actual capacitance of the dielectric area exposed to discharges during a half-cycle. The maximum attainable slope in *Q-V* diagrams, referred to as C_{diel}, can be greater than C_{diel}^{actual} due to the presence of immobile memory charges on the dielectric surface. We have estimated that the observed slope can be 20 to 30% higher than the capacitance of the discharged dielectric area C_{diel}^{actual}, though the exact difference will require further study.

In the standard equivalent circuit for DBDs uniform charging or discharging of the dielectric is implicitly assumed. Since this description is consistent with the discharge behavior for many spatially separated, discrete filaments, the existence of mobile charge on or near the dielectric surface is proposed, which can redistribute over the surface on time scales of 100's of nanoseconds. Only via redistribution of mobile surface charge from elsewhere on the surface to the local region affected by an individual filament can ignition of the next filament in a different location be suppressed until the external voltage has increased by *<dV>*. Furthermore, the parameters *<q>* and *<dV>* in this model are consistent with the data if the mobile charge is limited to the fractional area of the dielectric exposed to discharges *β*. The mobile charge, carried by electrons, has an estimated mobility $\mu_e \leq 1$ cm^2/Vs. It is hypothesized that the mobility of charge in the dielectric depends on recent contact with transient filaments. This mechanism leads to a constant burning voltage U_b throughout a discharge half-cycle. The fundamentals of charge transfer during transient plasma exposure and the subsequent behavior of these charges within the dielectric surface are a relatively

unexplored subject, but our results already suggest that the behavior of charge carriers (at high densities near the surface) is different from those in doped or undoped dielectrics (at low densities in the bulk).

Not all charge on the surface is mobile, or discharging would be entirely random in space across the surface and no memory effect would exist, nor can variations in the transferred charge/pulse between filaments be accounted for. Filaments also locally deposit immobile charge, likely in deep trap states within the dielectric material, which is referred to as 'memory charge'. From variations in the moment of ignition of individual filaments with respect to the average surface charge density, the non-uniformity of the surface charge density is estimated. This non-uniformity is a direct result of the memory charge. The degree of non-uniformity is shown to depend on gap width and dielectric thickness, in agreement with the charge/filament distribution measurements of Chapter 4.

In Chapter 4, it was observed that, even for the small area DBD used in this work, 2 filaments can occur within 30 ns, leading to overlapping current pulses. It was also observed that this had little effect on the charge distributions, *i.e.* it did not lead to an increase at the high end of the charge/pulse distribution even though 2 filaments were counted as one. The model presented here can also account for this. If 2 filaments occur in close succession, their surface expansion waves will overlap and the total charge extracted by both filaments will be lower than when they occur more separated in time, because they accelerate each other's extinction.

Time-dependent measurements of the surface charge distribution, such as performed by Bogaczyk *et al.* using a BSO crystal as dielectric [135], could be used to verify the model described here. The data in [135] does not contradict the conclusions drawn here, though their measurements are limited to low filament densities of ~ 20/cycle/cm^2, possibly making the mobile charge density relatively low compared to the memory charge density. A much simpler experiment would be to split the small electrode area used here, into 2 even smaller electrodes with separate dielectrics. If mobile charge cannot be shared between these electrodes, the Q/V slope during

discharging should increase up to twice as fast as a function of applied voltage amplitude, since two filaments with equal charge/pulse can then occur simultaneously without interfering with each other. Using well-defined electrode areas, where the dielectric does not extend beyond the bottom electrode as it does here, the actual discharge area $A_{\text{discharge}}^{actual}$ can also be compared to the effective discharge area $A_{discharge}$ as it appears from the Q-V diagrams. Another relatively simple approach to obtain $A_{\text{discharge}}^{actual}$ would be to coat the dielectric surface with an electrostatic powder, such as toner, after exposure to the DBD.

Appendix to Chapter 5

A5.1 Charge Q_d from measurement capacitor C_{meas}

Following is the derivation of Equation (5.3) based on the equivalent circuit depicted on the right-hand-side of Figure 5.3 in the main text. We will also discuss the effect of residual volume charges in the gap on the *Q-V* diagrams.

Considering the small dimensions of the DBD, as depicted on the left-hand-side of Figure 5.3, the effect of parasitic capacitance between the primary and secondary electrodes must also be considered. Parasitic capacitance is defined here as any region where polarization is induced by the external voltage, but where no discharging takes place. This parasitic capacitance is included as C_{cell}^{par} in the equivalent circuit diagram on the right-hand-side of Figure 5.3, where all other variables are also indicated. The parallel component C_{cell}^{par} is the only parasitic capacitance that needs to be considered, as it is the only component that can affect the charge measurement Q on the measurement capacitance C_{meas} and represents the region through air, alumina and Teflon ring outside the discharging area. The equivalent circuit assumes all components C_{gap}, C_{diel} and C_{cell}^{par} are charged uniformly.

The capacitances in the region of discharge, C_{gap} and C_{diel} are taken to be ideal plate-capacitors following

$$C_{gap} = \frac{\varepsilon_0 A_{discharge}}{d_{gap}} \text{ and} \tag{A5.1}$$

$$C_{diel} = \frac{\varepsilon_0 \varepsilon_r A_{discharge}}{d_{diel}}, \tag{A5.2}$$

where $A_{discharge}$, d_{gap} and d_{diel} are the maximum discharge area, gap width and alumina thickness, respectively.

During the discharge of a filament, the effect of volume charges in the gas gap is minimal, as the conducting region will be quasi-neutral, with net charge limited to the electrode surfaces, i.e. in the cathode fall region. The same is expected to hold between discharges. For a quasi-neutral volume plasma, the electric fields will be constant, the same as for an empty gap. At atmospheric pressure there is fast equilibration of the electron temperature T_e with the surrounding gas on nanosecond time-scales, leading to $T_e < 500$ K. The residual volume charge density cannot be much higher than 10^{11} cm^{-3} and is mostly composed of negative and positive ions due to attachment processes [117,162]. The low charge density of 10^{11} cm^{-3} at low temperature leads to Debeye lengths of 5 µm. The sheath thickness of the residual, electro-negative plasma will be on the order of 10 Debeye lengths, or 50 µm [170]. The voltage drop over the sheath will be on the order of $10 - 100$ V, which is low compared to the total voltage drop in the gap U_b [170]. The residual plasma is, therefore, expected to be quasi-neutral over most of the gap width and can be treated as a resistor $R_{residual}$ in parallel with the gap capacitance C_{gap}. At best, the presence of residual volume charge will lead to low leak currents through the gap, but these will be orders of magnitude lower than the plasma current through a filament. This is based on the observation that the Q-V diagrams show, to a good approximation, purely capacitive behavior between filamentary current pulses. This allows us to estimate the impedance of the residual volume plasma $R_{residual}$, because the impedance of the gap capacitance C_{gap} must be significantly lower than $R_{residual}$ to guarantee capacitive behavior:

$$R_{residual} \gg \left| \frac{1}{i\omega C_{gap}} \right|, \tag{A5.3}$$

where $\omega = 2\pi f = 2\pi \cdot 100$ kHz. With an electron mobility $\mu_e \approx 600$ cm^2/Vs [166] versus mobilities for positive and negative ions $\mu_{ion}^{+/-} \approx 2$ cm^2/Vs [163–165], we can assume electrons determine the conductivity, so that we can write:

$$R_{residual} = \rho_{residual} \frac{d_{gap}}{A_{\text{discharge}}} = \frac{1}{e\mu_e n_e} \frac{d_{gap}}{A_{\text{discharge}}}, \tag{A5.4}$$

with $\rho_{residual}$ the resistivity of the residual plasma, e the electron charge and n_e the electron density. Substituting Equations (A5.4) and (A5.1) in (A.5.3) and solving for n_e we find:

$$n_e \ll \frac{\varepsilon_0 2\pi f}{e\mu_e} = 10^9 \, \text{cm}^{-3} \,. \qquad (A5.5)$$

This result indicates that the electron density of the residual volume plasma must be very low compared to the expected ion density of 10^{11} cm^{-3}. Performing the same calculation for the positive and negative ions, with $\mu_{ion}^{+/-} \approx 2$ cm^2/Vs also confirms that the residual ion density cannot be greater than 10^{11} cm^{-3}.

The parasitic capacitance C_{cell}^{par} can be related to the total cell capacitance C_{cell}, determined via the measurement capacitor, using:

$$C_{cell} = C_{cell}^{par} + \left(C_{gap}^{-1} + C_{diel}^{-1} \right)^{-1} = C_{cell}^{par} + C_{cell}^{ideal} \,, \qquad (A5.6)$$

with C_{cell}^{ideal} the cell capacitance of the discharging region.

To derive the relationship between charge measured on the measurement capacitor C_{meas} and the deposited surface charge Q_d, the starting point is Gauss's law for the interface between discharge gap and dielectric:

$$\oiint_{A_{discharge}} \vec{D} \cdot d\vec{A} = A_{discharge} \left(\varepsilon_0 E_{gap} - \varepsilon_0 \varepsilon_r E_{diel} \right) = -Q_d \,, \qquad (A5.7)$$

where E_{gap} and E_{diel} are the electric fields perpendicular to the surface, as indicated in Figure 5.3, and deposited surface charge Q_d is identified as the *free* surface charge Q_f commonly associated with *D*-fields. The sign convention in Equation (A5.7) is chosen such that a *positive* field (and voltage *drop*) are downward in Figure 5.3 if the net

deposited surface charge is *negative.* Expressing the electric fields in terms of their respective voltage drops, we get:

$$\varepsilon_0 A_{discharge} \frac{U_{gap}}{d_{gap}} - \varepsilon_0 \varepsilon_r A_{discharge} \frac{U_{diel}}{d_{diel}} = -Q_d \,, \qquad (A5.8)$$

Which, by substitution of Equations (A5.1) and (A5.2) gives:

$$C_{gap} U_{gap} - C_{diel} U_{diel} = -Q_d \,. \qquad (A5.9)$$

There will also be charge on the interface between discharge gap and metal electrode, induced by the field in the gap E_{gap}. This charge does not need to be considered in the derivation, as it is simply a result of the external voltage and deposited charge on the dielectric and, therefore, not a contributing factor to the deposited charge.

Similar to Equation (A5.9), the 'interface' between dielectric, parasitic capacitor and measurement capacitor contains no free charge, hence:

$$C_{meas} V_{meas} - C_{diel} U_{diel} - C_{cell}^{par} \left(V - V_{meas} \right) = 0 \,, \qquad (A5.10)$$

which is simply Kirchhoff's law for two parallel capacitors, C_{diel} and C_{cell}^{par}, in series with a third capacitor, C_{meas}. With a final equation, stating that the total voltage drop across discharge gap, dielectric and measurement capacitor should add up to the external voltage:

$$U_{gap} + U_{diel} + V_{meas} = V \,, \qquad (A5.11)$$

We can substitute (A5.11) in (A5.9) and collect U_{diel},

$$C_{gap} \left(V - V_{meas} \right) - \left(C_{gap} + C_{diel} \right) U_{diel} = -Q_d \,, \qquad (A5.12)$$

and substituting (A5.10) in (A5.12), we get:

$$C_{gap}\left(V - V_{meas}\right)$$
$$-\left(C_{gap} + C_{diel}\right)\frac{C_{meas}V_{meas} - C_{cell}^{par}\left(V - V_{meas}\right)}{C_{diel}} = -Q_d. \quad \text{(A5.13)}$$

Solving (A5.13) for V_{meas} gives

$$V_{meas} = \frac{C_{cell}^{par}\left(C_{diel} + C_{gap}\right) + C_{diel}C_{gap}}{C_{diel}C_{gap} + \left(C_{meas} + C_{cell}^{par}\right)\left(C_{diel} + C_{gap}\right)}V$$
$$+ \frac{C_{diel}}{C_{diel}C_{gap} + \left(C_{meas} + C_{cell}^{par}\right)\left(C_{diel} + C_{gap}\right)}Q_d. \quad \text{(A5.14)}$$

With $C_{meas} \gg C_{cell}^{par}, C_{gap}, C_{diel}$, it can be shown that (A5.14) simplifies to:

$$C_{meas}V_{meas} = \left(C_{cell}^{par} + \frac{C_{diel}C_{gap}}{\left(C_{diel} + C_{gap}\right)}\right)V + \frac{C_{diel}}{\left(C_{diel} + C_{gap}\right)}Q_d. \quad \text{(A5.15)}$$

Since C_{gap} and C_{diel} in series is equivalent to C_{cell}^{ideal}, (A5.15) becomes:

$$Q = C_{meas}V_{meas} = \left(C_{cell}^{par} + C_{cell}^{ideal}\right)V + \left(1 - \frac{C_{cell}^{ideal}}{C_{diel}}\right)Q_d, \quad \text{(A5.16)}$$

which is the same as Equation (5.3) in the main text.

A5.2 Procedure for determining parasitic capacitance

In this section the procedure to obtain C_{cell}^{par} from measured data is described, assuming the discharging region of the DBD, consisting of C_{diel} and C_{gap}, is an ideal plate-capacitor.

The capacitance ζ_{diel} is the slope during discharging of the as-measured Q-V diagram and must be corrected by the capacitance C_{cell}^{par}. The effective dielectric capacitance after correction ζ_{diel}', is [70]:

$$\zeta_{diel}' = \zeta_{diel} - C_{cell}^{par}. \tag{A5.17}$$

It is demonstrated by Figure 5.9 in the main text that the capacitance ζ_{diel} will reach a saturation value at sufficiently high applied voltage, which implies that the saturation value of ζ_{diel}' can be identified as the *apparent* dielectric capacitance C_{diel} of the discharging region:

$$C_{diel} = \zeta_{diel}^{sat} - C_{cell}^{par}. \tag{A5.18}$$

Combining Equation (A5.18) with Equations (A5.1), (A5.2) and (A5.3) for C_{gap}, C_{diel} and the measured cell capacitance C_{cell}, respectively, it can be found that:

$$C_{cell}^{par} = \left(\frac{d_{diel}}{\varepsilon_r d_{gap}} + 1 \right) C_{cell} - \frac{d_{diel}}{\varepsilon_r d_{gap}} \zeta_{diel}^{sat}. \tag{A5.19}$$

Equation (A5.19) allows for the calculation of C_{cell}^{par} for each DBD configuration from the measured quantities C_{cell} and ζ_{diel}^{sat}.

A5.3 Expected deposited surface charge

To calculate the expected deposited surface charge density $\sigma_{d,expected}$ for breakdown at an external voltage V_{on} from the ideal capacitors C_{gap} and C_{diel} (see Figure 5.3 of the main text), a slight modification is made to Equation (A5.9):

$$C_{gap}U_{gap} - C_{diel}U_{diel} = -\sigma_d A_{\text{discharge}}. \tag{A5.20}$$

Using the following identities:

$$\sigma_d = \sigma_{d,expected} \quad , \tag{A5.21}$$

$$U_{gap} = U_b, \tag{A5.22}$$

$$V_{on} = U_{gap} + U_{diel}, \tag{A5.23}$$

and substituting them in Equation (A5.20) gives:

$$
\begin{aligned}
-\sigma_{d,expected} A_{discharge} &= C_{gap} U_{gap} - C_{diel} U_{diel} \\
&= C_{gap} U_b - C_{diel} \left(V_{on} - U_b \right) \\
&= \left(C_{gap} + C_{diel} \right) U_b - C_{diel} V_{on} \\
&= -C_{diel} \left(V_{on} - \frac{C_{gap} + C_{diel}}{C_{diel}} U_b \right).
\end{aligned}
\tag{A5.24}
$$

Further substituting Equation (A5.2) and

$$C_{cell}^{ideal} = \left(C_{gap}^{-1} + C_{diel}^{-1} \right)^{-1}, \tag{A5.25}$$

leads to:

$$\sigma_{d,expected} = \frac{\varepsilon_0 \varepsilon_r}{d_{diel}} \left(V_{on} - \frac{1}{1 - C_{cell}^{ideal}/C_{diel}} \langle U_b \rangle_{half-cycle} \right), \tag{A5.26}$$

which is equivalent to Equation (5.28) in the main text, after substitution of $U_b = \langle U_b \rangle_{half-cycle}$.

Outlook

In this thesis, we have used straightforward electrical models for the DBD to obtain basic characteristics of the discharge, the foremost being the burning voltage U_b. The alternative equivalent circuit for partial surface discharging, presented in Chapter 2, has proved invaluable to obtain the burning voltage accurately. In Chapter 3 it was shown that the efficiency of radical production conforms to this model, as both burning voltage and the energy per N atom produced remains unchanged with increasing applied voltage amplitude. A more in-depth analysis of the characteristics of individual filaments in Chapter 4 revealed how only the number density of filaments increases with increasing applied voltage, while the average charge transferred per filament remains virtually unchanged. This formed the basis for the analysis presented in Chapter 5, where the equivalent circuit is reinterpreted to consistently account for multiple-filament interactions.

As discussed in the conclusions of Chapter 5, splitting the electrode into two smaller electrodes with half the area can be used to verify the proposed model for multiple-filament interactions. If mobile charge cannot be shared between the two electrodes, the Q/V slope during discharging should increase up to twice as fast as a function of applied voltage amplitude compared to the single larger electrode, since two filaments can occur simultaneously without interfering with each other. The results can serve as indirect proof that not only local charging of the dielectric (via memory charges) is relevant to the discharge dynamics. Such a setup, with one 14 mm^2 electrode and two 7 mm^2 electrodes, has been built and will be used to perform these experiments, see Figure O.1.

The setup is also equipped with a glass bell-jar, allowing for experiments to be performed in controlled environments using a wide range of process gases. Similar to the setup used in Chapter 4 and Chapter 5, gap widths and dielectric materials are easily altered. Combining charge/pulse and Q-V analysis in a controlled environment allows for more rigorous measurements of filament number density, average charge/pulse and slope ζ_{diel}. A separate goal
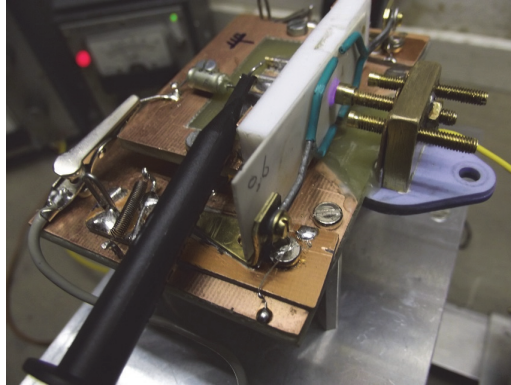
Figure O.1: *The setup with planar DBDs of 1 x 14 mm^2 and 2 x 7 mm^2 for experiments in a controlled environment. The bell-jar is not depicted.*

is to explore the effect of different dielectric materials on the discharge in greater detail than was done in Chapter 4, where only the difference between quartz and alumina in ambient air was investigated. Surface analysis techniques such as atomic force microscopy, XPS and spectroscopic ellipsometry, all readily available at Eindhoven University of Technology, will be used to determine if changes occur to the dielectric surface under the influence of DBD.

The proposed model for surface charge development in Chapter 5 also suggests that increasing the surface conductivity on the dielectric may lead to longer-burning filaments, and possibly to a single filament expanding over a larger area. This idea is not new; *e.g.* Okazaki *et al.* [171] and Golubovskii *et al.* [147] observe a radially expanding discharge on thin PET barriers overlaid on a fine conducting wire mesh. Similarly, Laroussi *et al.* use a relatively low resistivity material as a dielectric to obtain a diffuse discharge in He [172]. Using the new setup, dielectrics coated with thin conducting layers will also be investigated.

List of chemical reactions

The list on the following pages contains reactions relevant to recombining plasma in humid nitrogen-oxygen mixtures. All reactions marked with * are dependent on gas temperature and their rate constants have here been calculated for 320K. Recombination reactions between ions and electrons are assumed to have rates independent of species and are listed as reactions between species A, B and C where applicable, see [97] for details.

	Reaction	Rate constant	Unit	Ref.
	Ground states			
R1	$N + N + M \rightarrow N_2(A) + M$, $M = N_2, O_2$	$1.7 \cdot 10^{-33}$	$cm^6 s^{-1}$	[98]
R2	$N + N + M \rightarrow N_2(B) + M$, $M = N_2, O_2$	$2.4 \cdot 10^{-33}$	$cm^6 s^{-1}$	[98]
R3	$N + N + M \rightarrow N_2(X) + M$, $M = N_2, O_2$	$1.1 \cdot 10^{-32}$	$cm^6 s^{-1}$	[99–103]
R4*	$N + O_2 \rightarrow NO + O$	$2 \cdot 10^{-16}$	$cm^3 s^{-1}$	[97,98]
R5	$N + O_3 \rightarrow NO + O_2$	$1.0 \cdot 10^{-16}$	$cm^3 s^{-1}$	[97,98,173]
R6*	$N + NO \rightarrow N_2 + O$	$1.9 \cdot 10^{-11}$	$cm^3 s^{-1}$	[97,98]
R7	$N + NO_2 \rightarrow N_2 + O_2$	$7 \cdot 10^{-13}$	$cm^3 s^{-1}$	[97,99]
R8	$N + NO_2 \rightarrow N_2 + O + O$	$9.1 \cdot 10^{-13}$	$cm^3 s^{-1}$	[97,99]
R9	$N + NO_2 \rightarrow N_2O + O$	$3 \cdot 10^{-12}$	$cm^3 s^{-1}$	[97,99]
R10	$N + NO_2 \rightarrow NO + NO$	$2.3 \cdot 10^{-12}$	$cm^3 s^{-1}$	[97,99]
R11	$N + OH \rightarrow H + NO$	$7.5 \cdot 10^{-11}$	$cm^3 s^{-1}$	[174]
R12*	$N + HO_2 \rightarrow NO + OH$	$7.5 \cdot 10^{-13}$	$cm^3 s^{-1}$	[174]
R13*	$N + O + M \rightarrow NO + M$, $M = N_2, O_2$	$9.8 \cdot 10^{-33}$	$cm^3 s^{-1}$	[97,98,175]
R14	$N + O + M \rightarrow NO(B) + M$, $M = N_2, O_2$	$2.9 \cdot 10^{-34}$	$cm^3 s^{-1}$	[175,176]
R15	$O + O + N_2 \rightarrow O_2 + N_2$	$2.6 \cdot 10^{-33}$	$cm^6 s^{-1}$	[97,98]
R16	$O + O + O_2 \rightarrow O_2 + O_2$	$5.2 \cdot 10^{-33}$	$cm^6 s^{-1}$	[97,98]
R17	$O + O + M \rightarrow O_2(a) + M$	$2 \cdot 10^{-34}$	$cm^6 s^{-1}$	[98]
R18	$O + O + M \rightarrow O_2(b) + M$	$2 \cdot 10^{-35}$	$cm^6 s^{-1}$	[98]
R19*	$O + NO_2 \rightarrow NO + O_2$	$9 \cdot 10^{-12}$	$cm^3 s^{-1}$	[97]
R20*	$O + O_3 \rightarrow O_2 + O_2$	$1.5 \cdot 10^{-14}$	$cm^3 s^{-1}$	[97]
R21*	$O + O_3 \rightarrow O_2 + O_2(a)$	$7.5 \cdot 10^{-15}$	$cm^3 s^{-1}$	[98]
R22	$O + NO_3 \rightarrow O_2 + NO_2$	10^{-11}	$cm^3 s^{-1}$	[97]
R23*	$O + O_2 + N_2 \rightarrow O_3 + N_2$	$5.1 \cdot 10^{-34}$	$cm^3 s^{-1}$	[97,98]
R24*	$O + O_2 + O_2 \rightarrow O_3 + O_2$	$6.6 \cdot 10^{-34}$	$cm^3 s^{-1}$	[97,98]
R25	$O + NO + M \rightarrow NO_2 + M$	$1.0 \cdot 10^{-31}$	$cm^3 s^{-1}$	[98,173]

R26	$O + NO_2 + M \rightarrow NO_3 + M$	$7.4 \cdot 10^{-32}$	$cm^3 s^{-1}$	[97,98,173]
R27	$O + H + M \rightarrow OH + M$	$1.6 \cdot 10^{-32}$	$cm^6 s^{-1}$	[174]
R28*	$O + OH \rightarrow H + O_2$	$7.3 \cdot 10^{-12}$	$cm^3 s^{-1}$	[174]
R29*	$O + H_2O_2 \rightarrow OH + HO_2$	$3.3 \cdot 10^{-15}$	$cm^3 s^{-1}$	[174]
R30*	$O + HO_2 \rightarrow OH + O_2$	$1.7 \cdot 10^{-11}$	$cm^3 s^{-1}$	[174]
R31	$O + HNO \rightarrow OH + NO$	$6.0 \cdot 10^{-11}$	$cm^3 s^{-1}$	[174]
R32*	$O + HNO_2 \rightarrow NO_2 + OH$	$1.7 \cdot 10^{-16}$	$cm^3 s^{-1}$	[174]
R33*	$O_3 + H \rightarrow OH + O_2$	$2.9 \cdot 10^{-11}$	$cm^3 s^{-1}$	[174]
R34*	$O_3 + OH \rightarrow HO_2 + O_2$	$7.0 \cdot 10^{-14}$	$cm^3 s^{-1}$	[174]
R35*	$O_3 + HO_2 \rightarrow OH + O_2 + O_2$	$2.1 \cdot 10^{-15}$	$cm^3 s^{-1}$	[174]
R36*	$NO + O_3 \rightarrow O_2 + NO_2$	$2.8 \cdot 10^{-14}$	$cm^3 s^{-1}$	[97,98]
R37	$NO + NO_3 \rightarrow NO_2 + NO_2$	$1.7 \cdot 10^{-11}$	$cm^3 s^{-1}$	[97,98]
R38*	$NO + OH + M \rightarrow HNO_2 + M$	$6.3 \cdot 10^{-31}$	$cm^6 s^{-1}$	[174]
R39*	$NO + H + M \rightarrow HNO + M$	$2.6 \cdot 10^{-32}$	$cm^6 s^{-1}$	[174]
R40*	$NO + HO_2 \rightarrow OH + NO_2$	$7.9 \cdot 10^{-12}$	$cm^3 s^{-1}$	[174]
R41*	$NO + HO_2 \rightarrow HNO + O_2$	$1.4 \cdot 10^{-14}$	$cm^3 s^{-1}$	[174]
R42*	$NO_2 + O_3 \rightarrow O_2 + NO_3$	$5.7 \cdot 10^{-17}$	$cm^3 s^{-1}$	[97]
R43*	$NO_2 + NO_3 \rightarrow NO + NO_2 + O_2$	$1.5 \cdot 10^{-15}$	$cm^3 s^{-1}$	[97]
R44	$NO_2 + NO_2 + M \rightarrow N_2O_4 + M$	$5.6 \cdot 10^{-34}$	$cm^3 s^{-1}$	[97]
R45	$NO_2 + NO_3 + M \rightarrow N_2O_5 + M$	$4.1 \cdot 10^{-32}$	$cm^3 s^{-1}$	[97]
R46	$NO_2 + H \rightarrow OH + NO$	$1.5 \cdot 10^{-10}$	$cm^3 s^{-1}$	[174]
R47*	$NO_2 + OH + M \rightarrow HNO_3 + M$	$1.8 \cdot 10^{-30}$	$cm^6 s^{-1}$	[174]
R48*	$NO_3 + NO_3 \rightarrow O_2 + NO_2 + NO_2$	$4.2 \cdot 10^{-16}$	$cm^3 s^{-1}$	[97]
R49*	$NO_3 + H \rightarrow OH + NO_2$	$5.6 \cdot 10^{-11}$	$cm^3 s^{-1}$	[174]
R50	$NO_3 + OH \rightarrow HO_2 + NO_2$	$2 \cdot 10^{-11}$	$cm^3 s^{-1}$	[174]
R51	$NO_3 + HO_2 \rightarrow NO_2 + OH + O_2$	$4.8 \cdot 10^{-12}$	$cm^3 s^{-1}$	[174]
R52	$NO_3 + HO_2 \rightarrow HNO_3 + O_2$	$9.2 \cdot 10^{-13}$	$cm^3 s^{-1}$	[174]
R53	$H + O_2 + M \rightarrow HO_2 + M$	$4.8 \cdot 10^{-32}$	$cm^6 s^{-1}$	[174]
R54*	$H + H + M \rightarrow H_2 + M$	$5.6 \cdot 10^{-33}$	$cm^6 s^{-1}$	[174]
R55*	$H + OH + M \rightarrow H_2O + M$	$6.0 \cdot 10^{-31}$	$cm^6 s^{-1}$	[174]
R56*	$H + H_2O_2 \rightarrow OH + H_2O$	$6.1 \cdot 10^{-14}$	$cm^3 s^{-1}$	[174]
R57*	$H + H_2O_2 \rightarrow HO_2 + H_2$	$7.4 \cdot 10^{-15}$	$cm^3 s^{-1}$	[174]
R58	$H + HO_2 \rightarrow H_2 + O_2$	$5.6 \cdot 10^{-12}$	$cm^3 s^{-1}$	[174]
R59	$H + HO_2 \rightarrow O + H_2O$	$2.4 \cdot 10^{-12}$	$cm^3 s^{-1}$	[174]
R60*	$H + HO_2 \rightarrow OH + OH$	$2.2 \cdot 10^{-11}$	$cm^3 s^{-1}$	[174]
R61*	$H + HNO \rightarrow NO + H_2$	$6.3 \cdot 10^{-12}$	$cm^3 s^{-1}$	[174]
R62*	$H + HNO_2 \rightarrow NO_2 + H_2$	$1.9 \cdot 10^{-16}$	$cm^3 s^{-1}$	[174]

R63*	$H + HNO_3 \rightarrow NO_2 + H_2O$	$9.0 \cdot 10^{-19}$	$cm^3 s^{-1}$	[174]
R64*	$H_2 + OH \rightarrow H + H_2O$	$9.5 \cdot 10^{-15}$	$cm^3 s^{-1}$	[174]
R65*	$OH + OH \rightarrow O + H_2O$	$1.8 \cdot 10^{-12}$	$cm^3 s^{-1}$	[174]
R66*	$OH + OH + M \rightarrow H_2O_2 + M$	$6.6 \cdot 10^{-31}$	$cm^6 s^{-1}$	[174]
R67*	$OH + HO_2 \rightarrow O_2 + H_2O$	$1.0 \cdot 10^{-10}$	$cm^3 s^{-1}$	[174]
R68*	$OH + H_2O_2 \rightarrow HO_2 + H_2O$	$1.8 \cdot 10^{-12}$	$cm^3 s^{-1}$	[174]
R69*	$OH + HNO \rightarrow NO + H_2O$	$1.7 \cdot 10^{-11}$	$cm^3 s^{-1}$	[174]
R70*	$OH + HNO_2 \rightarrow NO_2 + H_2O$	$5.3 \cdot 10^{-12}$	$cm^3 s^{-1}$	[174]
R71*	$OH + HNO_3 \rightarrow NO_3 + H_2O$	$1.1 \cdot 10^{-13}$	$cm^3 s^{-1}$	[174]
R72*	$HO_2 + HO_2 \rightarrow H_2O_2 + O_2$	$1.4 \cdot 10^{-12}$	$cm^3 s^{-1}$	[174]
R73*	$HNO + O_2 \rightarrow NO + HO_2$	$4.7 \cdot 10^{-14}$	$cm^3 s^{-1}$	[174]
R74	$HNO + O_2 \rightarrow NO_2 + OH$	$1.7 \cdot 10^{-15}$	$cm^3 s^{-1}$	[174]
R75*	$HNO + HNO \rightarrow N_2O + H_2O$	$9.4 \cdot 10^{-18}$	$cm^3 s^{-1}$	[174]
R76	$HNO_2 + HNO_2 \rightarrow NO + NO_2 + H_2O$	$1 \cdot 10^{-20}$	$cm^3 s^{-1}$	[174]
R77	$HNO_2 + HNO_3 \rightarrow NO_2 + NO_2 + H_2O$	$1.6 \cdot 10^{-17}$	$cm^3 s^{-1}$	[174]
	Excited states			
R78	$N_2(A) + O_2 \rightarrow N_2 + 2O$	$2.5 \cdot 10^{-12}$	$cm^3 s^{-1}$	[97]
R79	$N_2(A) + O_2 \rightarrow N_2O + O$	$4 \cdot 10^{-14}$	$cm^3 s^{-1}$	[97,98]
R80	$N_2(A) + O \rightarrow NO + N(^2D)$	$7 \cdot 10^{-12}$	$cm^3 s^{-1}$	[97,98]
R81	$N_2(A) + N_2O \rightarrow N_2 + N + NO$	10^{-11}	$cm^3 s^{-1}$	[97,98]
R82	$N_2(A) + N_2(A) \rightarrow N_2(B) + N_2$	$7 \cdot 10^{-11}$	$cm^3 s^{-1}$	[92,97,177]
R83	$N_2(A) + N_2(A) \rightarrow N_2(C) + N_2$	$1.5 \cdot 10^{-10}$	$cm^3 s^{-1}$	[93,98]
R84	$N_2(A) + N_2 \rightarrow N_2 + N_2$	$3.0 \cdot 10^{-18}$	$cm^3 s^{-1}$	[97]
R85	$N_2(A) + O_2 \rightarrow N_2 + O_2$	$1.3 \cdot 10^{-12}$	$cm^3 s^{-1}$	[97,98]
R86	$N_2(A) + O_2 \rightarrow N_2 + O_2(a)$	$2 \cdot 10^{-13}$	$cm^3 s^{-1}$	[98]
R87	$N_2(A) + O_2 \rightarrow N_2 + O_2(b)$	$2 \cdot 10^{-13}$	$cm^3 s^{-1}$	[98]
R88	$N_2(A) + N \rightarrow N_2 + N$	$2 \cdot 10^{-12}$	$cm^3 s^{-1}$	[98]
R89*	$N_2(A) + N \rightarrow N_2 + N(^2P)$	$5 \cdot 10^{-11}$	$cm^3 s^{-1}$	[97,98]
R90	$N_2(A) + O \rightarrow N_2 + O(^1S)$	$2.1 \cdot 10^{-11}$	$cm^3 s^{-1}$	[97,98]
R91	$N_2(A) + NO \rightarrow N_2 + NO(A)$	$7 \cdot 10^{-11}$	$cm^3 s^{-1}$	[97,98]
R92	$N_2(A) + O_3 \rightarrow products$	$4 \cdot 10^{-11}$	$cm^3 s^{-1}$	[177]
R93	$N_2(A) + NO_2 \rightarrow N_2 + O + NO$	10^{-12}	$cm^3 s^{-1}$	[98]
R94	$N_2(A) + H_2O \rightarrow H + OH + N_2$	$5 \cdot 10^{-14}$	$cm^3 s^{-1}$	[174]
R95	$N_2(B) + N_2 \rightarrow N_2(A) + N_2$	$4.0 \cdot 10^{-11}$	$cm^3 s^{-1}$	[97,98,105]
R96	$N_2(B) + N_2 \rightarrow N_2 + N_2$	$2.0 \cdot 10^{-12}$	$cm^3 s^{-1}$	[92,98,106]
R97	$N_2(B) + O_2 \rightarrow N_2 + O + O$	$3.0 \cdot 10^{-10}$	$cm^3 s^{-1}$	[97,98]

R98	$N_2(B) + NO \rightarrow N_2(A) + NO$	$2.4 \cdot 10^{-10}$	$cm^3 s^{-1}$	[97,98]
R99	$N_2(B) + H_2 \rightarrow N_2(A) + H_2$	$2.5 \cdot 10^{-11}$	$cm^3 s^{-1}$	[174]
R100	$N_2(a') + N_2 \rightarrow N_2(B) + N_2$	$2 \cdot 10^{-13}$	$cm^3 s^{-1}$	[97,98]
R101	$N_2(a') + O_2 \rightarrow N_2(B) + O + O$	$2.8 \cdot 10^{-11}$	$cm^3 s^{-1}$	[97,98]
R102	$N_2(a') + NO \rightarrow N_2 + N + O$	$3.6 \cdot 10^{-10}$	$cm^3 s^{-1}$	[97,98]
R103	$N_2(C) + N_2 \rightarrow N_2(a') + N_2$	10^{-11}	$cm^3 s^{-1}$	[97,98]
R104	$N_2(C) + O_2 \rightarrow N_2 + O(^1S) + O$	$3 \cdot 10^{-10}$	$cm^3 s^{-1}$	[97,98]
R105*	$O_2(a) + O_3 \rightarrow O_2 + O_2 + O(^1D)$	$7 \cdot 10^{-15}$	$cm^3 s^{-1}$	[97,98]
R106*	$O_2(a) + N \rightarrow NO + O$	$3 \cdot 10^{-15}$	$cm^3 s^{-1}$	[97,98]
R107	$O_2(a) + N_2 \rightarrow O_2 + N_2$	$3 \cdot 10^{-21}$	$cm^3 s^{-1}$	[97,98]
R108*	$O_2(a) + O_2 \rightarrow O_2 + O_2$	$2.1 \cdot 10^{-18}$	$cm^3 s^{-1}$	[97,98]
R109	$O_2(a) + O \rightarrow O_2 + O$	$7 \cdot 10^{-16}$	$cm^3 s^{-1}$	[97,98]
R110	$O_2(a) + NO \rightarrow O_2 + NO$	$2.5 \cdot 10^{-11}$	$cm^3 s^{-1}$	[97,98]
R111*	$O_2(a) + O_2(a) \rightarrow O_2 + O_2(b)$	$2 \cdot 10^{-17}$	$cm^3 s^{-1}$	[98]
R112	$O_2(b) + O_3 \rightarrow O_2 + O_2 + O$	$2 \cdot 10^{-11}$	$cm^3 s^{-1}$	[97,98]
R113*	$O_2(b) + N_2 \rightarrow O_2(a) + N_2$	$2 \cdot 10^{-15}$	$cm^3 s^{-1}$	[97,98]
R114*	$O_2(b) + O_2 \rightarrow O_2(a) + O_2$	$2 \cdot 10^{-16}$	$cm^3 s^{-1}$	[97,98]
R115	$O_2(b) + O \rightarrow O_2(a) + O$	$8 \cdot 10^{-14}$	$cm^3 s^{-1}$	[97,98]
R116	$O_2(b) + O \rightarrow O_2 + O(^1D)$	$6.7 \cdot 10^{-17}$	$cm^3 s^{-1}$	[97,98]
R117	$O_2(b) + NO \rightarrow O_2(a) + NO$	$5 \cdot 10^{-14}$	$cm^3 s^{-1}$	[97,98]
R118*	$N(^2D) + O_2 \rightarrow NO + O$	$1.5 \cdot 10^{-12}$	$cm^3 s^{-1}$	[97]
R119*	$N(^2D) + O_2 \rightarrow NO + O(^1D)$	$6.2 \cdot 10^{-12}$	$cm^3 s^{-1}$	[97]
R120	$N(^2D) + NO \rightarrow N_2 + O$	$6 \cdot 10^{-11}$	$cm^3 s^{-1}$	[97,98,177]
R121	$N(^2D) + N_2O \rightarrow NO(B) + N_2$	$3.2 \cdot 10^{-12}$	$cm^3 s^{-1}$	[97,98,178]
R122	$N(^2D) + N_2 \rightarrow N + N_2$	$6 \cdot 10^{-15}$	$cm^3 s^{-1}$	[97,98]
R123	$N(^2P) + O_2 \rightarrow NO + O$	$2.6 \cdot 10^{-12}$	$cm^3 s^{-1}$	[97,98,177]
R124	$N(^2P) + NO \rightarrow N_2(A) + O$	$3.2 \cdot 10^{-11}$	$cm^3 s^{-1}$	[97,98]
R125	$N(^2P) + N_2 \rightarrow N(^2D) + N_2$	$2 \cdot 10^{-18}$	$cm^3 s^{-1}$	[97,98]
R126	$N(^2P) + N \rightarrow N(^2D) + N$	$1.8 \cdot 10^{-12}$	$cm^3 s^{-1}$	[97,98]
R127*	$O(^1D) + N_2 \rightarrow O + N_2$	$2.4 \cdot 10^{-11}$	$cm^3 s^{-1}$	[97,98]
R128*	$O(^1D) + O_2 \rightarrow O + O_2$	$7.9 \cdot 10^{-12}$	$cm^3 s^{-1}$	[97,98]
R129	$O(^1D) + O_2 \rightarrow O + O_2(a)$	10^{-12}	$cm^3 s^{-1}$	[98]
R130*	$O(^1D) + O_2 \rightarrow O + O_2(b)$	$3.1 \cdot 10^{-11}$	$cm^3 s^{-1}$	[97,98]
R131	$O(^1D) + O \rightarrow O + O$	$8 \cdot 10^{-12}$	$cm^3 s^{-1}$	[98]
R132	$O(^1D) + O_3 \rightarrow O + O + O_2$	$1.2 \cdot 10^{-10}$	$cm^3 s^{-1}$	[97,98]
R133	$O(^1D) + O_3 \rightarrow O_2 + O_2$	$1.2 \cdot 10^{-10}$	$cm^3 s^{-1}$	[97,98]
R134	$O(^1D) + NO \rightarrow O_2 + N$	$1.7 \cdot 10^{-10}$	$cm^3 s^{-1}$	[98]

R135	$O(^1D) + NO \rightarrow O + NO$	$4 \cdot 10^{-11}$	cm^3s^{-1}	[179]
R136	$O(^1D) + N_2O \rightarrow NO + NO$	$7.2 \cdot 10^{-11}$	cm^3s^{-1}	[97,98]
R137	$O(^1D) + N_2O \rightarrow N_2 + O_2$	$4.4 \cdot 10^{-11}$	cm^3s^{-1}	[97,98]
R138	$O(^1D) + H_2 \rightarrow OH + H$	$1.1 \cdot 10^{-10}$	cm^3s^{-1}	[174]
R139	$O(^1D) + H_2O \rightarrow OH + OH$	$2.2 \cdot 10^{-10}$	cm^3s^{-1}	[174]
R140	$O(^1S) + N_2 \rightarrow O + N_2$	$3 \cdot 10^{-17}$	cm^3s^{-1}	[97,98]
R141*	$O(^1S) + O_2 \rightarrow O + O_2$	$3 \cdot 10^{-13}$	cm^3s^{-1}	[97,98]
R142	$O(^1S) + O_3 \rightarrow O(^1D) + O + O_2$	$2.9 \cdot 10^{-10}$	cm^3s^{-1}	[97,98]
R143	$O(^1S) + O_3 \rightarrow O_2 + O_2$	$2.9 \cdot 10^{-10}$	cm^3s^{-1}	[97,98]
R144	$O(^1S) + NO \rightarrow O + NO$	$2.3 \cdot 10^{-10}$	cm^3s^{-1}	[97,98]
R145	$O(^1S) + NO \rightarrow O(^1D) + NO$	$4.1 \cdot 10^{-10}$	cm^3s^{-1}	[97,98]
R146	$O(^1S) + N_2O \rightarrow O + N_2O$	$6.3 \cdot 10^{-12}$	cm^3s^{-1}	[97,98]
R147	$O(^1S) + N_2O \rightarrow O(^1D) + NO(B)$	$3.1 \cdot 10^{-12}$	cm^3s^{-1}	[97,98,178]
R148	$O(^1S) + O_2(a) \rightarrow O(^1D) + O_2(b)$	$3.2 \cdot 10^{-11}$	cm^3s^{-1}	[97,98]
R149	$O(^1S) + O_2(a) \rightarrow O + O + O$	$3.3 \cdot 10^{-11}$	cm^3s^{-1}	[97,98]
R150	$O(^1S) + O_2(a) \rightarrow O + O_2$	$1.2 \cdot 10^{-10}$	cm^3s^{-1}	[97,98]
R151	$O(^1S) + O \rightarrow O(^1D) + O$	$2 \cdot 10^{-11}$	cm^3s^{-1}	[97,98]
R152	$NO(A) + N_2 \rightarrow NO + N_2$	$7.5 \cdot 10^{-14}$	cm^3s^{-1}	[175]
R153	$NO(A) + O_2 \rightarrow NO + O_2$	$1.8 \cdot 10^{-10}$	cm^3s^{-1}	[175]
R154	$NO(A) + NO \rightarrow NO + NO$	$2 \cdot 10^{-10}$	cm^3s^{-1}	[175]
R155	$NO(B) + N_2 \rightarrow NO + N_2$	$6 \cdot 10^{-13}$	cm^3s^{-1}	[175]
R156	$NO(B) + O_2 \rightarrow NO + O_2$	$1.5 \cdot 10^{-11}$	cm^3s^{-1}	[175]
R157	$NO(B) + NO \rightarrow NO + NO$	$2 \cdot 10^{-10}$	cm^3s^{-1}	[175]

	Radiative decay			
R158	$N_2(A) \rightarrow N_2 + h\nu$	0.5	s^{-1}	[98]
R159	$N_2(B) \rightarrow N_2(A) + h\nu$	$1.3 \cdot 10^5$	s^{-1}	[98]
R160	$N_2(C) \rightarrow N_2(B) + h\nu$	$2.5 \cdot 10^7$	s^{-1}	[98]
R161	$N_2(a') \rightarrow N_2 + h\nu$	100	s^{-1}	[98]
R162	$O_2(a) \rightarrow O_2 + h\nu$	$2.6 \cdot 10^{-4}$	s^{-1}	[98]
R163	$O_2(b) \rightarrow O_2(a) + h\nu$	$1.5 \cdot 10^{-3}$	s^{-1}	[98]
R164	$O_2(b) \rightarrow O_2 + h\nu$	$8.5 \cdot 10^{-2}$	s^{-1}	[98]
R165	$NO(A) \rightarrow NO + h\nu$	$5 \cdot 10^6$	s^{-1}	[176]
R166	$NO(B) \rightarrow NO + h\nu$	10^5	s^{-1}	[176]

	Associative ionization			
R167	$N_2(A) + N_2(a') \rightarrow N_4^+ + e$	$2.7 \cdot 10^{-11}$	cm^3s^{-1}	[97,98]

R168	$N_2(a') + N_2(a') \rightarrow N_4^+ + e$	$1.0 \cdot 10^{-10}$	cm^3s^{-1}	[97,98]
R169	$N(^2D) + N(^2P) \rightarrow N_2^+ + e$	10^{-12}	cm^3s^{-1}	[97]
R170	$O + N(^2P) \rightarrow NO^+ + e$	10^{-12}	cm^3s^{-1}	[97]

	Recombination with electrons			
R171	$A^+ + e + M \rightarrow A + M$	$6 \cdot 10^{-27} \cdot (300 / T_e)^{1.5}$	cm^6s^{-1}	[97]
R172	$N_4^+ + e \rightarrow N_2 + N_2$	$2.0 \cdot 10^{-6} \cdot \sqrt{300/T_e}$	cm^3s^{-1}	[97]
R173	$O_4^+ + e \rightarrow O_2 + O_2$	$1.4 \cdot 10^{-6} \cdot \sqrt{300/T_e}$	cm^3s^{-1}	[97]
R174	$NO^+(N_2) + e \rightarrow NO + N_2$	$1.3 \cdot 10^{-6} \cdot \sqrt{300/T_e}$	cm^3s^{-1}	[97]
R175	$NO^+(O_2) + e \rightarrow NO + O_2$	$1.3 \cdot 10^{-6} \cdot \sqrt{300/T_e}$	cm^3s^{-1}	[97]
R176	$O_2^+(N_2) + e \rightarrow O_2 + N_2$	$1.2 \cdot 10^{-6} \cdot \sqrt{300/T_e}$	cm^3s^{-1}	[97]
R177	$NO_2^+ + e \rightarrow NO + O$	$2.0 \cdot 10^{-7} \cdot \sqrt{300/T_e}$	cm^3s^{-1}	[97]
R178	$N_2O^+ + e \rightarrow N_2 + O$	$2.0 \cdot 10^{-7} \cdot \sqrt{300/T_e}$	cm^3s^{-1}	[97]
R179	$N_3^+ + e \rightarrow N_2 + N$	$2.0 \cdot 10^{-7} \cdot \sqrt{300/T_e}$	cm^3s^{-1}	[97]
R180	$N_2^+ + e \rightarrow N + N$	$2.8 \cdot 10^{-7} \cdot \sqrt{300/T_e}$	cm^3s^{-1}	[97]
R181	$N_2^+ + e \rightarrow N + N(^2D)$	$2.0 \cdot 10^{-7} \cdot \sqrt{300/T_e}$	cm^3s^{-1}	[97]
R182	$O_2^+ + e \rightarrow O + O$	$1.8 \cdot 10^{-7} \cdot (300/T_e)^{0.5}$	cm^3s^{-1}	[98]
R183	$O_2^+ + e \rightarrow O(^1D) + O$	$1.4 \cdot 10^{-7} \cdot (300/T_e)^{0.5}$	cm^3s^{-1}	[98]
R184	$NO^+ + e \rightarrow N + O$	$8.4 \cdot 10^{-8} \cdot (300/T_e)^{0.8}$	cm^3s^{-1}	[98]
R185	$NO^+ + e \rightarrow N(^2D) + O$	$3.4 \cdot 10^{-7} \cdot (300/T_e)^{0.8}$	cm^3s^{-1}	[98]
R186	$H_2^+ + e \rightarrow H + H$	$1.9 \cdot 10^{-7} \cdot T_e^{-0.43}$	cm^3s^{-1}	[174]
R187	$H_3^+ + e \rightarrow H_2 + H$	$5.2 \cdot 10^{-5} \cdot T_e^{-0.50}$	cm^3s^{-1}	[174]
R188	$H_3^+ + e \rightarrow H + H + H$	$1.1 \cdot 10^{-5} \cdot T_e^{-0.97}$	cm^3s^{-1}	[174]
R189	$H_2O^+ + e \rightarrow OH + H$	$2.7 \cdot 10^{-6} \cdot T_e^{-0.50}$	cm^3s^{-1}	[174]
R190	$H_2O^+ + e \rightarrow O + H_2$	$1.4 \cdot 10^{-6} \cdot T_e^{-0.50}$	cm^3s^{-1}	[174]
R191	$H_2O^+ + e \rightarrow O + H + H$	$1.4 \cdot 10^{-6} \cdot T_e^{-0.50}$	cm^3s^{-1}	[174]
R192	$H_3O^+ + e \rightarrow OH + H + H$	$5.5 \cdot 10^{-6} \cdot T_e^{-0.50}$	cm^3s^{-1}	[174]

	Attachment and detachment			
R193*	$e + O_2 + O_2 \rightarrow O_2^- + O_2$	$1.8 \cdot 10^{-29} e^{-700/T_e}$	cm^6s^{-1}	[98]
R194*	$e + O_2 + N_2 \rightarrow O_2^- + N_2$	$8.4 \cdot 10^{-30} e^{-1500/T_e}$	cm^6s^{-1}	[98]
R195	$e + O + O_2 \rightarrow O^- + O_2$	10^{-31}	cm^6s^{-1}	[97]
R196	$e + O + O_2 \rightarrow O + O_2^-$	10^{-31}	cm^6s^{-1}	[97]
R197	$e + O_3 + O_2 \rightarrow O_3^- + O_2$	10^{-31}	cm^6s^{-1}	[97]
R198	$e + O_3 \rightarrow O_2^- + O$	10^{-9}	cm^3s^{-1}	[97,98]
R199	$e + O_3 \rightarrow O^- + O_2$	10^{-11}	cm^3s^{-1}	[97,98]
R200	$e + NO_2 \rightarrow NO_2^-$	$3 \cdot 10^{-11}$	cm^3s^{-1}	[97]

162

R201	$e + NO + M \rightarrow NO^- + M$	10^{-30}	cm^6s^{-1}	[97]
R202	$e + NO_2 \rightarrow O^- + NO$	10^{-11}	cm^3s^{-1}	[97]
R203	$O_2^- + O_2(a) \rightarrow O_2 + O_2 + e$	$2 \cdot 10^{-10}$	cm^3s^{-1}	[97]
R204	$O_2^- + O_2(b) \rightarrow O_2 + O_2 + e$	$3.6 \cdot 10^{-10}$	cm^3s^{-1}	[97]
R205	$O_2^- + N_2(A) \rightarrow O_2 + N_2 + e$	$2.1 \cdot 10^{-9}$	cm^3s^{-1}	[97]
R206	$O_2^- + N_2(B) \rightarrow O_2 + N_2 + e$	$2.5 \cdot 10^{-9}$	cm^3s^{-1}	[97]
R207	$O^- + O_2(a) \rightarrow O_3 + e$	$3 \cdot 10^{-10}$	cm^3s^{-1}	[97]
R208	$O^- + O_2(b) \rightarrow O + O_2 + e$	$6.9 \cdot 10^{-10}$	cm^3s^{-1}	[97]
R209	$O^- + N_2(A) \rightarrow O + N_2 + e$	$2.2 \cdot 10^{-9}$	cm^3s^{-1}	[97]
R210	$O^- + N_2(B) \rightarrow O + N_2 + e$	$1.9 \cdot 10^{-9}$	cm^3s^{-1}	[97]
R211	$O^- + H_2 \rightarrow H_2O + e$	$7 \cdot 10^{-10}$	cm^3s^{-1}	[174]
R212	$NO^- + H_2 \rightarrow NO + H_2 + e$	$1.4 \cdot 10^{-9}$	cm^3s^{-1}	[174]
R213	$H^- + O_2 \rightarrow HO_2 + e$	$1.2 \cdot 10^{-9}$	cm^3s^{-1}	[174]
R214	$H^- + H \rightarrow H_2 + e$	$1.8 \cdot 10^{-9}$	cm^3s^{-1}	[174]
R215	$OH^- + O \rightarrow HO_2 + e$	$2 \cdot 10^{-9}$	cm^3s^{-1}	[174]
R216	$OH^- + H \rightarrow H_2O + e$	$1.8 \cdot 10^{-9}$	cm^3s^{-1}	[174]

	Associative detachment			
R217	$O_2^- + O \rightarrow O_3 + e$	$1.5 \cdot 10^{-10}$	cm^3s^{-1}	[97]
R218	$O_2^- + N \rightarrow NO_2 + e$	$5 \cdot 10^{-10}$	cm^3s^{-1}	[97]
R219	$O^- + O \rightarrow O_2 + e$	$5 \cdot 10^{-10}$	cm^3s^{-1}	[97]
R220	$O^- + N \rightarrow NO + e$	$2.6 \cdot 10^{-10}$	cm^3s^{-1}	[97]
R221	$O_3^- + O \rightarrow O_2 + O_2 + e$	$3 \cdot 10^{-10}$	cm^3s^{-1}	[97]
R222	$NO_2^- + O \rightarrow NO_3 + e$	10^{-12}	cm^3s^{-1}	[97]
R223	$O^- + O_2 \rightarrow O_3 + e$	$5 \cdot 10^{-15}$	cm^3s^{-1}	[97]
R224	$O^- + NO \rightarrow NO_2 + e$	$2.6 \cdot 10^{-10}$	cm^3s^{-1}	[97]

	Positive ions			
R225	$N_2^+ + N_2 + N_2 \rightarrow N_4^+ + N_2$	$4.5 \cdot 10^{-29}$	cm^6s^{-1}	[97,98]
R226*	$N_2^+ + N + N_2 \rightarrow N_3^+ + N_2$	$3.1 \cdot 10^{-29}$	cm^6s^{-1}	[97,98]
R227*	$O_2^+ + O_2 + O_2 \rightarrow O_4^+ + O_2$	$1.9 \cdot 10^{-30}$	cm^6s^{-1}	[97,98]
R228*	$O_2^+ + N_2 + N_2 \rightarrow O_2^+(N_2) + N_2$	$7.9 \cdot 10^{-31}$	cm^6s^{-1}	[97,98]
R229*	$NO^+ + N_2 + N_2 \rightarrow NO^+(N_2) + N_2$	$1.5 \cdot 10^{-31}$	cm^6s^{-1}	[97,98]
R230	$NO^+ + O_2 + N_2 \rightarrow NO^+(O_2) + N_2$	$3 \cdot 10^{-31}$	cm^6s^{-1}	[97,98]
R231	$NO^+ + O_2 + O_2 \rightarrow NO^+(O_2) + O_2$	$9 \cdot 10^{-32}$	cm^6s^{-1}	[97,98]
R232	$NO^+ + N_2O_5 + O_2 \rightarrow NO_2^+ + NO_2 + NO_2$	$5.9 \cdot 10^{-10}$	cm^6s^{-1}	[174]
R233	$N^+ + N_2 + N_2 \rightarrow N_3^+ + N_2$	$2.3 \cdot 10^{-29}$	cm^6s^{-1}	[97,98]

R234	$N^+ + O + M \rightarrow NO^+ + M$	10^{-29}	cm^6s^{-1}	[97,98]
R235	$N^+ + N + M \rightarrow N_2^+ + M$	10^{-29}	cm^6s^{-1}	[97,98]
R236	$O^+ + N_2 + M \rightarrow NO^+ + N + M$	$5.3 \cdot 10^{-29}$	cm^6s^{-1}	[97,98]
R237	$O^+ + O + M \rightarrow O_2^+ + M$	10^{-29}	cm^6s^{-1}	[97,98]
R238	$O^+ + N + M \rightarrow NO^+ + M$	10^{-29}	cm^6s^{-1}	[97,98]
R239	$N^+ + O_2 \rightarrow O_2^+ + N$	$2.8 \cdot 10^{-10}$	cm^3s^{-1}	[97,98]
R240	$N^+ + O_2 \rightarrow NO^+ + O$	$2.5 \cdot 10^{-10}$	cm^3s^{-1}	[97,98]
R241	$N^+ + O_2 \rightarrow O^+ + NO$	$2.8 \cdot 10^{-11}$	cm^3s^{-1}	[97,98]
R242	$N^+ + O \rightarrow N + O^+$	10^{-12}	cm^3s^{-1}	[97,98]
R243	$N^+ + O_3 \rightarrow NO^+ + O_2$	$5 \cdot 10^{-10}$	cm^3s^{-1}	[97,98]
R244	$N^+ + NO \rightarrow N + NO^+$	$8 \cdot 10^{-10}$	cm^3s^{-1}	[97,98]
R245	$N^+ + NO \rightarrow N_2^+ + O$	$3 \cdot 10^{-12}$	cm^3s^{-1}	[97,98]
R246	$N^+ + NO \rightarrow N_2 + O^+$	10^{-12}	cm^3s^{-1}	[97,98]
R247	$N^+ + N_2O \rightarrow NO^+ + N_2$	$5.5 \cdot 10^{-10}$	cm^3s^{-1}	[97,98]
R248	$N^+ + OH \rightarrow OH^+ + N$	$3.4 \cdot 10^{-10}$	cm^3s^{-1}	[174]
R249	$N^+ + OH \rightarrow NO^+ + H$	$3.4 \cdot 10^{-10}$	cm^3s^{-1}	[174]
R250	$N^+ + H_2O \rightarrow H_2O^+ + N$	$1.2 \cdot 10^{-9}$	cm^3s^{-1}	[174]
R251	$N^+ + H_2O \rightarrow NO^+ + H_2$	$2.1 \cdot 10^{-10}$	cm^3s^{-1}	[174]
R252	$O^+ + N_2 \rightarrow NO^+ + N$	$1.0 \cdot 10^{-12}$	cm^3s^{-1}	[97,98]
R253	$O^+ + O_2 \rightarrow O_2^+ + O$	$1.9 \cdot 10^{-11}$	cm^3s^{-1}	[97,98]
R254	$O^+ + O_3 \rightarrow O_2^+ + O_2$	10^{-10}	cm^3s^{-1}	[97,98]
R255	$O^+ + NO \rightarrow NO^+ + O$	$2.4 \cdot 10^{-11}$	cm^3s^{-1}	[97,98]
R256	$O^+ + NO \rightarrow O_2^+ + N$	$3 \cdot 10^{-12}$	cm^3s^{-1}	[97,98]
R257	$O^+ + N(^2D) \rightarrow N^+ + O$	$1.3 \cdot 10^{-10}$	cm^3s^{-1}	[97,98]
R258	$O^+ + NO_2 \rightarrow NO_2^+ + O$	$1.6 \cdot 10^{-9}$	cm^3s^{-1}	[97,98]
R259	$O^+ + N_2O \rightarrow N_2O^+ + O$	$3.1 \cdot 10^{-10}$	cm^3s^{-1}	[97,98]
R260	$O^+ + N_2O \rightarrow NO^+ + NO$	$2.3 \cdot 10^{-10}$	cm^3s^{-1}	[97,98]
R261	$O^+ + N_2O \rightarrow O_2^+ + N_2$	$2 \cdot 10^{-11}$	cm^3s^{-1}	[97,98]
R262	$O^+ + H \rightarrow H^+ + O$	$6.8 \cdot 10^{-10}$	cm^3s^{-1}	[174]
R263	$O^+ + H_2 \rightarrow OH^+ + H$	$1.7 \cdot 10^{-9}$	cm^3s^{-1}	[174]
R264	$O^+ + OH \rightarrow OH^+ + O$	$3.3 \cdot 10^{-10}$	cm^3s^{-1}	[174]
R265	$O^+ + OH \rightarrow O_2^+ + H$	$3.6 \cdot 10^{-10}$	cm^3s^{-1}	[174]
R266	$O^+ + H_2O \rightarrow H_2O^+ + O$	$3.2 \cdot 10^{-9}$	cm^3s^{-1}	[174]
R267	$N_2^+ + O_2 \rightarrow O_2^+ + N_2$	$5.8 \cdot 10^{-11}$	cm^3s^{-1}	[97,98]
R268	$N_2^+ + O \rightarrow NO^+ + N$	$1.3 \cdot 10^{-10}$	cm^3s^{-1}	[97,98]
R269	$N_2^+ + O \rightarrow O^+ + N_2$	10^{-11}	cm^3s^{-1}	[97,98]
R270	$N_2^+ + O_3 \rightarrow O_2^+ + O + N_2$	10^{-10}	cm^3s^{-1}	[97,98]

164

R271	$N_2^+ + N_2(A) \rightarrow N_3^+ + N$	$\leq 3 \cdot 10^{-10}$	$cm^3 s^{-1}$	[97]
R272	$N_2^+ + N \rightarrow N^+ + N_2$	$7.7 \cdot 10^{-13}$	$cm^3 s^{-1}$	[97,98]
R273	$N_2^+ + NO \rightarrow NO^+ + N_2$	$3.3 \cdot 10^{-10}$	$cm^3 s^{-1}$	[97,98]
R274	$N_2^+ + N_2O \rightarrow NO^+ + N_2 + N$	$4 \cdot 10^{-10}$	$cm^3 s^{-1}$	[97,98]
R275	$N_2^+ + N_2O \rightarrow N_2O^+ + N_2$	$6 \cdot 10^{-16}$	$cm^3 s^{-1}$	[97,98]
R276	$N_2^+ + H_2O \rightarrow H_2O^+ + N_2$	$2.3 \cdot 10^{-9}$	$cm^3 s^{-1}$	[174]
R277	$O_2^+ + N_2 \rightarrow NO^+ + NO$	10^{-17}	$cm^3 s^{-1}$	[97,98]
R278	$O_2^+ + N \rightarrow NO^+ + O$	$1.2 \cdot 10^{-10}$	$cm^3 s^{-1}$	[97,98]
R279	$O_2^+ + NO \rightarrow NO^+ + O_2$	$4.4 \cdot 10^{-10}$	$cm^3 s^{-1}$	[97,98]
R280	$O_2^+ + NO_2 \rightarrow NO^+ + O_3$	10^{-11}	$cm^3 s^{-1}$	[97,98]
R281	$O_2^+ + NO_2 \rightarrow NO_2^+ + O_2$	$6.6 \cdot 10^{-10}$	$cm^3 s^{-1}$	[97,98]
R282	$NO^+ + O_3 \rightarrow NO_2^+ + O_2$	10^{-15}	$cm^3 s^{-1}$	[97]
R283	$N_3^+ + O_2 \rightarrow O_2^+ + N + N_2$	$2.3 \cdot 10^{-11}$	$cm^3 s^{-1}$	[97,98]
R284	$N_3^+ + O_2 \rightarrow NO_2^+ + N_2$	$4.4 \cdot 10^{-11}$	$cm^3 s^{-1}$	[97,98]
R285	$N_3^+ + N \rightarrow N_2^+ + N_2$	$6.6 \cdot 10^{-11}$	$cm^3 s^{-1}$	[97,98]
R286	$N_3^+ + NO \rightarrow NO^+ + N + N_2$	$7 \cdot 10^{-11}$	$cm^3 s^{-1}$	[97,98]
R287	$N_3^+ + NO \rightarrow N_2O^+ + N_2$	$7 \cdot 10^{-11}$	$cm^3 s^{-1}$	[97,98]
R288	$NO_2^+ + NO \rightarrow NO^+ + NO_2$	$2.9 \cdot 10^{-10}$	$cm^3 s^{-1}$	[97,98]
R289	$N_2O^+ + NO \rightarrow NO^+ + N_2O$	$2.9 \cdot 10^{-10}$	$cm^3 s^{-1}$	[97,98]
R290	$N_4^+ + N_2 \rightarrow N_2^+ + N_2 + N_2$	$3 \cdot 10^{-15}$	$cm^3 s^{-1}$	[97,98]
R291	$N_4^+ + O_2 \rightarrow O_2^+ + N_2 + N_2$	$2.5 \cdot 10^{-15}$	$cm^3 s^{-1}$	[97,98]
R292	$N_4^+ + O \rightarrow O^+ + N_2 + N_2$	$2.5 \cdot 10^{-15}$	$cm^3 s^{-1}$	[97,98]
R293	$N_4^+ + N \rightarrow N^+ + N_2 + N_2$	10^{-11}	$cm^3 s^{-1}$	[97,98]
R294	$N_4^+ + NO \rightarrow NO^+ + N_2 + N_2$	$4 \cdot 10^{-10}$	$cm^3 s^{-1}$	[97,98]
R295*	$N_4^+ + H_2 \rightarrow H_2^+ + N_2 + N_2$	$1.1 \cdot 10^{-12}$	$cm^3 s^{-1}$	[174]
R296	$N_4^+ + H_2O \rightarrow H_2O^+ + N_2 + N_2$	$3 \cdot 10^{-9}$	$cm^3 s^{-1}$	[174]
R297	$O_4^+ + N_2 \rightarrow O_2^+(N_2) + N_2$	$1.3 \cdot 10^{-15}$	$cm^3 s^{-1}$	[97,98]
R298	$O_4^+ + O_2 \rightarrow O_2^+ + O_2 + O_2$	$3.8 \cdot 10^{-13}$	$cm^3 s^{-1}$	[97,98]
R299	$O_4^+ + O_2(a,b) \rightarrow O_2^+ + O_2 + O_2$	10^{-10}	$cm^3 s^{-1}$	[97,98]
R300	$O_4^+ + O \rightarrow O_2^+ + O_3$	$3 \cdot 10^{-10}$	$cm^3 s^{-1}$	[97,98]
R301	$O_4^+ + NO \rightarrow NO^+ + O_2 + O_2$	10^{-10}	$cm^3 s^{-1}$	[97,98]
R302	$O_2^+(N_2) + N_2 \rightarrow O_2^+ + N_2 + N_2$	$4.9 \cdot 10^{-10}$	$cm^3 s^{-1}$	[97,98]
R303	$O_2^+(N_2) + O_2 \rightarrow O_4^+ + N_2$	10^{-9}	$cm^3 s^{-1}$	[97,98]
R304	$NO^+(N_2) + N_2 \rightarrow NO^+ + N_2 + N_2$	$2.1 \cdot 10^{-11}$	$cm^3 s^{-1}$	[97,98]
R305	$NO^+(O_2) + N_2 \rightarrow NO^+ + O_2 + N_2$	$4 \cdot 10^{-11}$	$cm^3 s^{-1}$	[180]
R306	$H^+ + O \rightarrow O^+ + H$	$3.8 \cdot 10^{-10}$	$cm^3 s^{-1}$	[174]
R307	$H^+ + O_2 \rightarrow O_2^+ + H$	$1.2 \cdot 10^{-9}$	$cm^3 s^{-1}$	[174]

R308	$H^+ + NO \rightarrow NO^+ + H$	$1.9 \cdot 10^{-9}$	$cm^3 s^{-1}$	[174]
R309	$H^+ + H_2 + M \rightarrow H_3^+ + M$	$3. \cdot 10^{-29}$	$cm^6 s^{-1}$	[174]
R310	$H^+ + H_2O \rightarrow H_2O^+ + H$	$8.2 \cdot 10^{-9}$	$cm^3 s^{-1}$	[174]
R311	$H_2^+ + O_2 \rightarrow O_2^+ + H_2$	$7.8 \cdot 10^{-10}$	$cm^3 s^{-1}$	[174]
R312	$H_2^+ + H \rightarrow H^+ + H_2$	$6.4 \cdot 10^{-10}$	$cm^3 s^{-1}$	[174]
R313	$H_2^+ + H_2 \rightarrow H_3^+ + H$	$2 \cdot 10^{-9}$	$cm^3 s^{-1}$	[174]
R314	$H_2^+ + H_2O \rightarrow H_3O^+ + H$	$3.4 \cdot 10^{-9}$	$cm^3 s^{-1}$	[174]
R315	$H_2^+ + H_2O \rightarrow H_2O^+ + H_2$	$3.9 \cdot 10^{-9}$	$cm^3 s^{-1}$	[174]
R316	$H_3^+ + O \rightarrow OH^+ + H_2$	$8 \cdot 10^{-10}$	$cm^3 s^{-1}$	[174]
R317	$H_3^+ + H_2O \rightarrow H_3O^+ + H_2$	$3 \cdot 10^{-9}$	$cm^3 s^{-1}$	[174]
R318	$H_3^+ + NO_2 \rightarrow NO^+ + OH + H_2$	$7 \cdot 10^{-10}$	$cm^3 s^{-1}$	[174]
R319	$OH^+ + O_2 \rightarrow O_2^+ + OH$	$5.9 \cdot 10^{-10}$	$cm^3 s^{-1}$	[174]
R320	$OH^+ + NO \rightarrow NO^+ + OH$	$5.2 \cdot 10^{-10}$	$cm^3 s^{-1}$	[174]
R321	$OH^+ + NO_2 \rightarrow NO^+ + HO_2$	$1.3 \cdot 10^{-9}$	$cm^3 s^{-1}$	[174]
R322	$OH^+ + N_2O \rightarrow N_2O^+ + OH$	$2.1 \cdot 10^{-10}$	$cm^3 s^{-1}$	[174]
R323	$OH^+ + H_2 \rightarrow H_2O^+ + H$	$9.7 \cdot 10^{-10}$	$cm^3 s^{-1}$	[174]
R324	$OH^+ + OH \rightarrow H_2O^+ + O$	$7 \cdot 10^{-10}$	$cm^3 s^{-1}$	[174]
R325	$OH^+ + H_2O \rightarrow H_2O^+ + OH$	$1.6 \cdot 10^{-9}$	$cm^3 s^{-1}$	[174]
R326	$OH^+ + H_2O \rightarrow H_3O^+ + O$	$1.3 \cdot 10^{-9}$	$cm^3 s^{-1}$	[174]
R327	$H_2O^+ + N \rightarrow NO^+ + H_2$	$1.9 \cdot 10^{-10}$	$cm^3 s^{-1}$	[174]
R328	$H_2O^+ + O \rightarrow O_2^+ + H_2$	$5.5 \cdot 10^{-11}$	$cm^3 s^{-1}$	[174]
R329	$H_2O^+ + O_2 \rightarrow O_2^+ + H_2O$	$4.3 \cdot 10^{-10}$	$cm^3 s^{-1}$	[174]
R330	$H_2O^+ + NO \rightarrow NO^+ + H_2O$	$4.6 \cdot 10^{-10}$	$cm^3 s^{-1}$	[174]
R331	$H_2O^+ + NO_2 \rightarrow NO_2^+ + H_2O$	$1.2 \cdot 10^{-9}$	$cm^3 s^{-1}$	[174]
R332	$H_2O^+ + H_2 \rightarrow H_3O^+ + H$	$7.6 \cdot 10^{-10}$	$cm^3 s^{-1}$	[174]
R333	$H_2O^+ + H_2O \rightarrow H_3O^+ + OH$	$1.7 \cdot 10^{-9}$	$cm^3 s^{-1}$	[174]
R334	$H_3O^+ + NO \rightarrow NO^+ + H + H_2O$	$1.5 \cdot 10^{-12}$	$cm^3 s^{-1}$	[174]
R335	$H_3O^+ + N_2O_5 \rightarrow NO_2^+ + HNO_3 + H_2O$	$5.5 \cdot 10^{-16}$	$cm^3 s^{-1}$	[174]

	Negative ions			
R336	$O_2^- + O_2 + M \rightarrow O_4^- + M$	$3.3 \cdot 10^{-31}$	$cm^3 s^{-1}$	[97]
R337	$O^- + O_2 + M \rightarrow O_3^- + M$	$1.0 \cdot 10^{-30}$	$cm^3 s^{-1}$	[97]
R338	$O^- + NO + M \rightarrow NO_2^- + M$	10^{-29}	$cm^3 s^{-1}$	[97]
R339	$O_2^- + O \rightarrow O_2 + O^-$	$3.3 \cdot 10^{-10}$	$cm^3 s^{-1}$	[97]
R340	$O_2^- + O_3 \rightarrow O_2 + O_3^-$	$3.8 \cdot 10^{-10}$	$cm^3 s^{-1}$	[97,98]
R341	$O_2^- + NO_2 \rightarrow NO_2^- + O_2$	$7.5 \cdot 10^{-10}$	$cm^3 s^{-1}$	[97,98]
R342	$O_2^- + NO_3 \rightarrow NO_3^- + O_2$	$5 \cdot 10^{-10}$	$cm^3 s^{-1}$	[97,98]

R343	$O_2^- + N_2O \rightarrow O_3^- + N_2$	$< 10^{-12}$	$cm^3 s^{-1}$	[97,98]
R344	$O_2^- + HNO_3 \rightarrow NO_3^- + HO_2$	$2.8 \cdot 10^{-10}$	$cm^3 s^{-1}$	[174]
R345	$O^- + O_2(a) \rightarrow O_2^- + O$	10^{-10}	$cm^3 s^{-1}$	[97]
R346	$O^- + O_3 \rightarrow O + O_3^-$	$7.8 \cdot 10^{-10}$	$cm^3 s^{-1}$	[97,98]
R347	$O^- + NO_2 \rightarrow NO_2^- + O$	$1.2 \cdot 10^{-9}$	$cm^3 s^{-1}$	[97,98]
R348	$O^- + N_2O \rightarrow NO^- + NO$	$2 \cdot 10^{-10}$	$cm^3 s^{-1}$	[97,98]
R349	$O^- + N_2O \rightarrow N_2O^- + O$	$2 \cdot 10^{-12}$	$cm^3 s^{-1}$	[97,98]
R350	$O^- + H_2 \rightarrow OH^- + H$	$3.3 \cdot 10^{-11}$	$cm^3 s^{-1}$	[174]
R351	$O^- + H_2O \rightarrow OH^- + OH$	$1.4 \cdot 10^{-9}$	$cm^3 s^{-1}$	[174]
R352	$O_3^- + O \rightarrow O_2^- + O_2$	$1.6 \cdot 10^{-10}$	$cm^3 s^{-1}$	[97,98]
R353	$O_3^- + NO \rightarrow NO_3^- + O$	10^{-11}	$cm^3 s^{-1}$	[97,98]
R354	$O_3^- + NO \rightarrow NO_2^- + O_2$	$2.6 \cdot 10^{-12}$	$cm^3 s^{-1}$	[97]
R355	$O_3^- + NO_2 \rightarrow O_3 + NO_2^-$	$7 \cdot 10^{-10}$	$cm^3 s^{-1}$	[97,98]
R356	$O_3^- + NO_2 \rightarrow O_2 + NO_3^-$	$2 \cdot 10^{-11}$	$cm^3 s^{-1}$	[97,98]
R357	$O_3^- + NO_3 \rightarrow O_3 + NO_3^-$	$5 \cdot 10^{-10}$	$cm^3 s^{-1}$	[97,98]
R358	$O_3^- + H \rightarrow OH^- + O_2$	$8.4 \cdot 10^{-10}$	$cm^3 s^{-1}$	[174]
R359	$NO^- + O_2 \rightarrow O_2^- + NO$	$5 \cdot 10^{-10}$	$cm^3 s^{-1}$	[97,98]
R360	$NO^- + NO_2 \rightarrow NO_2^- + NO$	$7.4 \cdot 10^{-10}$	$cm^3 s^{-1}$	[97,98]
R361	$NO^- + N_2O \rightarrow NO_2^- + N_2$	$2.8 \cdot 10^{-14}$	$cm^3 s^{-1}$	[97,98]
R362	$NO_2^- + O_3 \rightarrow NO_3^- + O_2$	$1.8 \cdot 10^{-11}$	$cm^3 s^{-1}$	[97,98]
R363	$NO_2^- + NO_2 \rightarrow NO_3^- + NO$	$4 \cdot 10^{-12}$	$cm^3 s^{-1}$	[97,98]
R364	$NO_2^- + NO_3 \rightarrow NO_2 + NO_3^-$	$5 \cdot 10^{-10}$	$cm^3 s^{-1}$	[97,98]
R365	$NO_2^- + N_2O_5 \rightarrow NO_3^- + NO_3 + NO$	$7 \cdot 10^{-10}$	$cm^3 s^{-1}$	[174]
R366	$NO_2^- + H \rightarrow OH^- + NO$	$4 \cdot 10^{-10}$	$cm^3 s^{-1}$	[174]
R367	$NO_2^- + HNO_3 \rightarrow NO_3^- + HNO_2$	$7 \cdot 10^{-10}$	$cm^3 s^{-1}$	[174]
R368	$NO_3^- + NO \rightarrow NO_2^- + NO_3$	$3 \cdot 10^{-15}$	$cm^3 s^{-1}$	[97,98]
R369	$O_4^- + NO \rightarrow NO_3^- + O_2$	$2.5 \cdot 10^{-10}$	$cm^3 s^{-1}$	[97,98]
R370	$O_4^- + M \rightarrow O_2^- + O_2 + M$	$3.8 \cdot 10^{-12}$	$cm^3 s^{-1}$	[97,98]
R371	$O_4^- + O \rightarrow O_3^- + O_2$	$4 \cdot 10^{-10}$	$cm^3 s^{-1}$	[97]
R372	$O_4^- + O \rightarrow O^- + O_2 + O_2$	$3 \cdot 10^{-10}$	$cm^3 s^{-1}$	[97]
R373	$O_4^- + O_2(a,b) \rightarrow O_2^- + O_2 + O_2$	10^{-10}	$cm^3 s^{-1}$	[97]
R374	$H^- + N_2O \rightarrow OH^- + N_2$	$1.1 \cdot 10^{-9}$	$cm^3 s^{-1}$	[174]
R375	$H^- + NO_2 \rightarrow NO_2^- + H$	$2.9 \cdot 10^{-9}$	$cm^3 s^{-1}$	[174]
R376	$H^- + H_2O \rightarrow OH^- + H_2$	$3.8 \cdot 10^{-9}$	$cm^3 s^{-1}$	[174]
R377	$OH^- + O_3 \rightarrow O_3^- + OH$	$9 \cdot 10^{-10}$	$cm^3 s^{-1}$	[174]
R378	$OH^- + NO_2 \rightarrow NO_2^- + OH$	$1.9 \cdot 10^{-9}$	$cm^3 s^{-1}$	[174]

	Recombination of ions			
R379	$A^- + B^+ \rightarrow A + B$	$1.9 \cdot 10^{-7}$	$cm^3 s^{-1}$	[97]
R380	$A^- + (BC)^+ \rightarrow A + B + C$	10^{-7}	$cm^3 s^{-1}$	[97]

References

[1]   Bersin R L 1970 Automatic Plasma Machines for Stripping
        Photoresist *Solid State Technol.* **13** 39

[2]   Pappas D 2011 Status and potential of atmospheric plasma
        processing of materials *J. Vac. Sci. Technol. A Vacuum,
        Surfaces, Film.* **29** 020801

[3]   Kim H-H 2004 Nonthermal Plasma Processing for Air-
        Pollution Control: A Historical Review, Current Issues, and
        Future Prospects *Plasma Process. Polym.* **1** 91–110

[4]   Boer H E L De, Van Elzelingen-Dekker C M, Verberg C M F
        V R and Spanjaard L 2014 Use of Gaseous Ozone for
        Eradication of Methicillin Resistant Staphylococcus Aureus
        from the Home Environment of a Colonized Hospital
        Employee *Infect. Control Hosp. Epidemiol.* **27** 9–12

[5]   Mizuno A, Clements J S and Davis R H 1986 A Method for the
        Removal of Sulfur Dioxide from Exhaust Gas Utilizing Pulsed
        Streamer Corona for Electron Energization *IEEE Trans. Ind.
        Appl.* **IA-22** 516–22

[6]   Brehmer F K 2014 *Shining Light on Transient CO2 Plasma*
        (Eindhoven University of Technology)

[7]   Kong M G, Kroesen G M W, Morfill G, Nosenko T, Shimizu
        T, van Dijk J and Zimmermann J L 2009 Plasma medicine: an
        introductory review *New J. Phys.* **11** 115012

[8]   Laroussi M and Fridman A 2008 Plasma Medicine *Plasma
        Process. Polym.* **5** 501–2

[9]   Nastuta A V, Topala I, Grigoras C, Pohoata V and Popa G
        2011 Stimulation of wound healing by helium atmospheric
        pressure plasma treatment *J. Phys. D. Appl. Phys.* **44** 105204

[10] Patel C K N 1964 Continuous-Wave Laser Action on Vibrational-Rotational Transitions of CO2 *Phys. Rev.* **136** 1187–93

[11] Kogelschatz U, Eliasson B and Egli W 1997 Dielectric-Barrier Discharges. Principle and Applications *J. Phys. IV* **7** 47–66

[12] Kogelschatz U 2004 Atmospheric-pressure plasma technology *Plasma Phys. Control. Fusion* **46** B63–75

[13] Bárdos L and Baránková H 2010 Cold atmospheric plasma: Sources, processes, and applications *Thin Solid Films* **518** 6705–13

[14] d'Agostino R, Favia P, Oehr C and Wertheimer M R 2005 Low-Temperature Plasma Processing of Materials: Past, Present, and Future *Plasma Process. Polym.* **2** 7–15

[15] Goossens O, Dekempeneer E, Vangeneugden D, Van de Leest R and Leys C 2001 Application of atmospheric pressure dielectric barrier discharges in deposition, cleaning and activation *Surf. Coatings Technol.* **142-144** 474–81

[16] Merche D, Vandencasteele N and Reniers F 2012 Atmospheric plasmas for thin film deposition: A critical review *Thin Solid Films* **520** 4219–36

[17] Paulussen S, Rego R, Goossens O, Vangeneugden D and Rose K 2005 Plasma polymerization of hybrid organic–inorganic monomers in an atmospheric pressure dielectric barrier discharge *Surf. Coatings Technol.* **200** 672–5

[18] Vangeneugden D, Paulussen S, Goossens O, Rego R and Rose K 2005 Aerosol-Assisted Plasma Deposition of Barrier Coatings using Organic-Inorganic Sol-Gel Precursor Systems *Chem. Vap. Depos.* **11** 491–6

[19]   Bardon J, Bour J, Del Frari D, Arnoult C and Ruch D 2009 Dispersion of Cerium-Based Nanoparticles in an Organosilicon Plasma Polymerized Coating: Effect on Corrosion Protection *Plasma Process. Polym.* **6** S655–9

[20]   Bour J, Bardon J, Aubriet H, Del Frari D, Verheyde B, Dams R, Vangeneugden D and Ruch D 2008 Different Ways to Plasma-Polymerize HMDSO in DBD Configuration at Atmospheric Pressure for Corrosion Protection *Plasma Process. Polym.* **5** 788–96

[21]   Starostine S, Aldea E, de Vries H, Creatore M and van de Sanden M C M 2007 Atmospheric Pressure Barrier Discharge Deposition of Silica-Like Films on Polymeric Substrates *Plasma Process. Polym.* **4** S440–4

[22]   De Vries H, Mori F, Aldea E and van de Sanden M C M 2004 US 6774569, EP 1381257

[23]   Bouwstra J, Aldea E, van de Sanden M C M and de Vries H 2005 EP 1548795 A1

[24]   De Vries H, Bouwstra J, Aldea E, van de Sanden M C M and Peeters P 2006 EP 1626613 A1

[25]   Tendero C, Tixier C, Tristant P, Desmaison J and Leprince P 2006 Atmospheric pressure plasmas: A review *Spectrochim. Acta Part B At. Spectrosc.* **61** 2–30

[26]   Belmonte T, Henrion G and Gries T 2011 Nonequilibrium Atmospheric Plasma Deposition *J. Therm. Spray Technol.* **20** 744–59

[27]   Babaeva N Y and Kushner M J 2009 Effect of inhomogeneities on streamer propagation: I. Intersection with isolated bubbles and particles *Plasma Sources Sci. Technol.* **18** 035009

[28] Babaeva N Y and Kushner M J 2009 Effect of inhomogeneities on streamer propagation: II. Streamer dynamics in high pressure humid air with bubbles *Plasma Sources Sci. Technol.* **18** 035010

[29] Osawa N, Takashi A, Yoshioka Y and Hanaoka R 2013 Generation of high pressure homogeneous dielectric barrier discharge in air *Eur. Phys. J. Appl. Phys.* **61** 24317

[30] Golubovskii Y B, Maiorov V A and Behnke J F 2003 On the stability of a homogeneous barrier discharge in nitrogen relative to radial perturbations *J. Phys. D. Appl. Phys.* **36** 975–81

[31] Gherardi N and Massines F 2001 Mechanisms controlling the transition from glow silent discharge to streamer discharge in nitrogen *IEEE Trans. Plasma Sci.* **29** 536–44

[32] Stollenwerk L, Amiranashvili S, Boeuf J-P and Purwins H-G 2007 Formation and stabilisation of single current filaments in planar dielectric barrier discharge *Eur. Phys. J. D* **44** 133–9

[33] Papageorghiou L, Panousis E, Loiseau J-F, Spyrou N and Held B 2009 Two-dimensional modelling of a nitrogen dielectric barrier discharge (DBD) at atmospheric pressure: filament dynamics with the dielectric barrier on the cathode *J. Phys. D. Appl. Phys.* **42** 105201

[34] Wagner H-E, Yurgelenas Y V. and Brandenburg R 2005 The development of microdischarges of barrier discharges in N 2 /O 2 mixtures—experimental investigations and modelling *Plasma Phys. Control. Fusion* **47** B641–54

[35] Kozlov K V, Wagner H-E, Brandenburg R and Michel P 2001 Spatio-temporally resolved spectroscopic diagnostics of the barrier discharge in air *J. Phys. D. Appl. Phys.* **34** 3164

[36]   Sewraj N, Merbahi N, Gardou J P, Akerreta P R and Marchal F
        2011 Electric and spectroscopic analysis of a pure nitrogen
        mono-filamentary dielectric barrier discharge (MF-DBD) at
        760 Torr *J. Phys. D. Appl. Phys.* **44** 145201

[37]   Yurgelenas Y V. and Wagner H-E 2006 A computational
        model of a barrier discharge in air at atmospheric pressure: the
        role of residual surface charges in microdischarge formation *J.
        Phys. D. Appl. Phys.* **39** 4031–43

[38]   Yurgelenas Y V. and Leeva M a. 2009 Development of a
        Barrier Discharge in Air in Highly Nonhomogeneous Electric
        Field Caused by the Residual Dielectric Surface Charges *IEEE
        Trans. Plasma Sci.* **37** 809–15

[39]   Manley T C 1943 The electric characteristics of the ozonator
        discharge *Trans. Electrochem. Soc.* **84** 83–96

[40]   Hagelaar G 2011 BOLSIG+

[41]   Kogelschatz U 2010 Collective phenomena in volume and
        surface barrier discharges *J. Phys. Conf. Ser.* **257** 012015

[42]   Eliasson B and Kogelschatz U 1991 Modeling and applications
        of silent discharge plasmas *IEEE Trans. Plasma Sci.* **19** 309–
        23

[43]   Bruggeman P and Brandenburg R 2013 Atmospheric pressure
        discharge filaments and microplasmas: physics, chemistry and
        diagnostics *J. Phys. D. Appl. Phys.* **46** 464001

[44]   VITO http://www.vitoplasma.com/en/plasmaline

[45]   Lahti J 2012 *PlasmaNice Final Report*

[46]   Gibalov V I and Pietsch G J 2004 Properties of dielectric
        barrier discharges in extended coplanar electrode systems *J.
        Phys. D. Appl. Phys.* **37** 2093–100

[47]   Chirokov A, Gutsol A, Fridman A, Sieber K D, Grace J M and Robinson K S 2004 Analysis of two-dimensional microdischarge distribution in dielectric-barrier discharges *Plasma Sources Sci. Technol.* **13** 623–35

[48]   Xu X P and Kushner M J 1998 Multiple microdischarge dynamics in dielectric barrier discharges *J. Appl. Phys.* **84** 4153

[49]   Stollenwerk L, Amiranashvili S, Boeuf J-P and Purwins H-G 2006 Measurement and 3D Simulation of Self-Organized Filaments in a Barrier Discharge *Phys. Rev. Lett.* **96** 255001

[50]   Chirokov A, Gutsol A, Fridman A, Sieber K D, Grace J M and Robinson K S 2005 Self-organization of microdischarges in dielectric barrier discharge plasma *IEEE Trans. Plasma Sci.* **33** 300–1

[51]   Kogelschatz U 2003 Dielectric-barrier Discharges : Their History , Discharge Physics , and Industrial Applications *Plasma Chem. Plasma Process.* **23** 1–46

[52]   Wagner H-E, Brandenburg R, Kozlov K V, Sonnenfeld A, Michel P and Behnke J F 2003 The barrier discharge: basic properties and applications to surface treatment *Vacuum* **71** 417–36

[53]   Foest R, Kindel E, Ohl A, Stieber M and Weltmann K-D 2005 Non-thermal atmospheric pressure discharges for surface modification *Plasma Phys. Control. Fusion* **47** B525–36

[54]   Panousis E, Ricard A, Loiseau J-F, Clément F and Held B 2009 Estimation of densities of active species in an atmospheric pressure N2 DBD flowing afterglow using optical emission spectroscopy and analytical calculations *J. Phys. D. Appl. Phys.* **42** 205201

[55] Laroussi M and Lu X P 2005 Room-temperature atmospheric pressure plasma plume for biomedical applications *Appl. Phys. Lett.* **87** 113902

[56] Laroussi M and Akan T 2007 Arc-Free Atmospheric Pressure Cold Plasma Jets: A Review *Plasma Process. Polym.* **4** 777–88

[57] Förster S, Mohr C and Viöl W 2005 Investigations of an atmospheric pressure plasma jet by optical emission spectroscopy *Surf. Coatings Technol.* **200** 827–30

[58] Choi J H, Han M H and Baik H K 2008 Experimental Analysis of Reduced Electric Field during Time-Variable Pulsed Dielectric Barrier Discharge *Jpn. J. Appl. Phys.* **47** 1071–5

[59] Balcon N, Hagelaar G and Boeuf J-P 2008 Numerical Model of an Argon Atmospheric Pressure RF Discharge *IEEE Trans. Plasma Sci.* **36** 2782–7

[60] Barni R, Esena P and Riccardi C 2005 Chemical kinetics simulation for atmospheric pressure air plasmas in a streamer regime *J. Appl. Phys.* **97** 073301

[61] Xu X P and Kushner M J 1998 Ion composition of expanding microdischarges in dielectric barrier discharges *J. Appl. Phys.* **83** 7522

[62] Eliasson B, Hirth M and Kogelschatz U 1987 Ozone synthesis from oxygen in dielectric barrier discharges *J. Phys. D. Appl. Phys.* **20** 1421–37

[63] Liu S and Neiger M 2001 Excitation of dielectric barrier discharges by unipolar submicrosecond square pulses *J. Phys. D. Appl. Phys.* **34** 1632–8

[64] Liu S and Neiger M 2003 Electrical modelling of homogeneous dielectric barrier discharges under an arbitrary excitation voltage *J. Phys. D. Appl. Phys.* **36** 3144–50

[65]   Massines F, Rabehi A, Decomps P, Gadri R Ben, Ségur P and Mayoux C 1998 Experimental and theoretical study of a glow discharge at atmospheric pressure controlled by dielectric barrier *J. Appl. Phys.* **83** 2950

[66]   Naudé N, Cambronne J-P, Gherardi N and Massines F 2005 Electrical model and analysis of the transition from an atmospheric pressure Townsend discharge to a filamentary discharge *J. Phys. D. Appl. Phys.* **38** 530–8

[67]   Mangolini L, Anderson C, Heberlein J and Kortshagen U 2004 Effects of current limitation through the dielectric in atmospheric pressure glows in helium *J. Phys. D. Appl. Phys.* **37** 1021–30

[68]   Laroussi M, Lu X P, Kolobov V and Arslanbekov R 2004 Power consideration in the pulsed dielectric barrier discharge at atmospheric pressure *J. Appl. Phys.* **96** 3028

[69]   Nersisyan G and Graham W G 2004 Characterization of a dielectric barrier discharge operating in an open reactor with flowing helium *Plasma Sources Sci. Technol.* **13** 582–7

[70]   Falkenstein Z and Coogan J J 1999 Microdischarge behaviour in the silent discharge of nitrogen - oxygen and water - air mixtures *J. Phys. D. Appl. Phys.* **30** 817–25

[71]   Reichen P, Sonnenfeld A and von Rohr P R 2011 Discharge expansion in barrier discharge arrangements at low applied voltages *Plasma Sources Sci. Technol.* **20** 055015

[72]   Pipa A V., Koskulics J, Brandenburg R and Hoder T 2012 The simplest equivalent circuit of a pulsed dielectric barrier discharge and the determination of the gas gap charge transfer. *Rev. Sci. Instrum.* **83** 115112

[73]   Pipa A V., Hoder T, Koskulics J, Schmidt M and Brandenburg R 2012 Experimental determination of dielectric barrier discharge capacitance. *Rev. Sci. Instrum.* **83** 075111

[74]   Pipa A V., Hoder T and Brandenburg R 2013 On the Role of Capacitance Determination Accuracy for the Electrical Characterization of Pulsed Driven Dielectric Barrier Discharges *Contrib. to Plasma Phys.* **53** 469–80

[75]   Pipa A V., Hoder T, Koskulics J and Brandenburg R 2012 Approach of the simplest equivalent circuit for determination of charge transferred through the gas gap in pulsed dielectric barrier discharge *Hakone XIII*

[76]   Osawa N and Yoshioka Y 2012 Generation of low-frequency homogeneous dielectric barrier discharge at atmospheric pressure *IEEE Trans. Plasma Sci.* **40** 2–8

[77]   Osawa N, Yoshioka Y, Hanaoka R, Mochizuki Y, Kobayashi Y and Yamada Y 2012 Generation of uniform discharge by dielectric barrier discharge device in atmospheric-pressure air *Electr. Eng. Japan* **180** 1–9

[78]   Stollenwerk L and Stroth U 2011 Electric Charging in Dielectric Barrier Discharges with Asymmetric Gamma-Coefficients *Contrib. to Plasma Phys.* **51** 61–7

[79]   Panousis E, Merbahi N, Clément F, Ricard A, Yousfi M, Papageorghiou L, Loiseau J-F, Eichwald O, Held B and Spyrou N 2009 Atmospheric Pressure Dielectric Barrier Discharges Under Unipolar and Bipolar HV Excitation in View of Chemical Reactivity in Afterglow Conditions *IEEE Trans. Plasma Sci.* **37** 1004–15

[80]   Clément F, Panousis E, Ricard A, Lecoq E, Loiseau J-F and Held B 2010 Study of Dielectric Barrier Discharges in nitrogen and afterglows at atmospheric pressure *J. Phys. Conf. Ser.* **207** 012007

[81] Pointu A-M, Ricard A, Dodet B, Odic E, Larbre J and Ganciu M 2005 Production of active species in N 2 –O 2 flowing post-discharges at atmospheric pressure for sterilization *J. Phys. D. Appl. Phys.* **38** 1905–9

[82] Bockel S, Diamy a. M and Ricard A 1995 Optical diagnostics of active species in N2 microwave flowing post-discharges *Surf. Coatings Technol.* **74-75** 474–8

[83] Ricard A, Panousis E, Clément F, Sindzingre T and Loiseau J-F 2008 Production of active species in a N 2 DBD plasma afterglow *Eur. Phys. J. Appl. Phys.* **42** 63–6

[84] McKeon B, Comte-Bellot G, Foss J, Westerweel J, Scarano F, Tropea C, James M, Lee J, Cavone A, Schodl R, Koochesfahani M, Andreopoulos Y, Dahm W, Mullin J, Wallace J, Vukoslavčević P, Morris S, Pardyjak E and Cuerva A 2007 Velocity , Vorticity, and Mach Numer *Springer Handbook of Experimental Fluid Mechanics* pp 215–471

[85] Anon Air Products Nitrogen Premier

[86] Peeters F J J, Rumphorst R F and van de Sanden M C M Flow Velocity Measurements and Model for a Small Scale Linear Atmospheric Pressure Gas Jet with High Flow Velocity *To be Submitt.*

[87] Pearse R W B and Gaydon A G 1984 *The Identification of Molecular Spectra*

[88] Šimek M, Babicky V, Clupek M and Sunka P 2001 Observation of the N2 Herman infrared system in pulsed positive streamer *J. Phys. D. Appl. Phys.* **34** 3185–90

[89] Hays G N 1973 Population of N2(B) by N2(A) during the nitrogen afterglow *J. Chem. Phys.* **59** 1507

[90]   Hays G N 1973 Reaction rate constant for 2N2(A)→N2(C) + N2(X, ν′ > 0) *J. Chem. Phys.* **59** 6088

[91]   Hays G N, Tracy C J, Demonchy A R and Oskam H J 2000 Production of N2(C) and N2(C') by Mutual Collisions of N2(A) Metastable Molecules *Chem. Phys. Lett.* **14** 1–4

[92]   Piper L G 1988 State-to-state N2(A3∑+u) energy pooling reactions. II. The formation and quenching of N2(B3Πg, v'=1–12) *J. Chem. Phys.* **88** 6911

[93]   Piper L G 1988 State-to-state N2(A3Σ+u) energy-pooling reactions. I. The formation of N2(C3Πu) and the Herman infrared system *J. Chem. Phys.* **88** 231

[94]   Boudam M K, Saoudi B, Moisan M and Ricard A 2007 Characterization of the flowing afterglows of an N 2 –O 2 reduced-pressure discharge: setting the operating conditions to achieve a dominant late afterglow and correlating the NO β UV intensity variation with the N and O atom densities *J. Phys. D. Appl. Phys.* **40** 1694–711

[95]   Gordiets B F and Ricard A 1993 Production of N, O and NO in N2-O2 flowing discharges *Plasma Sources Sci. Technol.* **2** 158–63

[96]   Es-Sebbar E-T, Sarra-Bournet C, Naudé N, Massines F and Gherardi N 2009 Absolute nitrogen atom density measurements by two-photon laser-induced fluorescence spectroscopy in atmospheric pressure dielectric barrier discharges of pure nitrogen *J. Appl. Phys.* **106** 073302

[97]   Kossyi I A, Yu Kostinsky A, Matveyev A A and Silakov V P 1992 Kinetic scheme of the non-equilibrium discharge in nitrogen-oxygen mixtures *Plasma Sources Sci. Technol.* **1** 207–20

[98]   Capitelli M A, Ferreira C M, Gordiets B F and Osipov A I 2000 *Plasma Kinetics in Atmospheric Gases*

[99]   Harteck P, Reeves R R and Mannella G 1958 Rate of Recombination of Nitrogen Atoms *J. Chem. Phys.* **29** 608

[100]   Herron J T, Franklin J L, Bradt P and Dibeler V H 1959 Kinetics of Nitrogen Atom Recombination *J. Chem. Phys.* **30** 879

[101]   Herron J T, Franklin J L, Bradt P and Dibeler V H 1958 Kinetics of Nitrogen Atom Recombination *J. Chem. Phys.* **29** 230

[102]   Marshall T C 1962 Studies of Atomic Recombination of Nitrogen, Hydrogen, and Oxygen by Paramagnetic Resonance *Phys. Fluids* **5** 743

[103]   Clyne M A A and Stedman D H 1967 Rate of Recombination of Nitrogen Atoms *J. Phys. Chem.* **71** 3071–3

[104]   Miyazaki S and Takahashi S 1967 Reactions of Nitrogen Atom with Methane and with Ethylene *Bull. Chem. Soc. Jpn.* **41** 1456–8

[105]   Ricard A, Tétreault J and Hubert J 1991 Nitrogen atom recombination in high pressure Ar-N2 flowing post-discharges *J. Phys. B At. Mol. Opt. Phys.* **24** 1115–23

[106]   Ricard A, Besner A, Hubert J and Moisan M 1988 High nitrogen atom yield downstream of an atmospheric pressure flowing Ar-N2 microwave discharge *J. Phys. B At. Mol. Opt. Phys.* **21** L579–83

[107]   Tsyganov D and Pancheshnyi S 2012 Simulation of N-atom production in dielectric-barrier discharge in nitrogen at atmospheric pressure *Plasma Sources Sci. Technol.* **21** 065010

[108] Panousis E, Merbahi N, Clément F, Yousfi M and Loiseau J-F 2009 Analysis of Dielectric Barrier Discharges under Unipolar and Bipolar Pulsed Excitation *IEEE Trans. Dielectr. Electr. Insul.* **16** 734–41

[109] Stancu G D, Janda M, Kaddouri F, Lacoste D A and Laux C O 2010 Time-Resolved CRDS Measurements of the N 2 (A 3 Σ u) Density Produced by Nanosecond *J. Phys. Chem. A* **114** 201–8

[110] Šimek M 2003 Determination of N2(A) metastable density produced by nitrogen streamers at atmospheric pressure : 1 . Design of diagnostic method *Plasma Sources Sci. Technol.* **12** 421–31

[111] Šimek M 2003 Determination of N2(A) metastable density produced by nitrogen streamers at atmospheric pressure : 2 . Experimental verification *Plasma Sources Sci. Technol.* **12** 454–63

[112] Ellerweg D, von Keudell A and Benedikt J 2012 Unexpected O and O 3 production in the effluent of He/O 2 microplasma jets emanating into ambient air *Plasma Sources Sci. Technol.* **21** 034019

[113] Braun D, Kuchler U and Pietsch G J 1991 Microdischarges in air-fed ozonizers *J. Phys. D. Appl. Phys.* **24** 564–72

[114] Petrović D, Martens T, Dijk J Van, Brok W J M and Bogaerts A 2008 Modeling of a dielectric barrier discharge used as a flowing chemical reactor *J. Phys. Conf. Ser.* **133** 012023

[115] Panousis E, Papageorghiou L, Spyrou N, Loiseau J-F, Held B and Clément F 2007 Numerical modelling of an atmospheric pressure dielectric barrier discharge in nitrogen: electrical and kinetic description *J. Phys. D. Appl. Phys.* **40** 4168–80

[116] Celestin S, Bonaventura Z, Guaitella O, Rousseau A and Bourdon A 2009 Influence of surface charges on the structure of a dielectric barrier discharge in air at atmospheric pressure: experiment and modeling *Eur. Phys. J. Appl. Phys.* **47** 22810

[117] Akishev Y, Aponin G, Balakirev A, Grushin M, Karalnik V, Petryakov A and Trushkin N 2011 "Memory" and sustention of microdischarges in a steady-state DBD: volume plasma or surface charge? *Plasma Sources Sci. Technol.* **20** 024005

[118] Gibalov V I and Pietsch G J 2000 The development of dielectric barrier discharges in gas gaps and on surfaces *J. Phys. D. Appl. Phys.* **33** 2618–36

[119] Kozlov K V, Brandenburg R, Wagner H-E, Morozov a M and Michel P 2005 Investigation of the filamentary and diffuse mode of barrier discharges in N 2 /O 2 mixtures at atmospheric pressure by cross-correlation spectroscopy *J. Phys. D. Appl. Phys.* **38** 518–29

[120] Buss K 1932 Die elektrodenlose Entladung nach Messung mit dem Kathodenoszillographen *Arch. fur Elektrotechnik* **26** 261–5

[121] Akishev Y, Aponin G, Balakirev A, Grushin M, Karalnik V, Petryakov A and Trushkin N 2011 Role of the volume and surface breakdown in a formation of microdischarges in a steady-state DBD *Eur. Phys. J. D* **61** 421–9

[122] Höft H, Kettlitz M, Hoder T, Weltmann K-D and Brandenburg R 2013 The influence of O 2 content on the spatio-temporal development of pulsed driven dielectric barrier discharges in O 2 /N 2 gas mixtures *J. Phys. D. Appl. Phys.* **46** 095202

[123] Hirth M 1980 Teilprozesse bei der Ozonerzeugung mittels stiller elektrischer Entladungen *Beitrage aus der Plasmaphys.* **20** 1–14

[124] Gibalov V I, Dřímal J, Wronski M and Samoylovich V G 1991 Barrier Discharge The Transferred Charge and Ozone Synthesis *Contrib. to Plasma Phys.* **31** 89–99

[125] Gibalov V I and Pietsch G J 2012 Dynamics of dielectric barrier discharges in different arrangements *Plasma Sources Sci. Technol.* **21** 024010

[126] Dřímal J 1988 On value of transferred charge in silent discharge under atmospheric pressure *Czechoslov. J. Phys. B.* **38** 159–65

[127] Dřímal J, Gibalov V I and Samoylovich V G 1987 The magnitude of the transferred charge in the silent discharge in oxygen *Czechoslov. J. Phys. B.* **37** 1248–55

[128] Jidenko N, Petit M and Borra J P 2006 Electrical characterization of microdischarges produced by dielectric barrier discharge in dry air at atmospheric pressure *J. Phys. D. Appl. Phys.* **39** 281–93

[129] Dantzig R V A N, Koerts L A C, Oberski J E J, Mulder K, De Ridder T F, Sonnemans M A A, Wielinga B J, Ijpenberg A D, Biekmann W C M, Van Engen P G, Mars A J, Meesters R P, Suys J L C N M and Toenbreker S J A M 1971 Analysis of Multidimensional Nuclear Data (BOL) I *Nucl. Instruments Methods* **92** 205–13

[130] Oberski J E J, Mulder K, Koerts L A C, Van Dantzig R, Rumphorst R F, Bijvoets T, Dieperink J H, Kok E and Oostveen K 1971 Electronics of the BOL-System *Nucl. Instruments Methods* **92** 177–87

[131] Van Dantzig R, Oberski J E J, Koerts L A C, De Bie J E P, Biekmann W C M, Van Engen P G, Mars A J, Meesters R P, Sonnemans M A A and Visschers J L 1971 Data Acquisition with the BOL Nuclear Detection System *Nucl. Instruments Methods* **92** 199–203

[132] Limpert E, Stahel W A and Abbt M 2001 Log-normal Distributions across the Sciences: Keys and Clues *Bioscience* **51** 341

[133] Otto E, Fissan H, Park R S H S and Lee K W S 1999 The Log-Normal Size Distribution Theory of Brownian Aerosol Coagulation for the Entire Particle Size Range: Part II – Analytical Solution Using Dahneke's Coagulation Kernel *J. Aerosol Sci.* **30**

[134] Park S H, Lee K W, Otto E and Fissan H 1999 The Log-Normal Size Distribution Theory of Brownian Aerosol Coagulation for the Entire Particle Size Range: Part I – Analytical Solution Using The Harmonic Mean Coagulation Kernel *J. Aerosol Sci.* **30** 3–16

[135] Bogaczyk M, Wild R, Stollenwerk L and Wagner H-E 2012 Surface charge accumulation and discharge development in diffuse and filamentary barrier discharges operating in He, N 2 and mixtures *J. Phys. D. Appl. Phys.* **45** 465202

[136] Stollenwerk L 2009 Interaction of current filaments in dielectric barrier discharges with relation to surface charge distributions *New J. Phys.* **11** 103034

[137] Heuser C 1984 *Zur Ozonerzeugung in Elektrischen Gasentladungen* (RWTH Aachen)

[138] Bronold F X, Heinisch R L, Marbach J and Fehske H 2011 Plasma Walls Beyond the Perfect Absorber Approximation for Electrons *IEEE Trans. Plasma Sci.* **39** 644–51

[139] Bersch E, Rangan S, Bartynski R, Garfunkel E and Vescovo E 2008 Band offsets of ultrathin high-κ oxide films with Si *Phys. Rev. B* **78** 085114

[140] Raizer Y P 2011 *Gas Discharge Physics* (Springer)

[141] Meek J M 1940 A Theory of Spark Discharge *Phys. Rev.* **57** 722–8

[142] Yurgelenas Y V. and Leeva M a. 2010 Prebreakdown stages of a barrier discharge in air *Plasma Phys. Reports* **36** 1235–40

[143] Townsend J S 1915 *Electricity in gases* (Oxfor, Clarendon Press)

[144] Steinle G, Neundorf D, Hiller W and Pietralla M 1999 Two-dimensional simulation of filaments in barrier discharges *J. Phys. D. Appl. Phys.* **32** 1350–6

[145] Braun D, Gibalov V I and Pietsch G J 1992 Two-dimensional modelling of the dielectric barrier discharge in air *Plasma Sources Sci. Technol.* **1** 166

[146] Murata T, Tatsukawa M, Okita Y and Yasuoka K 1995 Polarity Effect of Silent Discharge *Ozone Sci. Eng.* **17** 575–85

[147] Golubovskii Y B, Maiorov V a, Behnke J F, Tepper J and Lindmayer M 2004 Study of the homogeneous glow-like discharge in nitrogen at atmospheric pressure *J. Phys. D. Appl. Phys.* **37** 1346–56

[148] Sjöberg M, Serdyuk Y V, Gubanski S M and Leijon M Å S 2003 Experimental study and numerical modelling of a dielectric barrier discharge in hybrid air–dielectric insulation *J. Electrostat.* **59** 87–113

[149] Kogelschatz U 1987 Filamentary and diffuse barrier discharges *Proceedings of the 16th International Conference on Phenomena in Ionized Gases* pp 240–50

[150] Brandenburg R, Bogaczyk M, Höft H, Nemschokmichal S, Tschiersch R, Kettlitz M, Stollenwerk L, Hoder T, Wild R, Weltmann K-D, Meichsner J and Wagner H-E 2013 Novel insights into the development of barrier discharges by

advanced volume and surface diagnostics *J. Phys. D. Appl. Phys.* **46** 464015

[151] Brandenburg R, Navrátil Z, Jánský J, St'ahel P, Trunec D and Wagner H-E 2009 The transition between different modes of barrier discharges at atmospheric pressure *J. Phys. D. Appl. Phys.* **42** 085208

[152] Peeters F J J, Rumphorst R F and van de Sanden M C M The Influence of Partial Surface Discharging on the Electrical Characterization of Dielectric Barrier Discharges *Submitt. to Plasma Sources Sci. Technol.*

[153] Peeters F J J, Rumphorst R F and van de Sanden M C M 2014 Microdischarge Distributions in Planar DBD's at High Filament Number Densities *To be Submitt.*

[154] Bogaczyk M, Nemschokmichal S, Wild R, Stollenwerk L, Brandenburg R, Meichsner J and Wagner H-E 2012 Development of Barrier Discharges: Operation Modes and Structure Formation *Contrib. to Plasma Phys.* **52** 847–55

[155] Heinisch R L, Bronold F X and Fehske H 2012 Electron surface layer at the interface of a plasma and a dielectric wall *Phys. Rev. B* **85** 075323

[156] Bronold F X, Fehske H, Heinisch R L and Marbach J 2012 Wall Charge and Potential from a Microscopic Point of View *Contrib. to Plasma Phys.* **52** 856–63

[157] Ambrico P F, Ambrico M, Colaianni a, Schiavulli L, Dilecce G and De Benedictis S 2010 Thermoluminescence study of the trapped charge at an alumina surface electrode in different dielectric barrier discharge regimes *J. Phys. D. Appl. Phys.* **43** 325201

[158] Ambrico P F, Ambrico M, Schiavulli L, Ligonzo T and Augelli V 2009 Charge trapping induced by plasma in alumina

electrode surface investigated by thermoluminescence and optically stimulated luminescence *Appl. Phys. Lett.* **94** 051501

[159] Marbach J, Bronold F X and Fehske H 2012 Resonant charge transfer at dielectric surfaces *Eur. Phys. J. D* **66** 106

[160] Marbach J, Bronold F X and Fehske H 2012 Pseudoparticle approach for charge-transferring molecule-surface collisions *Phys. Rev. B* **86** 115417

[161] Tay W H, Yap S L and Wong C S 2014 Electrical Characteristics and Modeling of a Filamentary Dielectric Barrier Discharge in Atmospheric Air *Sains Malaysiana* **43** 583–94

[162] Nijdam S, Takahashi E, Markosyan A H and Ebert U 2014 Investigation of positive streamers by double-pulse experiments , effects of *Plasma Sources Sci. Technol.* **23** 025008

[163] Stano M, Safonov E, Kučera M and Matejčik Š 2008 Ion mobility spectrometry study of negative corona discharge in oxygen/nitrogen mixtures *Chem. List.* **102** s1414–7

[164] Young R A, Gatz C R, Sharpless R L and Ablow C M 1965 New Method for Measuring the Rates of Ionic Transport and Loss. I. Mobility of NO+ *Phys. Rev.* **138** A359–70

[165] Snuggs R M, Volz D J, Schummers J H, Martin D W and McDaniel E W 1971 Mobilities and Longitudinal Diffusion Coefficients of Mass-Identified Potassium Ions and Positive and Negative Oxygen Ions in Oxygen *Phys. Rev. A* **3** 477–87

[166] Freeman G R and Wada T 1981 Temperature, density, and electric-field effects on electron mobility in nitrogen vapor *Phys. Rev. A* **24** 1066–76

[167] Higuchi T, Shiiyama K, Izumi Y, Howlader M M R, Kutsuwada M and Kinoshita C 2002 Effects of specimen thickness and impurity on the conductivity of alumina under electron irradiation *J. Nucl. Mater.* **307-311** 1250–3

[168] Okuyama Y, Kurita N and Fukatsu N 2010 Electrical conductivity of calcium-doped α-alumina *Solid State Ionics* **181** 142–7

[169] Semenyuk L N 1996 Electrical properties of alumina films *Inorg. Mater.* **32** 1310–1

[170] Yasserian K, Aslaninejad M, Borghei M and Eshghabadi M 2010 Electronegative plasma-sheath characteristics over a wide range of collisionality *J. Theor. Appl. Phys.* **4** 26–9

[171] Okazaki S, Kogoma M, Uehara M and Kimura Y 1993 Appearance of stable glow discharge in air, argon, oxygen and nitrogen at atmospheric pressure using a 50 Hz source *J. Phys. D. Appl. Phys.* **26** 889

[172] Laroussi M, Member S, Alexeff I, Richardson J P and Dyer F F 2002 The Resistive Barrier Discharge *IEEE Trans. Plasma Sci.* **30** 158–9

[173] Atkinson R, Baulch D L, Cox R A, Hampson R F, Kerr J A and Troe J 1989 Evaluated Kinetic and Photochemical Data for Atmospheric Chemistry: Supplement III *J. Phys. Chem. Ref. Data* **18** 881–1097

[174] Sakiyama Y, Graves D B, Chang H-W, Shimizu T and Morfill G E 2012 Plasma chemistry model of surface microdischarge in humid air and dynamics of reactive neutral species *J. Phys. D. Appl. Phys.* **45** 425201

[175] Melton L a. 1973 Energy transfer in monochromatically excited nitric oxide: A2Σ+ and B2Π *J. Chem. Phys.* **59** 1099

188

[176] Pintassilgo C D, Loureiro J and Guerra V 2005 Modelling of a N 2 –O 2 flowing afterglow for plasma sterilization *J. Phys. D. Appl. Phys.* **38** 417–30

[177] Herron J T 1999 Evaluated Chemical Kinetics Data for Reactions of N(D), N(P) and N2(A) in the Gas Phase *J. Phys. Chem. Ref. Data* **28** 1453

[178] Welge K H 1966 Formation of N2(A3Σu+) and N(2D, 2P) by Photodissociation of HN3 and N2O and Their Reactions with NO and N2O *J. Chem. Phys.* **45** 166–70

[179] Doroshenko V M, Kudryavtsev N N and Smetanin V V. 1992 Quenching mechanisms for electronically excited species in partially dissociated air *High Energy Chem.* **26** 227–30

[180] Hiraoka K and Yamabe S 1991 Cluster ions: Gas-phase stabilities of NO+(O2)n and NO+(CO2)n with n=1–5 *J. Chem. Phys.* **95** 6800

[181] Klarenaar B L M 2011 *Exploring the possibilities of the PlasmaLine, a study on GLYMO, TEOS & HMDS* (Eindhoven University of Technology)

[182] Fromy P, Pointu A-M, Ganciu M and Orphal J 2006 Transportation of nitrogen atoms in an atmospheric pressure post-discharge of pure nitrogen *J. Phys. D. Appl. Phys.* **39** 108–12

[183] Penetrante B M 2002 NOx reduction by electron beam-produced nitrogen atom injection Patent 6345497

[184] Babayan S E, Ding G, Nowling G R, Yang X and Hicks R F 2002 Characterization of the Active Species in the Afterglow of a Nitrogen and Helium Atmospheric-Pressure Plasma *Plasma Chem. Plasma Process.* **22** 255–69

Summary

The Electrical Dynamics of Dielectric Barrier Discharges

Dielectric Barrier Discharges (DBDs) can be used to produce plasma at atmospheric pressure and are employed on a large industrial scale for the production of ozone. While studied for over a century, interest has increased in recent years in the areas of materials processing, plasma medicine and solar fuels. The generation of plasma from DBDs at atmospheric pressure requires relatively simple, cost-effective technology compared to low pressure plasma generation methods, and therefore offers the advantages of plasma processing for lower added-value applications. The replacement of wet-chemical methods in surface coating and pre-treatment by plasma processing could reduce the environmental impact from hazardous chemicals and, moreover, can open up other applications due to the high chemical reactivity at low temperatures attainable by plasma. Examples of the latter include plasma enhanced catalysis for pollution control and on-site production of reactive chemicals for use as sterilizing agents for food and water and, recently, for medical treatment.

Irrespective of the application, the ability to control a DBD with regard to the dynamics of the discharge and the production rates of radicals is desirable. In this thesis the focus is on cheap process gases such as nitrogen and air, since these have the greatest potential for use in large-scale industrial processing, such as surface modification and deposition of materials. The proposed diagnostic methods are, however, equally applicable to other gases. Contrary to low-pressure discharges, atmospheric pressure discharges tend to be non-uniform, *i.e.* the plasma will consist of many small, transient microdischarges, also referred to as filaments, with diameters of ~ 0.1 mm and durations on the order of several 10's of nanoseconds, distributed over the dielectric surface. The research questions examined in this thesis regard (i) the relation between the voltage over the plasma filaments and radical production and (ii) the relation between individual filaments and electrical models of DBDs as a whole.

As a first step, an improved electrical model for DBDs is presented, which takes into account the possibility that the number density of filaments is insufficient to cover the entire electrode area. Using this model, the voltage drop over the plasma filaments, referred to as the burning voltage, can be determined irrespective of filament number density. By determining the atomic N concentration in an N_2 DBD, it is found that both the energy efficiency of atomic N production and the burning voltage are independent of the voltage applied to the DBD electrodes. The only control achieved over the discharge results from the number density of filaments on the electrode area. It follows from this that the burning voltage is a leading characteristic of both single filaments and the discharge as a whole.

Secondly, by combining a miniature DBD with an analog circuit designed to count and integrate individual filamentary current pulses, it is examined whether the current pulses through the filamentary discharge channels vary significantly with applied voltage amplitude or phase. At the same time, it is determined how the current pulses are affected by changes in the DBD geometry and how this affects burning voltage. Contrary to previous work, it is found that the statistical distributions of current pulses are log-normal in nature. Furthermore, the distributions are independent of filament number density for a given DBD geometry. Using both the improved electrical model and current pulse distributions, it is inferred that multi-filament discharge dynamics are regulated by mobile charges on or near the surface of the dielectric, resulting in step-wise ignition of filaments as a function of applied voltage. The log-normal charge/filament distributions, on the other hand, develop from the locally trapped charges on the dielectric. It is recommended that both mobile charges from residual conductivity and immobile trapped charges be considered in models of DBDs, especially when converting data from the abundant single-filament models in DBD literature to real devices. This added understanding of filamentary discharges may also prove relevant for promoting uniform discharging, which would offer great advantages for surface treatment applications.

Samenvatting

Het Elektrische Gedrag van Diëlektrische Barrière-ontladingen

Diëlektrische Barrière-ontladingen (DBDs) kunnen plasma genereren bij atmosferische druk en worden op grote industriële schaal benut voor de productie van ozon. Hoewel ze al meer dan een eeuw worden bestudeerd is er nu toenemende interesse voor het opdampen van functionele materialen met behulp van DBDs, de klinische toepassingen van door DBDs geproduceerde chemische stoffen en het gebruik van DBDs voor de afbraak van CO_2 in de atmosfeer. Het opwekken van plasma met DBDs is relatief eenvoudig en goedkoop ten opzichte van plasma's opgewekt bij lage druk, waardoor plasma's als chemische reactoren kunnen worden gebruikt bij toepassingen met een lage toegevoegde waarde. Het vervangen van nat-chemische industriële processen met plasma kan de invloed van schadelijke stoffen op het milieu terugdringen en bovendien leiden tot hele nieuwe toepassingen. Voorbeelden van dit laatste zijn plasmagedreven katalyse voor het reinigen van uitstootgassen, productie van stoffen ter sterilisatie van voedsel of water en het gebruik van plasma in de geneeskunde.

Onafhankelijk van de toepassing is het wenselijk de eigenschappen van de DBD te kunnen manipuleren en de productiesnelheden van chemische stoffen te controleren. In tegenstelling tot plasma's opgewekt bij lage druk hebben plasma's bij atmosferische druk de neiging niet uniform te zijn en te bestaan uit vele kleine, vergankelijke micro-ontladingen. Deze zogeheten filamenten hebben diameters van ~ 0.1 mm met levensduren van enkele tientallen nanoseconden en vinden gespreid over het oppervlak van de DBD plaats. De onderzoeksvragen in dit proefschrift omvatten (i) de relatie tussen de spanning over de filamenten en de productie van stoffen uit het procesgas en (ii) de relatie tussen de individuele filamenten en elektrische modellen van de DBD als geheel.

Allereerst wordt een verbeterd elektrisch model voor een DBD gepresenteerd, wat rekening houdt met de mogelijkheid dat het aantal filamenten tijdens de ontlading te gering is om het volledige

elektrode-oppervlak te bedekken. Met dit model kan de 'brandspanning' over de filamenten tijdens een ontlading nauwkeurig worden bepaald, ongeacht de dichtheid van de filamenten. Door ook de concentratie van atomair N in een N_2 DBD te bepalen wordt duidelijk dat zowel de dissociatie-efficiëntie als de brandspanning volledig onafhankelijk zijn van de spanning die aangelegd wordt over de elektroden. De enige beheersing over de ontlading wordt bereikt door de dichtheid van filamenten op het elektrode-oppervlak te variëren via de aangelegde spanning. Bovendien volgt hieruit dat de brandspanning een bepalende karakteristiek is van zowel individuele filamenten als de gehele ontlading.

Door een miniatuur DBD met klein oppervlak te combineren met een analoog circuit, ontworpen om de individuele stroompulsjes door de filamentaire plasmakanaaltjes te registreren, is onderzocht of de stroompulsjes aanzienlijk veranderen met de aangelegde spanning over de elektroden. Tegelijkertijd is onderzocht hoe de stroompulsjes worden beinvloed door de geometrie van de DBD, zoals de grootte van de spleet waarin de ontlading plaatsvindt, en wat de uitwerking hiervan is op de brandspanning. In tegenstelling tot andere onderzoeken, wordt hier een log-normale distributie van stroompulsjes gevonden. Bovendien zijn deze distributies volledig onafhankelijk van de aangelegde spanning. Door gebruik te maken van zowel het verbeterde elektrisch model en de distributies van stroompulsjes, is herleid dat DBDs worden gereguleerd door mobiele lading op of in het oppervlak van het dielektrische elektrodemateriaal. De log-normale verdelingen van de stroompulsjes, echter, zijn het gevolg van lokaal ingevangen lading in het materiaal. Aangezien bestaande modellen van DBDs uitgaan van enkel lokaal ingevangen lading, wordt aanbevolen om ook mobiele lading op te nemen in toekomstige modellen. Dit is vooral relevant voor het converteren van enkele-filament computermodellen naar complete DBD systemen. Deze nieuwe inzichten kunnen ook relevant blijken voor het bevorderen van uniforme, filament-vrije ontladingen, wat grote voordelen zou hebben voor het opdampen van functionele materialen met DBDs.

Acknowledgements

Finally. It is done. Six years, two projects and more than three office buildings ago, I started putting together this thesis. Though the odds were not in my favor during a significant portion of those six years, I am now very happy with the end result. The first person to thank for getting me to this point is Richard van de Sanden. Despite my sudden illness, which lasted for quite a few years, you always managed to assure me I could complete a thesis. After my funding ended, it was you who pushed me just a little bit further to pick up where I had left off. And here we are! I am looking forward to continuing our collaboration in the future.

In line with the above, my thesis work could not have been completed without the tireless efforts of Rein Rumphorst. Despite both of us being equally capable of coming up with crazy experimental plans, it was you who managed to put together all the electronic equipment to make it happen. At no cost (aside from broken limbs, electrical shocks and general confusion), which was essential considering the circumstances. In my mind, this book is yours as much as it is mine. Thank you for all of it!

Third, I owe a debt of gratitude to Niek Lopes Cardozo for his comments and support, which motivated me to tie together the separate bits and pieces of work I had collected into a coherent thesis. I would not have been as happy with the end result if it wasn't for you; many thanks!

Next to my scientific advisers, I wish to thank my auxiliary advisers for playing an important role in keeping me going: Jeanne Loonen, Lianne Doms and Mieke Rompen. Thank you for your listening ears and for helping me deal with all the non-scientific aspects of the past years!

A lot of the work, especially in the early days, was made possible by the technical support of Janneke Zeebregts, Ries van de Sande, Joris Meulendijks, Wytze Keuning and Herman de Jong at TU/e and Erwin van Hoof at VITO. Here, I also wish to thank Roel Dams of VITO for helping me out with measurements, Rong Yang for his many weeks of measuring emission spectra on the PlasmaLine and Bart Klarenaar; the only student a PhD candidate could ever need.

My gratitude also goes out to Hindrik de Vries and Sergei Starostin of Fujifilm and Differ for providing me with comments on my thesis. Thanks to everyone in the PlasmaNice project, also for all of the fun evenings across Europe. Special thanks in this regard to Dirk Vangeneugden and Marjorie Dubreuil for handling some of the workload during my absence.

Day-to-day life at the university would not have been as enjoyable without my many office mates: Pavel, Cristina, Arno, Tatiana, Roy, Sjoerd, Henriette, Yizhi, Bart M, the guys from EPG, and last but not least, Chai and Srinath. Thanks for putting up with me, though technically you had no choice in the matter! Of course, thanks to all other colleagues at PMP, who are too many to name. Special thanks to Harm Knoops for being an excellent Watson, my brothers-in-arms Srinath Ponduri (again), Florian Brehmer, Jan-Willem Weber and İlker Doğan, for struggling together on our theses, and Daan Schram for providing me with support and feedback over the past years. The oppurtunity to work on the EnergyDays with you was also much appreciated!

Outside TU/e there are many friends to thank for supporting me in more ways than I can count: Aafke, Tim, Florian L, Bart G, Mark, my flatmates Penny, Sheldon, Martin, Jules, Balthasar and Ziggy Stardust and many, many others (you know who you are, or at least I will conveniently assume you know). Also, a great many thanks to Christien for keeping my house livable in the meantime.

Thanks to my family Johan, Petra, Stéphanie, Clifton, Quentin and Isabella, for their support in difficult times and everything they did for me long before I started my PhD. Finally, and most importantly, I am very grateful to have met Doortje during my recovery and the writing of this thesis. Your love and support allowed me to achieve the impossible!

Curriculum Vitae

Personalia

Family name   Peeters
First names   Floran Johan Joseph
Date of birth   16 May 1983
Place of birth Rucphen, the Netherlands

Education

1995 - 2001   Atheneneum, KSE, Etten-Leur, the Netherlands

2001 - 2006   Bachelor of Science in Applied Physics, Eindhoven University of Technology, Eindhoven, the Netherlands

2007 - 2008   Master of Science in Applied Physics, Eindhoven University of Technology, Eindhoven, the Netherlands

                       Traineeship at TNO Science and Industry on FTIR spectroscopy of metal-polymer interfaces

                       Master thesis project in the group ETP on cavity ring-down spectroscopy of a-Si:H thin films

2009 - 2010   Researcher at Eindhoven University of Technology with FP7 EU project 'PlasmaNice' on surface modification using atmospheric pressure plasmas

2013 - 2015   Researcher at the Dutch Institute for Fundamental Energy Research, DIFFER on electrical diagnostics of dielectric barrier discharges